

DEVELOPMENT OF $\text{Sr}_2\text{FeTiO}_{6-\Delta}$ ELECTRODE FOR SOLID OXIDE FUEL CELL



A Thesis Submitted in Partial Fulfillment of the Requirements
for the Degree of Master of Science in Chemistry

Department of Chemistry

Faculty of Science

Chulalongkorn University

Academic Year 2018

Copyright of Chulalongkorn University

การพัฒนาขั้วไฟฟ้า $\text{Sr}_2\text{FeTiO}_{6-\delta}$ สำหรับเซลล์เชื้อเพลิงออกไซด์ของแข็ง



วิทยานิพนธ์นี้เป็นส่วนหนึ่งของการศึกษาตามหลักสูตรปริญญาวิทยาศาสตรมหาบัณฑิต

สาขาวิชาเคมี ภาควิชาเคมี

คณะวิทยาศาสตร์ จุฬาลงกรณ์มหาวิทยาลัย

ปีการศึกษา 2561

ลิขสิทธิ์ของจุฬาลงกรณ์มหาวิทยาลัย

อุษา โพธิ์ทอง : การพัฒนาขั้วไฟฟ้า $\text{Sr}_2\text{FeTiO}_{6-\text{delta}}$ สำหรับเซลล์เชื้อเพลิงออกไซด์
ของแข็ง. (DEVELOPMENT OF $\text{Sr}_2\text{FeTiO}_6-$

DELTA ELECTRODE FOR SOLID OXIDE FUEL CELL) อ.ที่ปรึกษาหลัก : รศ. ดร.โสภณ
ไชยอนันต์สุจริต

ดับเบิลเพอรอฟสไกต์ $\text{Sr}_2\text{FeTi}_{1-x}(\text{Nb},\text{V})_x\text{O}_6$ ($x=0.05-0.50$) สามารถเตรียมได้โดยการแทนที่ไนโอเบียมและวานาเดียมที่ตำแหน่งไทเทเนียมของ $\text{Sr}_2\text{FeTiO}_6$ (SFT) และนำไปทดสอบการเป็นขั้วไฟฟ้าในเซลล์เชื้อเพลิงของแข็งที่อุณหภูมิปานกลาง (500-800 องศาเซลเซียส) ผลการวิเคราะห์โครงสร้างด้วย XRD พบว่า $\text{Sr}_2\text{FeTi}_{0.95}\text{Nb}_{0.05}\text{O}_6$ และ $\text{Sr}_2\text{FeTi}_{0.95}\text{V}_{0.05}\text{O}_6$ เป็นสารบริสุทธิ์ ไม่มีโครงสร้างสารอื่นเจือปน และจะพบสารเจือปน ($\text{Sr}(\text{FeNb})_{0.5}\text{O}_3$ และ $\text{Sr}_3(\text{VO}_4)_2$) เมื่อเพิ่มอัตราส่วนของไนโอเบียมและวานาเดียมในโครงสร้าง การใส่ไนโอเบียมและวานาเดียมปริมาณเล็กน้อยลงในโครงสร้าง SFT ส่งผลให้ค่าการนำไฟฟ้าและสมบัติทางไฟฟ้าเคมีของ SFT ดีขึ้น เมื่อศึกษาสารออกไซด์ที่มีการแทนที่ในอัตราส่วนต่าง ๆ พบว่า $\text{Sr}_2\text{FeTi}_{0.95}\text{Nb}_{0.05}\text{O}_6$ และ $\text{Sr}_2\text{FeTi}_{0.95}\text{V}_{0.05}\text{O}_6$ มีค่าการนำไฟฟ้าสูงที่สุดคือ 2.44 และ 3.93 ซีเมนตต่อเซนติเมตรตามลำดับ และมีค่าความต้านทานที่ต่ำประมาณ 1.91 และ 1.89 โอห์มตารางเซนติเมตรที่อุณหภูมิ 800 องศาเซลเซียสตามลำดับ เมื่อนำสารที่สังเคราะห์ไปศึกษาสมบัติการเป็นขั้วไฟฟ้าใน SOFC พบว่า $\text{Sr}_2\text{FeTi}_{0.95}\text{Nb}_{0.05}\text{O}_6$ และ $\text{Sr}_2\text{FeTi}_{0.95}\text{V}_{0.05}\text{O}_6$ แสดงศักยภาพสูงโดยสามารถใช้เป็นทั้งขั้วแคโทดและแอโนดในเซลล์เชื้อเพลิงออกไซด์ของแข็งเดี่ยวได้ โดยค่ากำลังไฟฟ้าสูงสุดของแคโทดเมื่อใช้ LSGM เป็นอิเล็กโทรไลต์คือ 97 และ 106 มิลลิวัตต์ต่อตารางเซนติเมตรที่อุณหภูมิ 800 องศาเซลเซียสสำหรับ $\text{Sr}_2\text{FeTi}_{0.95}\text{Nb}_{0.05}\text{O}_6$ และ $\text{Sr}_2\text{FeTi}_{0.95}\text{V}_{0.05}\text{O}_6$ ตามลำดับ และการใช้เป็นขั้วแอโนดในเซลล์เชื้อเพลิงออกไซด์ของแข็งเดี่ยวของสาร $\text{Sr}_2\text{FeTi}_{0.95}\text{Nb}_{0.05}\text{O}_6$ และ $\text{Sr}_2\text{FeTi}_{0.95}\text{V}_{0.05}\text{O}_6$ พบว่าให้กำลังไฟฟ้าที่สูงที่สุดคือ 60 และ 86 มิลลิวัตต์ต่อตารางเซนติเมตรที่อุณหภูมิ 800 องศาเซลเซียส นอกจากนี้พบว่าสาร $\text{Sr}_2\text{FeTi}_{0.95}\text{Nb}_{0.05}\text{O}_6$ และ $\text{Sr}_2\text{FeTi}_{0.95}\text{V}_{0.05}\text{O}_6$ ที่ใช้เป็นอิเล็กโทรดไม่ทำปฏิกิริยากับ LSGM ที่เป็นอิเล็กโทรไลต์เมื่อนำมาเผาพร้อมกันที่อุณหภูมิ 900 องศาเซลเซียสเป็นเวลา 5 ชั่วโมงภายใต้บรรยากาศปกติ

สาขาวิชา เคมี

ลายมือชื่อนิสิต

ปีการศึกษา 2561

ลายมือชื่อ อ.ที่ปรึกษาหลัก

5872100023 : MAJOR CHEMISTRY

KEYWORD: Double perovskite, Solid oxide fuel cell, Electrode material

Ausa Potong : DEVELOPMENT OF $\text{Sr}_2\text{FeTiO}_6$ -
DELTA ELECTRODE FOR SOLID OXIDE FUEL CELL. Advisor: Assoc. Prof.
SOAMWADEE CHAIANANSUTCHARIT, Ph.D.

$\text{Sr}_2\text{FeTi}_{1-x}(\text{Nb},\text{V})_x\text{O}_6$ ($x=0.05-0.50$) double perovskites have been synthesized by the substitution of Nb and V on Ti sites of $\text{Sr}_2\text{FeTiO}_6$ (SFT) and tested as electrode for intermediate temperature solid oxide fuel cell (IT-SOFC). The XRD analyses indicated $\text{Sr}_2\text{FeTi}_{0.95}\text{Nb}_{0.05}\text{O}_6$ and $\text{Sr}_2\text{FeTi}_{0.95}\text{V}_{0.05}\text{O}_6$ were pure and the impurities, $\text{Sr}(\text{FeNb})_{0.5}\text{O}_3$ and $\text{Sr}_3(\text{VO}_4)_2$, were found with the increasing of Nb and V contents in SFT. By small addition of Nb and V in SFT, the electrical conductivity and electrochemical property of SFT was improved. Among the various oxide examined, $\text{Sr}_2\text{FeTi}_{0.95}\text{Nb}_{0.05}\text{O}_6$ and $\text{Sr}_2\text{FeTi}_{0.95}\text{V}_{0.05}\text{O}_6$ showed the highest electrical conductivity of 2.44 and 3.93 S cm^{-1} , respectively, and the lowest polarization resistance around 1.91 and 1.89 $\Omega \text{ cm}^2$ at 800°C in air, respectively. For the application as electrode in SOFC, $\text{Sr}_2\text{FeTi}_{0.95}\text{Nb}_{0.05}\text{O}_6$ and $\text{Sr}_2\text{FeTi}_{0.95}\text{V}_{0.05}\text{O}_6$ showed a high potential to be used as both cathode and anode in electrolyte-supported single cell SOFC. The maximum power density of cathodes with LSGM electrolyte were achieved about 97 and 106 mW cm^{-2} at 800°C for $\text{Sr}_2\text{FeTi}_{0.95}\text{Nb}_{0.05}\text{O}_6$ and $\text{Sr}_2\text{FeTi}_{0.95}\text{V}_{0.05}\text{O}_6$, respectively. And the single cell performance of $\text{Sr}_2\text{FeTi}_{0.95}\text{Nb}_{0.05}\text{O}_6$ and $\text{Sr}_2\text{FeTi}_{0.95}\text{V}_{0.05}\text{O}_6$ anodes were 60 and 86 mW cm^{-2} at 800°C, respectively. Furthermore, the reactivity tests demonstrated that $\text{Sr}_2\text{FeTi}_{0.95}\text{Nb}_{0.05}\text{O}_6$ and $\text{Sr}_2\text{FeTi}_{0.95}\text{V}_{0.05}\text{O}_6$ electrodes were chemically compatible with the LSGM electrolyte at 900°C for 5 hours in air.

Field of Study: Chemistry

Student's Signature

Academic Year: 2018

Advisor's Signature

ACKNOWLEDGEMENTS

I would like to express my sincere gratitude to my advisor Associate Professor Dr. Soamwadee Chaianansucharit for her invaluable help and constant encouragement throughout the course of this research. Her guidance helped me in all the time of research and writing of this thesis. I could not have imagined having a better advisor and mentor for my study.

I would like to thank Associate Professor Dr. Vudhichai Parasuk as the chairman, Associate Professor Dr. Saowarux Fuangswasdi and Assistant Professor Dr. Jinda Yeyongchaiwat for serving as this thesis committee.

In addition, I must express my very profound gratitude to my family, all lab's members and friends for providing me with unfailing support and continuous encouragement throughout my years of study and through the process of researching and writing this thesis.

Finally, I am grateful for the scholarship and funding of the thesis work provided by the Development and Promotion of Science and Technology Talents Project and Center of Excellence on Petrochemical and Materials Technology.

TABLE OF CONTENTS

	Page
ABSTRACT (THAI).....	iii
ABSTRACT (ENGLISH).....	iv
ACKNOWLEDGEMENTS	v
TABLE OF CONTENTS	vi
LIST OF TABLES.....	ix
LIST OF FIGURES	xi
CHAPTER 1 INTRODUCTION	1
1.1 Fuel cell	1
1.2 Solid oxide fuel cell (SOFC).....	2
1.2.1 SOFC operation	4
1.2.2 SOFC components.....	5
1.2.2.1 Electrolyte.....	5
1.2.2.2 Cathode.....	6
1.2.2.3 Anode.....	8
1.3 Double Perovskite Oxide	10
1.4 Electrical Conductivity.....	13
1.4.1 Electronic conductivity	13
1.4.2 Ionic conductivity.....	14
1.5 Fuel Cell Characterization	17
1.5.1 Current-Voltage (i-V) measurement	17
1.5.2 Electrochemical Impedance Spectroscopy (EIS).....	19

1.6 Literature Review.....	21
1.7 Objectives	24
CHAPTER 2 EXPERIMENTAL	25
2.1 Chemicals.....	25
2.2 Material preparation	26
2.2.1 Anode preparation.....	26
2.2.2 Cathode preparation	26
2.2.3 Samples preparation	27
2.2.4 Electrolyte preparation.....	28
2.2.5 Compatibility test	28
2.3 Material characterization	29
2.3.1 X-ray diffractometry (XRD)	29
2.3.2 Electrical conductivity Measurement	29
2.3.3 Thermal expansion coefficient (TEC)	30
2.3.4 Electrochemical Impedance Spectroscopy	30
2.3.5 SOFC performance	31
CHAPTER 3 RESULT AND DISCUSSION	33
3.1 XRD characterizations.....	33
3.2 Electrical conductivity measurement	36
3.3 Electrochemical Impedance Spectroscopy (EIS).....	44
3.4 Fuel cell performance.....	46
3.4.1 Testing of single cell performance using $\text{Sr}_2\text{FeTi}_{1-x}\text{M}_x\text{O}_{6-\delta}$ (M = Nb, V) oxides as the cathode material.....	46

3.4.2 Testing of single cell performance using $\text{Sr}_2\text{FeTi}_{1-x}\text{M}_x\text{O}_{6-\delta}$ (M = Nb, V) oxides as the anode material	52
3.4.3 Cell performance of symmetrical cell	57
3.5 X-ray Photoelectron analysis	58
3.5.1 XPS results of Nb-doped SFT double perovskites.....	58
3.5.2 XPS results of V-doped SFT double perovskites.....	65
3.5 Thermal expansion	69
3.7 The chemical compatibility	70
CHAPTER 4 CONCLUSION	73
4.1 Conclusion	73
4.2 Suggestion.....	74
REFERENCES	75
VITA.....	87

LIST OF TABLES

	Page
Table 1.1 A typical fuel cell	3
Table 2.1 The chemicals and reagents used in this research	25
Table 2.2 Compositions and abbreviations of prepare samples	28
Table 3.1 The maximum electrical conductivity (σ_{\max}) of SFT, $\text{Sr}_2\text{FeTi}_{1-x}\text{Nb}_x\text{O}_{6-\delta}$ and $\text{Sr}_2\text{FeTi}_{1-x}\text{V}_x\text{O}_{6-\delta}$ ($x = 0.05 - 0.5$).....	39
Table 3.2 Activation energy of conductivity for $\text{Sr}_2\text{FeTi}_{1-x}\text{Nb}_x\text{O}_{6-\delta}$ ($x = 0.05 - 0.50$).....	41
Table 3.3 Activation energy of conductivity for $\text{Sr}_2\text{FeTi}_{1-x}\text{V}_x\text{O}_{6-\delta}$ ($x = 0.05 - 0.50$).....	43
Table 3.4 The polarization resistance value of $\text{Sr}_2\text{FeTi}_{1-x}\text{Nb}_x\text{O}_{6-\delta}$ and $\text{Sr}_2\text{FeTi}_{1-x}\text{V}_x\text{O}_{6-\delta}$ ($x = 0 - 0.5$) at 800°C in air.....	46
Table 3.5 The maximum power density value and polarization resistance of a SFTNb _x / LSGM/ NiFe cell with different compositions at 800°C	48
Table 3.6 The maximum power density value and polarization resistance of a SFTV _x / LSGM/ NiFe cell at 800°C	51
Table 3.7 The maximum power density value and polarization resistance of a SSC/ LSGM/ SFTNb _x cell with different compositions at 800°C	53
Table 3.8 The maximum power density value and polarization resistance of a SSC/ LSGM/ SFTV _x cell with different compositions at 800°C	56
Table 3.9 Calculated Ratio of Fe $2p_{3/2}$ for SFT and $\text{Sr}_2\text{FeTi}_{1-x}\text{Nb}_x\text{O}_{6-\delta}$ ($x = 0.05, 0.10, 0.50$) oxides	63
Table 3.10 Calculated ratio between adsorbed oxygen and lattice oxygen for SFT and $\text{Sr}_2\text{FeTi}_{1-x}\text{Nb}_x\text{O}_{6-\delta}$ ($x = 0.05, 0.10, 0.50$) oxides	64
Table 3.11 Calculated Ratio of Fe $2p_{3/2}$ for SFT and SFTV05 oxides.....	68

Table 3.12 Calculated ratio between adsorbed oxygen and lattice oxygen for SFT and SFTV05 oxides	69
--	----



LIST OF FIGURES

	Page
Figure 1.1 Operating principle of a solid oxide fuel cell	4
Figure 1.2 Conductivity of common electrolyte materials (YSZ, ScSZ, GDC and LSGM) for SOFC.....	6
Figure 1.3 The oxygen reduction mechanism for cathode SOFC	7
Figure 1.4 The hydrogen oxidation mechanism for anode SOFC.....	9
Figure 1.5 SEM cross section of Ni-YSZ anode	10
Figure 1.6 Perovskite structure with a 3D network of corner-shared (BO ₆) octahedra incorporated the 12-fold coordinated A-cation.....	11
Figure 1.7 Double-perovskite structure with long range B-site cation ordering.....	11
Figure 1.8 Covalent bonds between the oxygen ion p-orbitals and B-cation.....	14
Figure 1.9 Electron hopping mechanism	14
Figure 1.10 Oxide ion transfer mechanism.....	15
Figure 1.11 Saddle point for ion transport	16
Figure 1.12 Fuel cell polarization curve.....	17
Figure 1.13 Power density curve	19
Figure 1.14 Nyquist plot with the equivalent circuit model.....	21
Figure 2.1 DC four point probe measurement	30
Figure 2.2 Schematic diagram of symmetric cell for AC impedance measurement	31
Figure 2.3 Schematic of the single cell measurement for AC impedance and SOFC performance	32
Figure 3.1 XRD patterns of SFT and Sr ₂ FeTi _{1-x} Nb _x O _{6-δ} (x = 0.05 – 0.50) at room temperature.....	33

Figure 3.2 XRD patterns of SFT and $\text{Sr}_2\text{FeTi}_{1-x}\text{V}_x\text{O}_{6-\delta}$ ($x = 0.05 - 0.50$) at room temperature.....	34
Figure 3.3 The magnification of main peak in XRD patterns of SFT and $\text{Sr}_2\text{FeTi}_{1-x}\text{Nb}_x\text{O}_{6-\delta}$ ($x = 0.05 - 0.50$)	34
Figure 3.4 The magnification of main peak in XRD patterns of SFT and $\text{Sr}_2\text{FeTi}_{1-x}\text{V}_x\text{O}_{6-\delta}$ ($x = 0.05 - 0.50$)	36
Figure 3.5 Temperature dependence on electrical conductivity for SFT in air (a) and Arrhenius plots of the electrical conductivity for SFT (b).....	38
Figure 3.6 Electrical conductivity of $\text{Sr}_2\text{FeTi}_{1-x}\text{Nb}_x\text{O}_{6-\delta}$ ($x = 0.05 - 0.50$) with SFT in air as a function of temperature	40
Figure 3.7 Arrhenius plot of $\text{Sr}_2\text{FeTi}_{1-x}\text{Nb}_x\text{O}_{6-\delta}$ ($x = 0.05 - 0.50$) for the electrical conductivity	41
Figure 3.8 Electrical conductivity of $\text{Sr}_2\text{FeTi}_{1-x}\text{V}_x\text{O}_{6-\delta}$ ($x = 0.05 - 0.50$) with SFT in air as a function of temperature	42
Figure 3.9 Arrhenius plot of $\text{Sr}_2\text{FeTi}_{1-x}\text{V}_x\text{O}_{6-\delta}$ ($x = 0.05 - 0.50$) for the electrical conductivity	43
Figure 3.10. Typical impedance spectra of SFT, $\text{Sr}_2\text{FeTi}_{1-x}\text{Nb}_x\text{O}_{6-\delta}$ ($x = 0.00 - 0.50$) (a) and $\text{Sr}_2\text{FeTi}_{1-x}\text{V}_x\text{O}_{6-\delta}$ ($x = 0.00 - 0.50$) (b) with LSGM electrolyte at 800°C in air.....	45
Figure 3.11 Cell voltage and power density as functions of current density for the single cell with $\text{Sr}_2\text{FeTi}_{1-x}\text{Nb}_x\text{O}_{6-\delta}$ ($x = 0.00, 0.05, 0.10, 0.20, 0.50$) cathode at 800°C ...	47
Figure 3.12 Impedance spectra of single cell with $\text{Sr}_2\text{FeTi}_{1-x}\text{Nb}_x\text{O}_{6-\delta}$ ($x = 0.00, 0.05, 0.10, 0.20, 0.50$) cathode at 800°C	48
Figure 3.13 Cell voltage and power density as functions of current density for the single cell with $\text{Sr}_2\text{FeTi}_{0.95}\text{Nb}_{0.05}\text{O}_{6-\delta}$ cathode over the temperature range from 600 – 800°C	49
Figure 3.14 Cell voltage and power density as functions of current density for the single cell with $\text{Sr}_2\text{FeTi}_{1-x}\text{V}_x\text{O}_{6-\delta}$ ($x = 0.00, 0.05, 0.10, 0.20, 0.50$) cathode at 800°C.....	50

Figure 3.15 Impedance spectra of single cell with $\text{Sr}_2\text{FeTi}_{1-x}\text{V}_x\text{O}_{6-\delta}$ ($x = 0.00, 0.05, 0.10, 0.20, 0.50$) cathode at 800°C	50
Figure 3.16 Cell voltage and power density as functions of current density for the single cell with $\text{Sr}_2\text{FeTi}_{0.95}\text{Nb}_{0.05}\text{O}_{6-\delta}$ cathode over the temperature range from $600 - 800^\circ\text{C}$	51
Figure 3.17 Cell voltage and power density as functions of current density for the single cell with $\text{Sr}_2\text{FeTi}_{1-x}\text{Nb}_x\text{O}_{6-\delta}$ ($x = 0.00, 0.05, 0.10, 0.20, 0.50$) anode at 800°C	52
Figure 3.18 Impedance spectra of single cell with $\text{Sr}_2\text{FeTi}_{1-x}\text{Nb}_x\text{O}_{6-\delta}$ ($x = 0.00, 0.05, 0.10, 0.20, 0.50$) anode at 800°C	53
Figure 3.19 Cell voltage and power density as functions of current density for the single cell with $\text{Sr}_2\text{FeTi}_{0.95}\text{Nb}_{0.05}\text{O}_{6-\delta}$ anode over the temperature range from $600 - 800^\circ\text{C}$	54
Figure 3.20 Cell voltage and power density as functions of current density for the single cell with $\text{Sr}_2\text{FeTi}_{1-x}\text{V}_x\text{O}_{6-\delta}$ ($x = 0.00, 0.05, 0.10, 0.20, 0.50$) anode at 800°C	55
Figure 3.21 Impedance spectra of single cell with $\text{Sr}_2\text{FeTi}_{1-x}\text{V}_x\text{O}_{6-\delta}$ ($x = 0.00, 0.05, 0.10, 0.20, 0.50$) anode at 800°C	55
<i>Figure 3.22 Cell voltage and power density as functions of current density for the single cell with $\text{Sr}_2\text{FeTi}_{0.95}\text{V}_{0.05}\text{O}_{6-\delta}$ anode over the temperature range from $600 - 800^\circ\text{C}$</i>	<i>56</i>
Figure 3.23 Cell voltage and power density as functions of current density for the symmetrical cell with SFT, SFTNb05 and SFTV05 electrode at 800°C	57
Figure 3.24 XPS spectra of Sr 3d for SFT and $\text{Sr}_2\text{FeTi}_{1-x}\text{Nb}_x\text{O}_{6-\delta}$ ($x = 0.05, 0.10, 0.50$) at room temperature.....	58
Figure 3.25 XPS spectra of Ti 2p for SFT and $\text{Sr}_2\text{FeTi}_{1-x}\text{Nb}_x\text{O}_{6-\delta}$ ($x = 0.05, 0.10, 0.50$) at room temperature.....	59
Figure 3.26 XPS spectra of Nb 3d for SFT and $\text{Sr}_2\text{FeTi}_{1-x}\text{Nb}_x\text{O}_{6-\delta}$ ($x = 0.05, 0.10, 0.50$) at room temperature.....	60

Figure 3.27 XPS spectra of Fe 2p for SFT and $\text{Sr}_2\text{FeTi}_{1-x}\text{Nb}_x\text{O}_{6-\delta}$ ($x = 0.05, 0.10, 0.50$) at room temperature.....	61
Figure 3.28 XPS spectra of O 1s for SFT and $\text{Sr}_2\text{FeTi}_{1-x}\text{Nb}_x\text{O}_{6-\delta}$ ($x = 0.05, 0.10, 0.50$) at room temperature.....	64
Figure 3.29 XPS spectra of Sr 3d for SFT and SFTV05 samples at room temperature	65
Figure 3.30 XPS spectra of Ti 2p for SFT and SFTV05 samples at room temperature	66
Figure 3.31 XPS spectra of V 2p for SFTV05 sample at room temperature.....	67
Figure 3.32 XPS spectra of Fe 2p for SFT and SFTV05 samples at room temperature	67
Figure 3.33 XPS spectra of O 1s for SFT and SFTV05 samples at room temperature .	68
Figure 3.34 Thermal expansion curves of SFT, SFTNb05 and SFTV05 as a function temperature in air.....	70
Figure 3.35 XRD pattern of SFT powder, LSGM powder and LSGM-SFT mixture calcined at 900°C for 5 hours in air.....	71
Figure 3.36 XRD pattern of SFTNb05 powder, LSGM powder and LSGM-SFTNb05 mixture calcined at 900°C for 5 hours in air	72
Figure 3.37 XRD pattern of SFTV05 powder, LSGM powder and LSGM-SFTV05 mixture calcined at 900°C for 5 hours in air.....	72

LIST OF ABBREVIATION

SOFC	Solid oxide fuel cell
AFC	Alkaline fuel cell
PEMFC	Polymeric electrolyte membrane fuel cell
PAFC	Phosphoric acid fuel cell
MCFC	Molten carbonate fuel cell
ORR	Oxygen reduction reaction
HOR	Hydrogen oxidation reaction
TPB	Triple-phase boundary
MIEC	Mixed ionic-electronic conductivity
EIS	Electrochemical impedance spectroscopy
XRD	X-ray diffractometry
XPS	X-ray photoelectron spectroscopy
TEC	Thermal expansion coefficient
T	Temperature
t	Tolerance factor
r	Ionic radii
I	Current
V	Voltage
R_p	Polarization resistance
σ	Electrical conductivity
E_a	Activation energy
P	Power density
Z	Impedance

CHAPTER 1

INTRODUCTION

Nowadays, a rapid rising in human social, economic, and industrial sections causes the demand in energy around the world. Most electrical power generally comes from burning of fossil fuels such as oil, natural gas and coal. The combustion of fossil fuels emits carbon dioxide (CO_2) and sulfur dioxide (SO_2) into the atmosphere and these gases affect badly to the environment and human health, for example, CO_2 causes the phenomenon of global warming [1, 2] and SO_2 is directly harmful to human respiratory system. Because the fossil fuels are a limited quantity and will eventually run out, people are seeking for an alternative energy e.g. solar power, wind energy, hydro energy, geothermal energy, biomass energy, fuel cell, etc., to replace these fuels. The alternative energy must also be renewable energy and environmental-friendly. Among the kinds of alternative energy, fuel cells are one of the interesting energy sources due to power efficiency size reduction, and less CO_2 output.

1.1 Fuel cell [3-5]

A fuel cell is a device that directly converts the chemical energy into electricity power through the electrochemical reaction between hydrogen (or another fuel) and oxygen. Fuel cell works like battery, but there are some significant differences. Fuel cells don't run out or need recharging because they produce electrical energy as long as fuel and oxygen are continuously supplied. Batteries, on the other hand, have a limited amount of available energy based on chemical reactant stored. Some additional advantages of the fuel cells are environmental performance, high efficiency, quiet operation, fuel flexibility (such as hydrogen, methanol, ethanol, etc.) and size reduction. Generally, fuel cells have several types. They are classified by the kind of electrolyte used. Fuel cell types are as follows:

- Alkaline fuel cell (AFC)
- Polymeric electrolyte membrane fuel cell (PEMFC)
- Phosphoric acid fuel cell (PAFC)

- Molten carbonate fuel cell (MCFC)
- Solid oxide fuel cell (SOFC)

The summary of each fuel cell types can be followed in Table 1.1 [4].

1.2 Solid oxide fuel cell (SOFC) [6-10]

SOFC is one of fuel cell types that uses a ceramic compound as the electrolyte and operates at very high temperatures (500 – 1000°C). In comparison to other types of fuel cell, SOFC has high efficiency of electricity production and it can considerably reduce costs. Additionally, there are several advantages of SOFC, for example, no use of expensive catalysts (platinum or ruthenium), long lifetime of cell, tolerance to the fuel impurities such as sulfur and low emission of greenhouse gases (CO₂, SO₂, etc.), and fuel flexibility. However, SOFC has some drawbacks owing to the high operating temperature. For example, the materials used requires durable ceramic component in order to have relative thermal expansion for large temperature range, and the long-term operation for startup and cool down is required for minimizing thermal stress of materials in the cell. However, SOFC has wide range in applications and the main applications are stationary power sources for industry, auxiliary power units (APU) for transportation, and portable power sources, like battery chargers.

Table 1.1 A typical fuel cell

Characteristics	Polymer electrolyte	Alkaline	Phosphoric acid	Molten carbonate	Solid oxide
Operating temperature [°C]	40 – 80	65 – 220	205	650	600 – 1000
Electrolyte	Hydrated polymeric ion exchange membrane	Mobilized or immobilized potassium hydroxide in asbestos matrix	Immobilized liquid phosphoric acid in SiC	Immobilized liquid molten carbonate in LiAlO ₂	Perovskites (ceramics)
Electrodes	Carbon	Platinum	Carbon	Nickel and Nickel oxide	Ceramic based
Catalyst	Platinum	Platinum	Platinum	Electrode material	Electrode material
Cell components	Carbon based	Carbon based	Carbon based	Stainless based	Ceramic based
Charge carrier	H ⁺	OH ⁻	H ⁺	CO ₃ ⁺	O ²⁻
Reaction at the anode	$H_2 \rightarrow 2H^+ + 2e^-$	$H_2 + 2OH^- \rightarrow 2H_2O + CO_2 + 2e^-$	$H_2 \rightarrow 2H^+ + 2e^-$	$H_2 + CO_3^{2-} \rightarrow H_2O + CO_2 + 2e^-$ $CO + CO_3^{2-} \rightarrow 2CO_2 + 2e^-$	$H_2 + O^{2-} \rightarrow H_2O + 2e^-$ $CO + O^{2-} \rightarrow CO_2 + 2e^-$ $CH_4 + 4O^{2-} \rightarrow 2H_2O + CO_2 + 8e^-$
Reaction at the cathode	$O_2 + 4H^+ + 4e^- \rightarrow 2H_2O$	$O_2 + CO_2 + 4e^- \rightarrow 2CO_3^{2-}$	$O_2 + 4H^+ + 4e^- \rightarrow 2H_2O$	$O_2 + CO_2 + 4e^- \rightarrow 2CO_3^{2-}$	$O_2 + 4e^- \rightarrow 2O^{2-}$

1.2.1 SOFC operation [11, 12]

SOFC consists of three main parts; an electrolyte, an anode, and a cathode. The electrolyte is sandwiched between the cathode and the anode, while the cathode and anode are connected by an external circuit as illustrated in Figure 1.1. Oxygen gas (O_2) from air is fed into the cathode and reacts with incoming electrons, which come from the circuit. The combination of oxygen and electrons creates oxide ions (O^{2-}) via the oxygen reduction reaction (ORR) as shown in equation 1.1. The oxide ions then migrate through the electrolyte, which the properties should conduct oxide ions and not conduct electrons, to the anode. Meanwhile, at the anode, these oxide ions combine with hydrogen gas or fuel to liberate electrons and produce water as by-product. This reaction is the hydrogen oxidation reaction, which is presented in equation 1.2, and equation 1.3 displays the overall SOFC reaction. Electrons in the anode flow via the external circuit to the cathode and provide the electricity simultaneously.

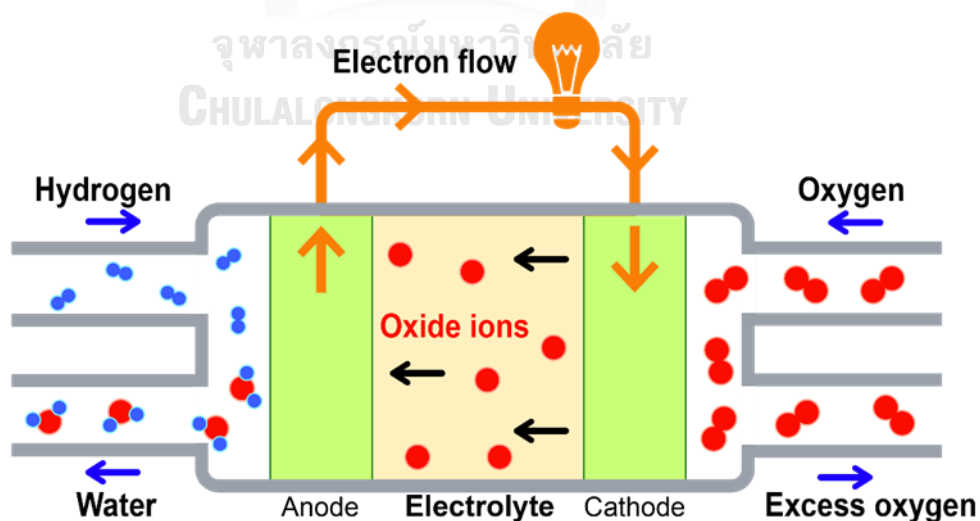
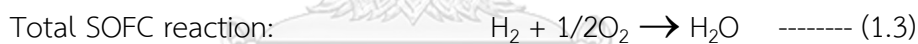


Figure 1.1 Operating principle of a solid oxide fuel cell [12]

1.2.2 SOFC components

As mentioned earlier, SOFC consists of electrolyte, cathode and anode. The properties of materials used as components are very important. There are mainly required properties such as electrical conductivity, catalytic activity, chemical compatibility among different components, thermal stability and matching thermal expansion between interconnect component.

1.2.2.1 Electrolyte

Electrolyte is one of main SOFC component and it is oxide ion conductor materials. The salient features of electrolyte are as follows [13, 14]:

- Electrochemical property: electrolyte must have high ionic conductivity ($\geq 0.1 \text{ S}\cdot\text{cm}^{-1}$ at about 1000°C) because the high ionic conductivity leads to the decreasing of ohmic resistance and it should have low electronic conductivity ($< 10^{-3} \text{ S}\cdot\text{cm}^{-1}$) for preventing oxygen leakage and voltage loss.
- Chemical property: electrolyte needs to have the chemical stability with electrode materials, oxygen (air) and fuels.
- Thermal property: electrolyte must be stable under operating temperature and a good match in thermal expansion coefficient (TEC) with other component of the cell especially electrodes.
- Mechanical property: electrolyte should be durable to fracture and stress.

Many challenge materials have been studied as electrolyte materials of SOFC. Yttria stabilized zirconia (YSZ) is the most common and widely used material as electrolyte in SOFC because it has high ionic conductivity and stability. However, YSZ shows low ionic conductivity at lower operating temperature. Scandia stabilized zirconia (ScSZ) also has higher ionic conductivity and long-term stability than YSZ but high cost of scandium and availability of scandium make ScSZ less attractive in SOFC electrolyte materials [15]. Gadolinium doped ceria (GDC) or cerium gadolinium oxide (CGO) has higher ionic conductivity than YSZ and ScSZ. GDC can operate at low temperature thus it has been considered as great electrolyte materials for intermediate-temperature SOFC (IT-SOFC) application. The drawback of this material is low electronic conduction under reducing conditions due to the associated reduction

of Ce^{4+} to Ce^{3+} [16, 17]. In addition to zirconia and ceria materials which has fluorite structure, lanthanum materials with perovskite structure (ABO_3) is one of interesting electrolyte for SOFC. $LaGaO_3$ based perovskite with strontium substituted on lanthanum site and magnesium substituted on gallium site ($(La_{1-x}Sr_x)(Ga_{1-y}Mg_y)O_3$, LSGM) provides excellent ionic conductivity at low temperature, hence it has great potential to be used as electrolyte at low operating temperature [18, 19]. Nevertheless, the limitation of this material is chemical and mechanical stability and price of gallium. Figure 1.2 displays the conductivity of traditional electrolyte materials worked at low temperature for SOFC.

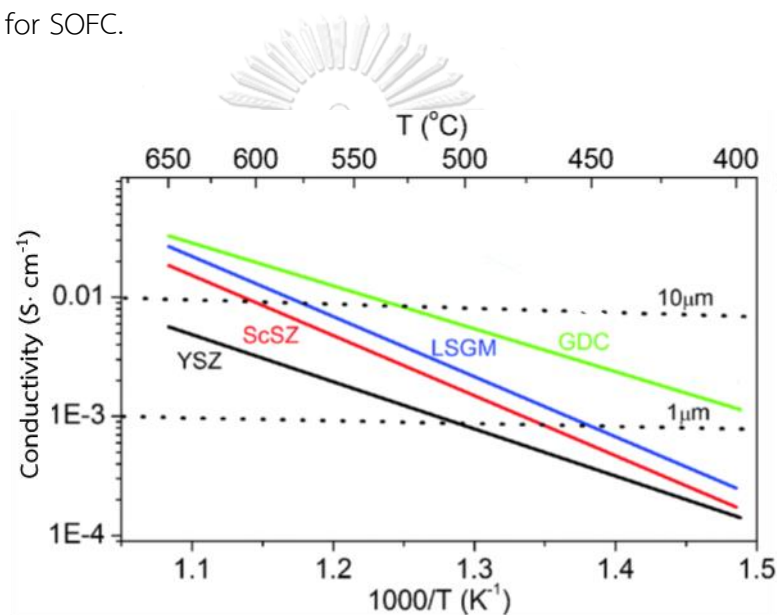


Figure 1.2 Conductivity of common electrolyte materials (YSZ, ScSZ, GDC and LSGM) for SOFC [20]

1.2.2.2 Cathode

The cathode is a contact layer with the electrolyte and involves in the electrochemical reduction of oxygen. The requirements of cathode materials are mostly as follows [21, 22]:

- High electronic conductivity
- High catalytic activity for oxygen reduction and oxygen molecule dissociation
- Chemical compatibility and minimum reactivity with the electrolyte and interconnect materials

- Stability under the oxidizing atmosphere and during cell fabrication as well as cell operation
- Thermal expansion match with other component of the cell, especially electrolyte and interconnect materials
- Sufficient porosity for oxygen gases to diffuse through cathode to cathode-electrolyte interface
- Low cost

For the cathode, the oxygen reduction reaction (ORR) occurs on the electrode-electrolyte-gas interface or triple-phase boundary (TPB) sites. There are several steps of ORR including O_2 gas diffusion, surface exchange processes (such as oxygen adsorption, dissociation and charge transfer), oxide ion diffusion, and oxide ion transfer from electrode into electrolyte [23].

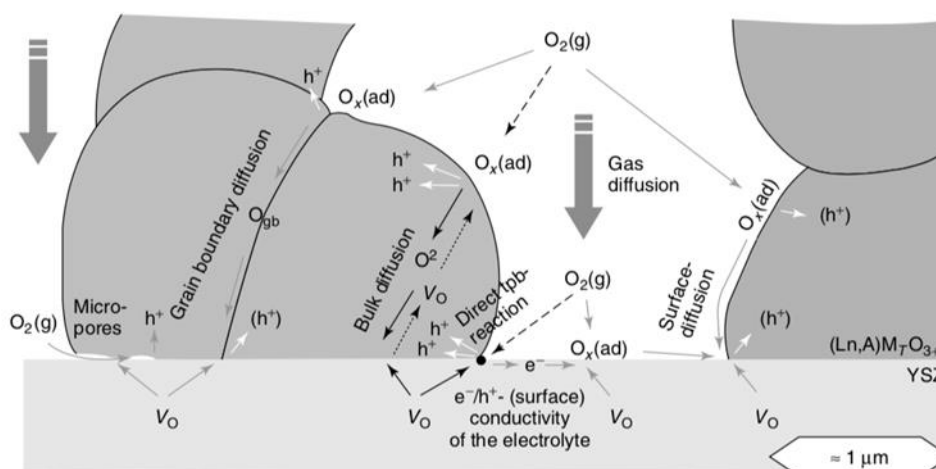


Figure 1.3 The oxygen reduction mechanism for cathode SOFC [23]

A wide range of cathode materials has been investigated for SOFC. The perovskite-based oxide materials have been preferred as a potential SOFC cathode such as lanthanum manganite ($LaMnO_3$, LMO). The substitution of alkaline earth cation e.g. Sr^{2+} , Ca^{2+} on La site can make the formation of oxygen vacancies in order to balance the charge compensation. This reason causes the material to behave as a mixed ionic and electronic conductor (MIEC) [22]. $La_{1-x}Sr_xMnO_3$ (LSM) is also higher electronic conductivity compared to LMO and the TEC values of LSM are good

matching with YSZ electrolyte. Additionally, there have been many studies on increasing conductivity of lanthanum-based perovskite [24] e.g. (La, Sr)MO₃ systems with M = Mn, Co, Fe. As compared with the ferrites and manganites, the cobaltites have higher electrical conductivity because they offer higher rates of oxide ion diffusion and faster kinetics of oxygen reduction. However, the cobaltites have higher TEC than YSZ electrolyte [25]. Furthermore, these materials are also reactive to YSZ but a thin layer of GDC can reduce the chemical reaction of these cathode with YSZ [11]. For another cathode, Sm_{0.5}Sr_{0.5}CoO₃ (SSC) is of interest materials since SSC exhibits lower polarization resistance, higher electrical conductivity and better performance compare to LSM [26].

1.2.2.3 Anode

The one important component of SOFC is anode, which implicates the oxidation of the fuel. The requirements of anode material properties are as follows [21, 22]:

- High catalytic activity for the electrochemical oxidation of hydrogen (H₂) or carbon monoxide (CO) and the other fuels.
- High electronic conductivity
- Adequate porosity for the gas permeation
- Matching of thermal expansion coefficient
- Chemical stability with the electrolyte and interconnect
- Low cost

The candidates of the anode materials are the transition metals, for example, Nickel (Ni), Iron (Fe), Ruthenium (Ru), Cobalt (Co), Platinum (Pt), Palladium (Pd) and Gold (Au). The best metallic anode is Ni because of a good effective catalyst for the hydrogen oxidation reaction (HOR) [27].

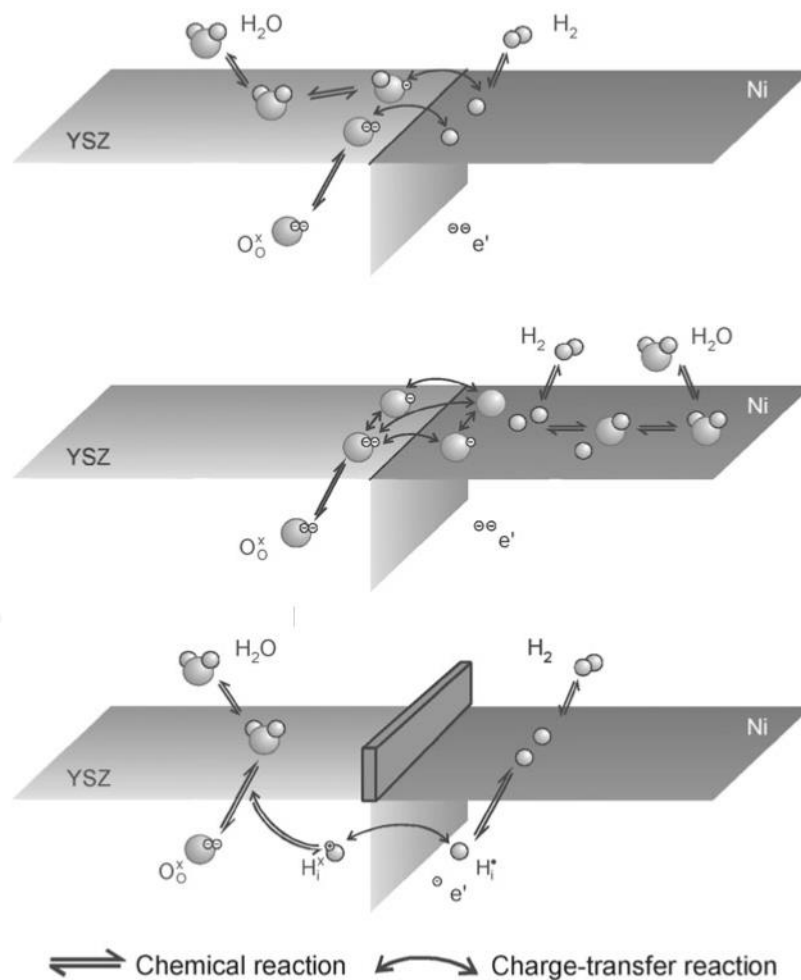


Figure 1.4 The hydrogen oxidation mechanism for anode SOFC [28]

However, pure Ni metal is high TEC and tends to aggregate during the operating temperature. Ni-YSZ anode was designed to have the YSZ particles surrounding the Ni particles, as a result the TEC of anode closed to the TEC of electrolyte [29, 30]. In addition, the catalytic activity of Ni-YSZ is higher than that of Ni metal anode because the Ni-YSZ cermet has lower polarization resistance than the pure Ni electrode. Nevertheless, the hydrocarbon fuels e.g. methane fed to anode for long-term operation cause carbon deposition on the Ni-YSZ anode surface, which blocks gas to access the active area. Another problem of Ni-YSZ material is the sulfur impurities from fuels, that can poison the tolerance of anode [31, 32].

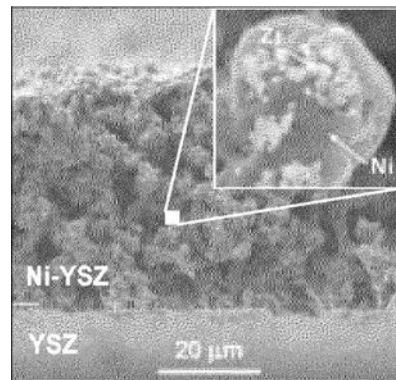


Figure 1.5 SEM cross section of Ni-YSZ anode [30]

Besides Ni-YSZ, an alternatively anode of metal-supported SOFC is Ni-Fe bimetal anode. T. Ishihara et. al. [33] found that the Ni-Fe electrode with the LSGM electrolyte can enhance the anodic catalytic activity. The addition of Fe into metallic Ni-based anode will not only significantly decreased the TEC of the anode but also suppressed coke formation in the hydrocarbon fuels [34, 35]. Furthermore, the ceramic anodes, such as strontium titanate (SrTiO_3), Nb-doped SrTiO_3 , $\text{Sr}_2\text{MgMoO}_{6-\delta}$, have been proposed as the alternative anode materials. These anodes show good performance in reducing carbon deposition and improving sulfur tolerance, but these materials exhibit lower electrical conductivity compared to the Ni-based anodes [36-38].

1.3 Double Perovskite Oxide [39-45]

The double perovskite oxide materials have been investigated for electrode and electrolyte materials in SOFC due to the chemical and physical properties of the perovskite such as chemical flexibility, electronic conductivity, ionic conductivity and good catalyst. The double perovskite oxides have a crystal structure like the perovskite oxides. Normally, the general formula of perovskite is ABO_3 with a face-centered cubic structure while the double perovskite formula is $\text{A}_2\text{BB}'\text{O}_6$ (double B-site) with a layer-type structure. The perovskites consist of two cations, A and B. Cation A is alkaline earth or lanthanide ions especially Ca, Sr, Ba, La, and cation B is transition ions. The perovskite unit cell possess the structure which the larger A cations located at the corners of the cube, the B-site cations occupied the body center and an oxygen anion located at the face center. The crystal structures of the perovskite and double

perovskite are shown in Figure 1.6 and Figure 1.7, respectively. In Figure 1.6, the A-site has twelve-coordinated oxygen ions whereas the B-site has sixfold oxygen coordination or octahedrally coordination (BO_6). For double perovskite structure, two different B-site (B and B' cations) cations are observed and these two ions are alternated in each layer, as presented in Figure 1.7.

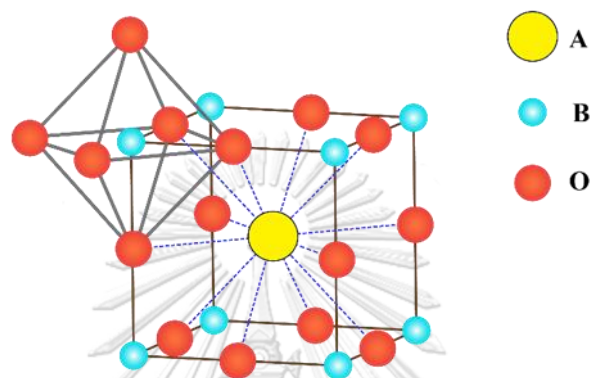


Figure 1.6 Perovskite structure with a 3D network of corner-shared (BO_6) octahedra incorporated the 12-fold coordinated A-cation [39]

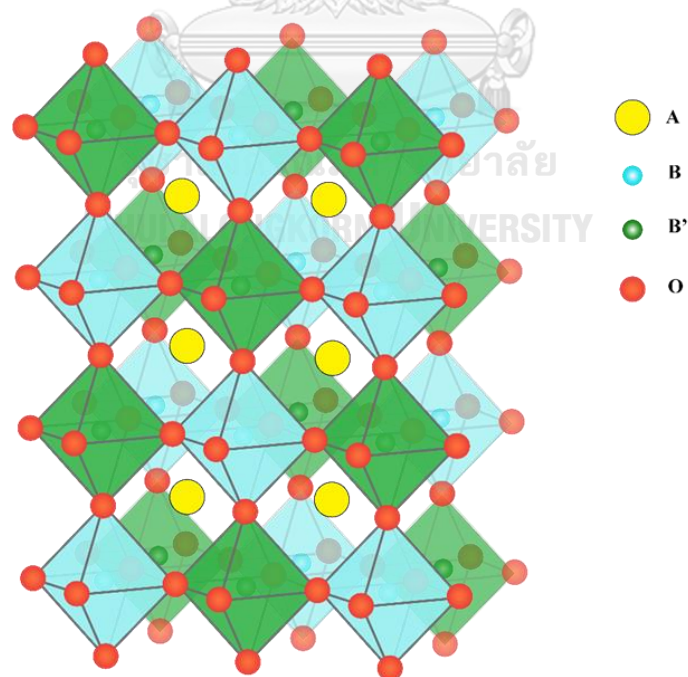


Figure 1.7 Double-perovskite structure with long range B-site cation ordering [40]

The stability of the perovskite structure is popularly predicted by the unity of the Goldschmidt tolerance factor (t) as shown in equation 1.4. This factor investigates the distortions of the structure and the relative strengths of the A-O and B-O bonds. Usually, the perovskite-type structure is obtained in the range $0.75 \leq t \leq 1.0$ and the perfect perovskite has closer to $t = 1$, when the A cation and the oxygen ion are the same size. For the ideal perovskite, the O-B-O bond angle is 180° or it is linear. The deviation of cubic symmetry arises from the mismatch in size of the cation and anion, which results in the angle change of O-B-O bonds and the tilting of the BO_6 octahedra. If t decreases from 1, the lattice structure deforms towards the lower A-site coordination; as a result, the cubic structure changes to rhombohedral. For $t > 1$, on the other hand, the distortion of perovskite structure to hexagonal and orthorhombic structures is found due to the shared BO_6 octahedra faces instead of corners. For double perovskite structure, the tolerance factor can be written as equation 1.5.

$$t = \frac{r_A + r_O}{\sqrt{2} \times (r_B + r_O)} \quad \text{----- (1.4)}$$

$$t = \frac{r_A + r_O}{\sqrt{2} \times \left(\frac{r_B}{2} + \frac{r'_B}{2} + r_O\right)} \quad \text{----- (1.5)}$$

Where; t = the Goldschmidt tolerance factor (t)

r_A = the ionic radii of A cation

r_B = the ionic radii of B cation

r'_B = the ionic radii of B' cation

r_O = the ionic radii of oxygen ion

Moreover, the mixed ionic-electronic conductivity (described in the next section) is one of the outstanding features for the perovskite oxides. The partial substitution for B-site cations may influence the electrical property of perovskite compounds owing to some parameters such as ionic radii and electronic configuration. Thus, many current researches have been aimed to develop the perovskite oxide

materials by doping various metal cations into the perovskite structure. Hence that can improve the efficiency of the perovskite properties.

1.4 Electrical Conductivity [46-49]

The mixed ionic-electronic conductivity (MIEC) is the interesting property of perovskite. MIEC materials can conduct both ions and electronic charge carriers (electron/hole) simultaneously. The ionic and electronic conductivity for the perovskite materials are described in details below.

1.4.1 Electronic conductivity

The electronic conduction carries on through electrons or holes along the B-O-B bonding of the BO_6 octahedra network in the perovskite structure. Naturally, the overlapping between the d orbitals of B-site cations and the p orbitals of oxygen ions forms the B-O covalent bond as illustrated in Figure 1.8, which displays the overlapping and the covalent bonds between the B cation t_{2g} (d) orbitals and the oxygen ion p_π orbitals. Additionally, the covalency of the B-O-B bond influences the electrical property of the perovskite oxides. The colinear overlap of all B-O bonding (B-O-B angle about 180°) might also exhibit the larger B3d-O2p overlap. Therefore, the electrons/holes can transport from the t_{2g} orbital into the neighboring t_{2g} orbital B-site cation via the p_π orbital of the oxygen anion. This pathway is commonly known as the electron hopping mechanism. In addition, there are other ways for the generative electronic conductivity including thermal excitation, deviation from stoichiometry and doping.

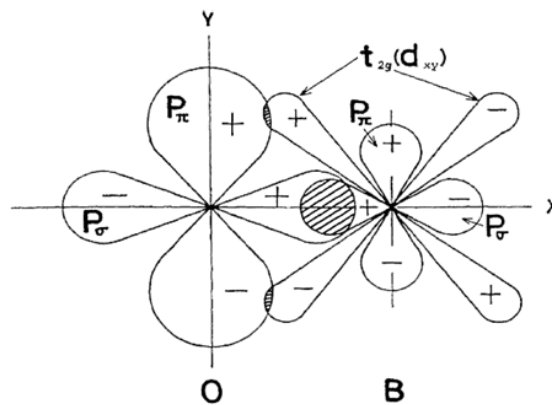


Figure 1.8 Covalent bonds between the oxygen ion p-orbitals and B-cation t (d) orbitals [46]

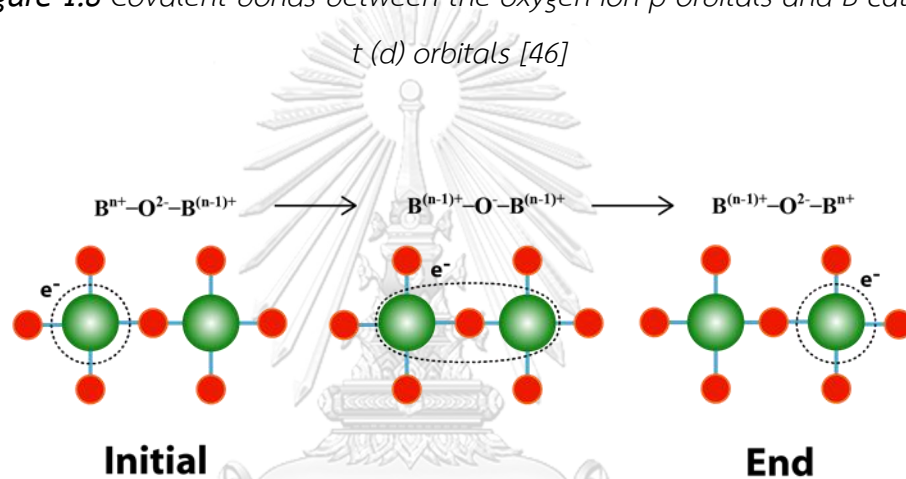


Figure 1.9 Electron hopping mechanism [47]

1.4.2 Ionic conductivity

The ionic conduction occurs via the oxygen vacancy mechanism. The vacant site of the oxygen ions in the perovskite structure is generated by thermal excitation for the intrinsic defect, and by the cation doping for the extrinsic defect. The oxide ions (O^{2-}) in the lattice then diffuse to the nearby oxygen vacancies, which is called the ion transport, and result in ionic conductivity. Figure 1.10 shows the model of the oxide ion transport in the perovskite structure.

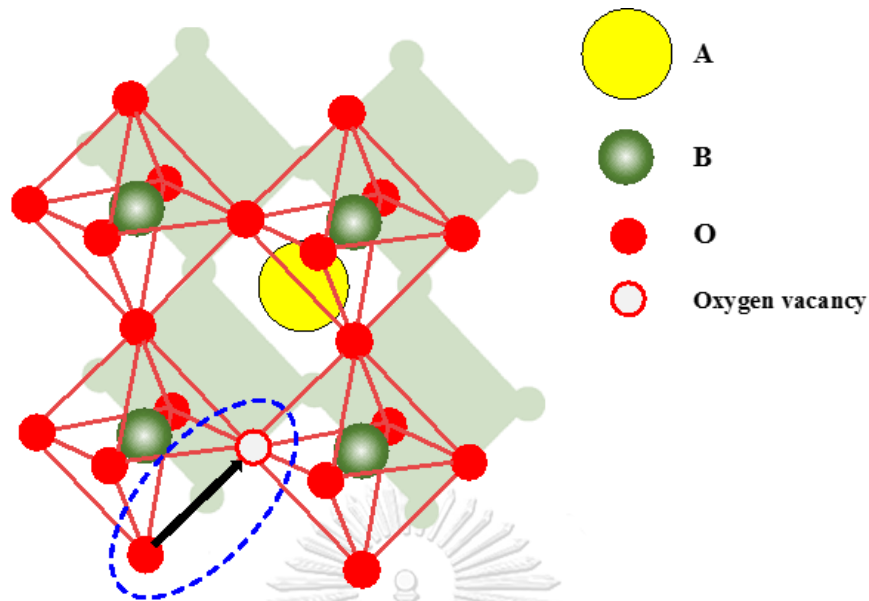


Figure 1.10 Oxide ion transfer mechanism [46]

In the perovskite oxide, the substitution of the lower valence state cations can create the oxygen vacancies due to the charge compensation. Subsequently, the increasing of oxygen vacancy concentrations essentially increases the ionic conductivity. However, the oxygen ion conductivity not only depends on the oxygen vacancy, but also the geometrical factors. The higher the symmetry of perovskite structure ($t \approx 1$), the greater the ionic conductivity is. For a transfer of oxide ions from one site to the neighboring vacancy along the BO₆ octahedral edge, an oxide ion has to pass through a saddle point, which is constructed by two cations of A-site and one cation of B-site, as shown in Figure 1.11. The saddle point is described in term of a critical radii (r_{cr}), which defines the maximum size of the mobile ion to be passed. Also, the larger critical radii can enhance the oxygen ionic conductivity. This critical radii can be calculated by equation 1.6 and 1.7. Therefore, the increasing radii of B cation and the decreasing radii of A cation can encourage the larger critical radii.

$$r_{cr} = \frac{a_0 \left(\frac{3}{4} a_0 - \sqrt{2} r_B \right) + r_B^2 - r_A^2}{2(r_A - r_B) + \sqrt{2} a_0} \quad \text{----- (1.6)}$$

$$a_0 \approx V_{cell}^{1/3} = 2.37 r_B + 2.47 - 2.00(t^{-1} - 1) \quad \text{----- (1.7)}$$

Where; r_{cr} = the critical radii

r_A = the radii of A ion

r_B = the radii of B ion

$V^{1/3}$ = pseudo cubic lattice parameter

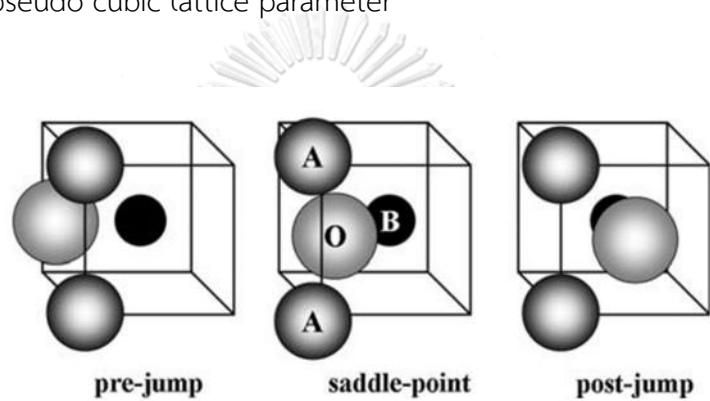


Figure 1.11 Saddle point for ion transport [46]

Generally, the electrical conductivity of perovskite oxide is carried out using a four-point probe technique for SOFC application. This technique measures both electronic and ionic conductivity. Thus, the electrical conductivity can be expressed as the sum of the electric and ionic components. This conductivity is also the complex property related to the mobility and concentration terms of all charge carriers, as presented in the equation 1.8 [50].

$$\sigma = C\mu q \quad \text{----- (1.8)}$$

Where; σ = the electrical conductivity ($S \cdot cm^{-1}$)

C = the concentration of the carried charge (cm^{-3})

μ = the mobility of the carried charge ($m^2 V^{-1} s^{-1}$)

q = the charge (coulombs)

1.5 Fuel Cell Characterization

Two important techniques are commonly used for investigating the cell performance in SOFCs are a current-voltage (i-V) measurement and the electrochemical impedance spectroscopy (EIS). These two techniques are briefly described in this section.

1.5.1 Current-Voltage (i-V) measurement [50, 51]

The current-voltage (i-V) measurement is quantitatively used for evaluating the fuel cell performance and the power density. The current-voltage (i-V) curve displays the voltage output of the fuel cell for a given current density loading. Also, a typical i-V curve for the fuel cell is shown in Figure 1.12.

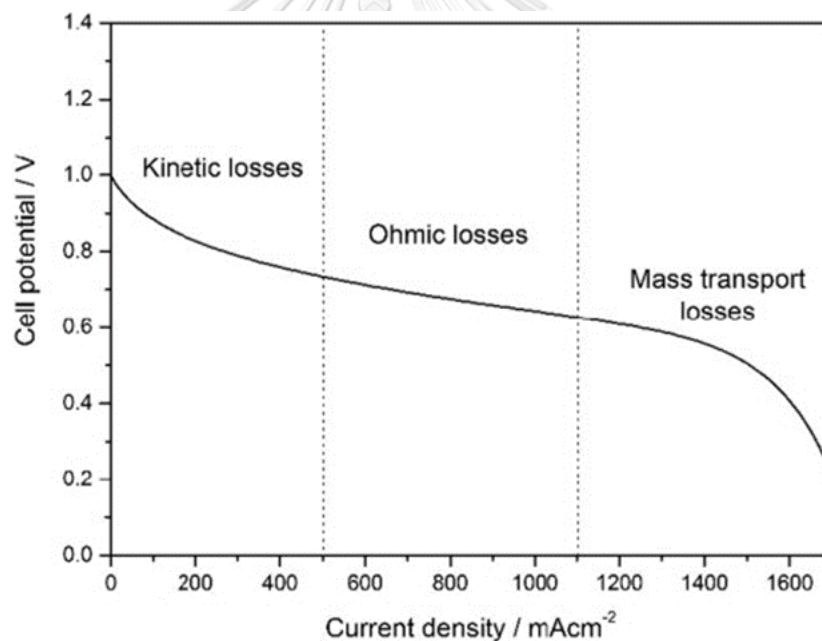


Figure 1.12 Fuel cell polarization curve [51]

The x axis of this curve is the current density, which a unit is amperes per square centimeter ($A \cdot cm^{-2}$). For the ideal fuel cell, the cell voltage would maintain a constant of the theoretical voltage for any amount of current supplied and the ideal cell voltage is determined by the thermodynamics. However, the cell voltage of a real

fuel cell is lower than the ideal fuel cell because of irreversible losses in the fuel cell.

There are three major types of the fuel cell losses, as described below:

- At low current densities; the kinetic losses come from the kinetics of electrochemical reactions
- At moderate current densities; the ohmic losses are due to the ionic and electronic conduction
- At high current densities; the concentration losses are due to the mass transport

Therefore, the operation voltage of the fuel cell can be written as equation 1.9.

$$V = E_{thermo} - \eta_{act} - \eta_{ohmic} - \eta_{conc} \quad \text{----- (1.9)}$$

Where; V = the real voltage

E_{thermo} = the thermodynamically predicted voltage

η_{act} = the activation loss due to electrochemical reaction kinetics

η_{ohmic} = the ohmic loss due to electrical resistance in fuel cell

η_{conc} = the concentration loss due to mass transport

The power density of fuel cell can be calculated from the current and voltage as equation 1.10 and the common power density curve is displayed in Figure 1.13 with a function of the current density. The fuel cell which has high performance exhibits less losses and higher cell voltage for the current loading.

$$P = IV \quad \text{----- (1.10)}$$

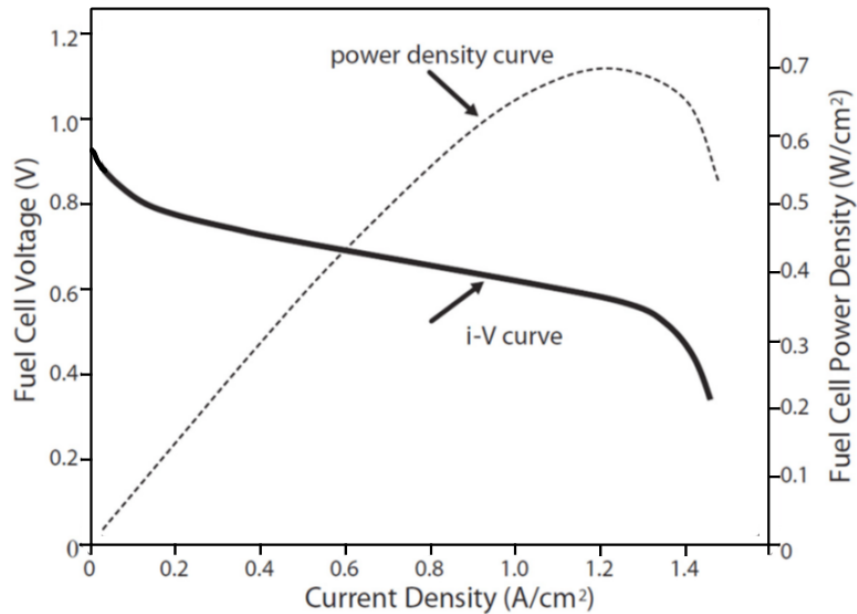


Figure 1.13 Power density curve [52]

1.5.2 Electrochemical Impedance Spectroscopy (EIS) [50, 53-55]

Since the polarization curve in a previous section is not completely provided the insightful information of the cell resistance, electrochemical impedance spectroscopy (EIS) is a widely used technique for distinguishing the different losses of fuel cell. EIS method is made by applying the small sinusoidal perturbation potential to the cell and then monitoring the responsive current (AC) signal with the same frequency. Technically, the analytical EIS applies a wide range of frequency to the cell and consequently recording the variations in phase and magnitude of the cell voltage and current with the frequency, which can be determined in term of impedance Z .

$$Z = \frac{V(t)}{i(t)} = \frac{V_0 \cos(\omega t)}{i_0 \cos(\omega t - \phi)} = Z_0 (\cos \phi + j \sin \phi) \quad \text{----- (1.11)}$$

Where; Z = the impedance

$V(t)$ = the potential at time

$i(t)$ = the current at time

ω = the radial frequency

ϕ = the phase shift

$j =$ the imaginary number ($\sqrt{-1}$)

Therefore, the complex impedance is:

$$Z = Z_{real} - Z_{imag} \quad \text{----- (1.12)}$$

When; $Z_{real} = Z_0 \cos \phi$ and $Z_{imag} = Z_0 j \sin \phi$

Typically, EIS data for the fuel cell are most often represented in Nyquist plots, which are plotted the real impedance (Z_{real}) of the cell on the x axis versus the imaginary impedance (Z_{imag}) on the y axis, as shown in Figure 1.14. The semi-circle curve of the Nyquist plot can also be deconvoluted for an equivalent circuit model of the processes that occurs inside the fuel cell, as illustrated in Figure 1.14. In addition, the intercept value on the real impedance axis at high frequency is the ohmic resistance (R_o), which consists of the ohmic resistance of the electrolyte, the contact of electrode with collector and the wires. The difference between the high frequency and the low frequency intercept on real axis corresponds to the polarization resistance (R_p). Furthermore, the charge transfer reaction at the interface between electrolyte and electrode can be observed from the high frequency arcs, while the low frequency arcs were relevant to the molecular oxygen adsorption, dissociation and diffusion processes in the electrode material [56-60].

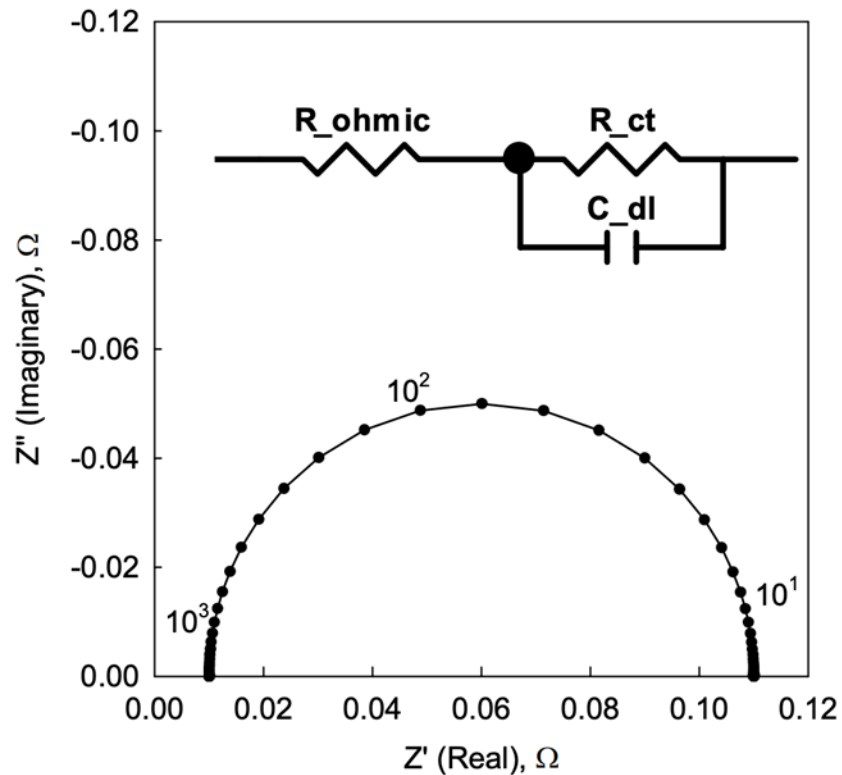


Figure 1.14 Nyquist plot with the equivalent circuit model [55]

1.6 Literature Review

In SOFC, it has long been recognized that high operating temperature causes some disadvantage such as short lifetime of the cell and corrosion of the material. At present the development of intermediate temperature SOFC (IT-SOFC) is introduced in order to reduce the operating temperature to 600 – 800°C. However, the decreasing of operating temperature not only limits the electrode kinetics but also highly promotes the activation polarization and concentration polarization. Thus, it is necessary to develop a new electrode material for IT-SOFC. A $\text{Sr}_2\text{FeTiO}_{6.8}$ (SFT) double perovskite is one of many interesting materials for IT-SOFC electrode because it shows mixed ionic-electronic conductivity property and it can be used as both cathode and anode. In contrast, the electrical conductivity of SFT oxide is rather low, thus this research is aimed to improve the conductivity of this material in order to be a high potential electrode for IT-SOFC. Some related researches are also briefly summarized in below.

According to W. Jung et. al. study on the impedance of $\text{SrTi}_{1-x}\text{Fe}_x\text{O}_{3-\delta}$ ($x = 0.05 - 0.80$) cathode with YSZ electrode. The SFT cathode exhibited the mixed ionic-electronic behavior. The SFT material showed the low area specific resistance (ASR) and the surface exchange coefficient value virtually equal to those values of popular $(\text{La, Sr})(\text{Co, Fe})\text{O}_3$ (LSCF) cathode. Thus, the SFT mixed conductor can be the suitable cathode material [61].

W. Li et. al. prepared $\text{Sr}_2\text{FeTiO}_{6-\delta}$ (SFT) by a solid state reaction method and introduced the SFT material as a promising good electrode for IT-SOFC regarding to its properties. The electrical conductivity of SFT material was $2.83 - 2.33 \text{ S}\cdot\text{cm}^{-1}$ at $600 - 800^\circ\text{C}$ and thermal expansion coefficient in the temperature range of $30 - 1000^\circ\text{C}$ was $16.8 \times 10^{-6} \text{ K}^{-1}$. Also, the single cell performance of SFT cathode with the SDC electrolyte and NiO-SDC anode was $441 \text{ mW}\cdot\text{cm}^{-2}$ at 800°C and the area specific resistance was found to be $0.051 \Omega\cdot\text{cm}^2$ at 800°C . The maximum power density of symmetrical single cell for SFT/SDC/SFT configuration was $335 \text{ mW}\cdot\text{cm}^{-2}$ at 800°C [62].

Q. Zhou et. al. reported the potential of new SOFC cathode by substitution of Mo on Ti-site in SFT structure ($\text{Sr}_2\text{FeTi}_{0.75}\text{Mo}_{0.25}\text{O}_{6-\delta}$, SFTM). The SFTM material had a good chemical compatibility with SDC electrolyte and a maximum electrical conductivity value of $2.31 \text{ S}\cdot\text{cm}^{-1}$ at 500°C . The thermal expansion coefficient of SFTM oxide was $13.6 \times 10^{-6} \text{ K}^{-1}$, which was closed to that of electrolyte material. The polarization resistance was $0.4 \Omega\cdot\text{cm}^2$ at 800°C for SFTM as electrode and SDC as electrolyte. The single cell of the SFTM cathode on SDC electrolyte with NiO-SDC as anode reached the maximum power density value of $394 \text{ mW}\cdot\text{cm}^{-2}$ [63].

B. Niu et. al. suggested the double perovskite $\text{Sr}_2\text{TiFe}_{1-x}\text{Mo}_x\text{O}_{6-\delta}$ ($x = 0.1, 0.2$) as promising candidate materials for SOFC commercials. The $\text{Sr}_2\text{TiFe}_{1-x}\text{Mo}_x\text{O}_{6-\delta}$ ($x = 0.1, 0.2$) cathodes were prepared by the traditional solid-state reaction and demonstrated good structure stability, good chemical compatibility, and thermal expansion coefficient matching with the common electrolyte under operating temperature, compared to the Mo substitution on Ti-site in SFT. The electrolyte-supported symmetrical single cell with $\text{Sr}_2\text{TiFe}_{0.9}\text{Mo}_{0.1}\text{O}_{6-\delta}$ electrode showed the maximum power density of $573 \text{ mW}\cdot\text{cm}^{-2}$ in H_2 fuel and no sign of any degradation on electrochemical

stability test. Besides, the materials can resist carbon deposition and sulfur poisoning better than the traditional anode materials [64].

G. Y. Lee et. al. investigated the properties of $\text{La}_{0.8}\text{Sr}_{0.05}\text{Ca}_{0.15}\text{CrO}_3$ (LSCC) doped with Cu, Ni and V and found that the electrical conductivity of LSCC at 800°C varied as $34 \text{ S}\cdot\text{cm}^{-1}$, $48 \text{ S}\cdot\text{cm}^{-1}$ and $22 \text{ S}\cdot\text{cm}^{-1}$ for Cu, Ni and V dopant, respectively. However, the V doped-LSCC sample was more stable in a low oxygen partial pressure than Cu and Ni doped-LSCC samples [65].

W. Zhou et. al. suggested the addition of Nb for $\text{SrNb}_{0.1}\text{Co}_{0.9}\text{O}_{3-\delta}$ (SNC) perovskite cathode for low temperature SOFC. The SNC had excellent electrical conductivity around $244 \text{ mW}\cdot\text{cm}^{-2}$ in air at 600°C and $247 - 187 \text{ mW}\cdot\text{cm}^{-2}$ under $P(\text{O}_2) = 1 \times 10^{-5}$ atm in temperature range of 500 – 600°C. The high charge of Nb^{5+} can stabilize the structure to avoid order-disorder phase transition and enhance the charge-transfer process for ORR. However, the materials showed the relatively high thermal expansion value of $19.1 \times 10^{-6} \text{ K}^{-1}$ comparing with the common electrolyte due to the spin state of Co. From overall properties of SNC, it had been suggested that SNC can be a promising cathode material for low temperature SOFC [66].

L. Ding et. al. found that $\text{Sr}_{1-x}\text{Co}_{0.7}\text{Nb}_{0.1}\text{Fe}_{0.2}\text{O}_{3-\delta}$ ($x = 0, 0.05$) perovskite oxide developed a great potential to be a cathode in IT-SOFC. The slight deficiency of Sr in $\text{S}_{0.95}\text{CNF}$ perovskite showed the increasing of oxygen vacancy concentration and oxygen reduction catalytic activity in comparison with SCNF material. The polarization resistance of SCNF and $\text{S}_{0.95}\text{CNF}$ at 700°C was $0.11 \text{ }\Omega\cdot\text{cm}^2$ and $0.18 \text{ }\Omega\cdot\text{cm}^2$, respectively. The charge transfer process was the rate limiting step for SCNF and $\text{S}_{0.95}\text{CNF}$ cathode. Also, the single cell performance of SCNF and $\text{S}_{0.95}\text{CNF}$ cathode with SDC electrolyte-supported were $180 \text{ mW}\cdot\text{cm}^{-2}$ and $208 \text{ mW}\cdot\text{cm}^{-2}$, respectively, at 700°C and the single cell for $\text{S}_{0.95}\text{CNF}$ cathode demonstrated high stability under operating condition [67].

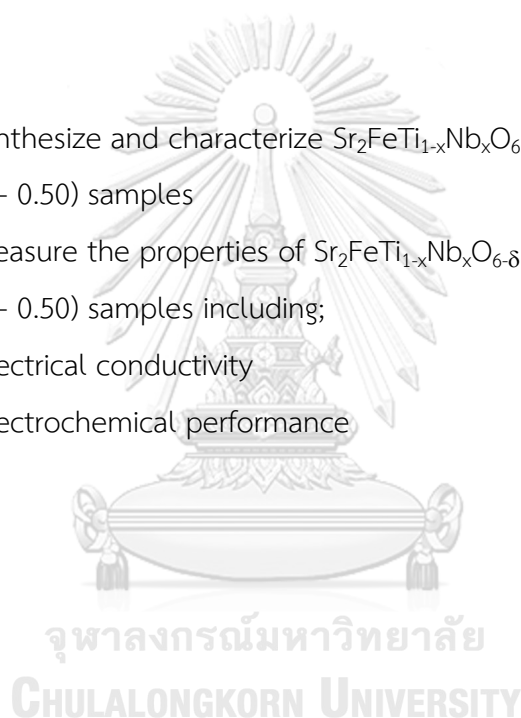
C. Yao et. al. discovered that the Nb and W co-doped $\text{SrFeO}_{3-\delta}$ perovskite, $\text{SrNb}_{0.1}\text{W}_{0.1}\text{Fe}_{0.8}\text{O}_{3-\delta}$ (SNWF), exhibited good performance to be a cathode for IT-SOFC better than the Nb and W single doping, SNF and SWF. That was because SNWF has the oxygen vacancy density more than SNF and SWF. As a result, the SNWF oxide provided better ORR activity, low specific resistance, and high power density compared to those of SNF and SWF samples. The area specific resistance of SNWF, SNF and SWF

at 800°C were 0.071 $\Omega\cdot\text{cm}^2$, 0.087 $\Omega\cdot\text{cm}^2$ and 0.115 $\Omega\cdot\text{cm}^2$, respectively. The maximum output power densities of these cathodes with LSGM electrolyte supported single cell were 832 $\text{mW}\cdot\text{cm}^{-2}$, 772 $\text{mW}\cdot\text{cm}^{-2}$ and 712 $\text{mW}\cdot\text{cm}^{-2}$ at 750°C for SNWF, SNF and SWF, respectively [68].

From above literatures, the substitution of Nb and V on B-site was aimed to improve the properties of double perovskite $\text{Sr}_2\text{FeTiO}_{6-\delta}$ (SFT) material for IT-SOFC. Thus, the properties, such as electrical conductivity, catalytic activity for oxygen reduction and hydrogen oxidation, and cell performance were investigated.

1.7 Objectives

- 1.7.1 To synthesize and characterize $\text{Sr}_2\text{FeTi}_{1-x}\text{Nb}_x\text{O}_{6-\delta}$ and $\text{Sr}_2\text{FeTi}_{1-x}\text{V}_x\text{O}_{6-\delta}$ ($x = 0.05 - 0.50$) samples
- 1.7.2 To measure the properties of $\text{Sr}_2\text{FeTi}_{1-x}\text{Nb}_x\text{O}_{6-\delta}$ and $\text{Sr}_2\text{FeTi}_{1-x}\text{V}_x\text{O}_{6-\delta}$ ($x = 0.05 - 0.50$) samples including;
 - Electrical conductivity
 - Electrochemical performance



CHAPTER 2

EXPERIMENTAL

The chemicals, preparation of materials and characterization of samples are explained in this chapter.

2.1 Chemicals

Table 2.1 shows the chemicals and reagents listed, which were used without purification.

Table 2.1 The chemicals and reagents used in this research

Chemical and reagent	Formula weight	Purity (%)	CAS no.	Company
SrCO ₃	147.63	≥ 99.9	1633-05-2	Aldrich
Fe ₂ O ₃	159.69	81	1317-61-9	Labchem
NiO	74.69	99	1313-99-1	Aldrich
La ₂ O ₃	325.81	99.99	1312-81-8	Wako
Ga ₂ O ₃	187.44	≥ 99.99	12024-21-4	Aldrich
MgO	40.30	≥ 98.0	1309-48-4	Fluka
Sr(NO ₃) ₃	211.63	99	10042-76-9	Sigma-Aldrich
Sm(NO ₃) ₃ ·6H ₂ O	444.47	99.9	13759-83-6	Aldrich
Co(NO ₃) ₃ ·6H ₂ O	291.03	98 – 102.0	10026-22-9	Univar
C ₆ H ₈ O ₇ ·H ₂ O	210.14	99.5 – 100.5	77-92-9	Merck
NH ₄ NO ₃	80.04	101.0	6484-52-2	J.T. Baker
NH ₃ solution	35.50	25	7664-41-7	Merch
Fe(NO ₃) ₃ ·9H ₂ O	404.00	≥ 98	7782-61-8	Sigma-Aldrich
C ₂ H ₆ O	46.07	99	64-17-5	Merch
TiO ₂	79.87	99.8	1317-70-0	Aldrich
Nb ₂ O ₅	265.81	99.99	1313-96-8	Aldrich

Chemical and reagent	Formula weight	Purity (%)	CAS no.	Company
V ₂ O ₅	181.90	>98.5	1314-62-1	B. D. H.
C ₁₀ H ₁₆ N ₂ O ₈	292.25	99.4 – 100.6	60-00-4	Univar
C ₁₂ H ₂₄ O ₃	216.32	99	25265-77-4	Sigma-Aldrich
Ethyl cellulose	-	48.0 – 49.5 (%w/w)	9004-57-3	Fluka

2.2 Material preparation

2.2.1 Anode preparation

Anode, Nickel Iron Oxide (Ni-Fe), was prepared by modified impregnation method. Firstly, the mixture solution with weight percentage (%wt) ratio between Nickel and Iron of 9: 1 was prepared by dissolving Fe(NO₃)₃·9H₂O in distilled water under heating and stirring for 30 minutes. Then, NiO was dissolved in distilled water and added into the Fe-solution under vigorously stirring. The mixture solution was continuously stirred and heated until the color of solution changed to dark-brown color. After that, the temperature was increased to evaporate the solvent. Before the solvent disappeared, the magnetic stirrer was removed and the slurry was stirred using a glass stirring rod to obtain a dry product. The resulting product was then covered with a glass cover and heated at 200°C to release NO_x gases until the dark-brown product was achieved. The product was then transferred into a furnace and heat-treated again at 400°C for 2 hours. Finally, the obtained powder was calcined at 1,200°C for 6 hours and ground with ethanol.

2.2.2 Cathode preparation

Sr_{0.5}Sm_{0.5}CoO₆ (SSC), a cathode, was synthesized via the combination method using citrate and ethylenediamine tetra acetic acid (EDTA) complexing. Firstly, the stoichiometric amount of prepared solution was calculated based on the molar ratio of total metal ions: citric acid: EDTA was around 1: 3: 1.1. Then, the EDTA-NH₃-H₂O solution, a complexing agent, was prepared by dissolving EDTA in deionized water and

adding the 25%wt ammonia solution into until the pH of mixture was approximately 7 under stirring. Next, $\text{Sr}(\text{NO}_3)_2$, $\text{Sm}(\text{NO}_3)_3 \cdot 6\text{H}_2\text{O}$ and $\text{Co}(\text{NO}_3)_3 \cdot 6\text{H}_2\text{O}$ were dissolved in deionized water to obtain the dark reddish solution, which was slowly poured into the EDTA- $\text{NH}_3 \cdot \text{H}_2\text{O}$ solution under stirring. After that, the citrate solution of $\text{C}_6\text{H}_8\text{O}_7 \cdot \text{H}_2\text{O}$ was added into the solution. At this stage, the pH solution was seriously controlled to 7 by the addition of 25% NH_4NO_3 solution. Then, the mixture solution was left overnight at room temperature under stirring. The resulting solution was later evaporated on the hot plate until the product was obtained. Lastly, the black product was calcined at 400°C for 2 hours, sintered at $1,000^\circ\text{C}$ for 5 hours, and ground into powder.

2.2.3 Samples preparation

The sample materials prepared in this section were used as both anode and cathode. All samples were synthesized through a traditional solid-state reaction and the compositions and abbreviations of materials are summarized in the Table 2.2.

The stoichiometric amounts of starting materials, SrCO_3 , Fe_2O_3 , TiO_2 , Nb_2O_5 and V_2O_5 were thoroughly mixed by a mortar and pestle with ethanol for an hour and then calcined in air at $1,050^\circ\text{C}$ for 12 hours. The calcined powder was re-grounded with ethanol for 1 hour. After that the resulting powder was pressed into pellets and sintered in air at $1,250^\circ\text{C}$ for 12 hours to obtain a dense ceramic disk. The heating rate of both calcination and sinterization was $3.3^\circ\text{C} \cdot \text{min}^{-1}$.

Table 2.2 Compositions and abbreviations of prepare samples

Substituted site	Dopant	Composition	Abbreviation
-	-	$\text{Sr}_2\text{FeTiO}_6$	SFT
Ti	Nb	$\text{Sr}_2\text{FeTi}_{0.95}\text{Nb}_{0.05}\text{O}_6$	SFTNb05
		$\text{Sr}_2\text{FeTi}_{0.9}\text{Nb}_{0.1}\text{O}_6$	SFTNb1
		$\text{Sr}_2\text{FeTi}_{0.8}\text{Nb}_{0.2}\text{O}_6$	SFTNb2
		$\text{Sr}_2\text{FeTi}_{0.7}\text{Nb}_{0.3}\text{O}_6$	SFTNb3
		$\text{Sr}_2\text{FeTi}_{0.6}\text{Nb}_{0.4}\text{O}_6$	SFTNb4
		$\text{Sr}_2\text{FeTi}_{0.5}\text{Nb}_{0.5}\text{O}_6$	SFTNb5
	V	$\text{Sr}_2\text{FeTi}_{0.95}\text{V}_{0.05}\text{O}_6$	SFTV05
		$\text{Sr}_2\text{FeTi}_{0.9}\text{V}_{0.1}\text{O}_6$	SFTV1
		$\text{Sr}_2\text{FeTi}_{0.8}\text{V}_{0.2}\text{O}_6$	SFTV2
		$\text{Sr}_2\text{FeTi}_{0.7}\text{V}_{0.3}\text{O}_6$	SFTV3
		$\text{Sr}_2\text{FeTi}_{0.6}\text{V}_{0.4}\text{O}_6$	SFTV4
		$\text{Sr}_2\text{FeTi}_{0.5}\text{V}_{0.5}\text{O}_6$	SFTV5

2.2.4 Electrolyte preparation

In this research, $\text{La}_{0.9}\text{Sr}_{0.1}\text{Ga}_{0.8}\text{Mg}_{0.2}\text{O}_3$ (LSGM) was chosen as the electrolyte because it has high ionic conductivity. LSGM was synthesized by a conventional solid-state reaction. Firstly, the stoichiometric mixture of La_2O_3 , SrCO_3 , Ga_2O_3 and MgO were grounded in a mortar homogeneously for an hour and then calcined at $1,000^\circ\text{C}$ in air. Later, the calcined powder was re-grounded for 1 hour and pressed into cylindrical disks (2 cm. in a diameter) via a cold isostatic pressing (CIP) method at 325 MPa for 30 minutes. Next, the white disks were sintered in air at $1,500^\circ\text{C}$ for 5 hours after that the disks were polished to reduce the thickness to 0.3 mm. by a diamond grinding machine.

2.2.5 Compatibility test

The chemical compatibility between electrode and electrolyte was prepared using a mixture of sample and LSGM electrolyte in 1: 1%wt ratio with grounded and

then calcined at 900°C for 5 hours in air. The calcined powder was analyzed by the X-ray diffraction technique.

2.3 Material characterization

2.3.1 X-ray diffractometry (XRD)

The crystal structure of synthesized materials was carried out using a Rigaku, DMAX 2002 Ultima Plus X-ray powder diffractometer equipped with a monochromator and the Cu X-ray tube (40 kV, 30 mA). The data were recorded on the two-theta range of 20 – 80 degree with a scan speed of 5 degree·min⁻¹ in air at Department of Chemistry, Faculty of Science, Chulalongkorn University.

2.3.2 Electrical conductivity Measurement

Electrical conductivity of the specimens was measured by the DC four-point probes method. The sintered-pellet sample were cut into a rectangular shape with dimension of 12 mm. x 5 mm. x 1.5 mm. and then two platinum wires, the current electrode, were attached to the outer of the rectangular specimen using the platinum paste binder. Also, another two wires which corresponds to the voltage probes were placed between the outer probes as shown in Figure 2.1 and the distance of inner platinum wires is approximately. 5 mm. The specimen was heated at 950°C with a heating rate of 5°C·min⁻¹ for 10 minutes in order to assure a good contact between wires and specimen. When the DC current (I) was applied through the current probe, the difference in voltage between the inner platinum probes was recorded from 300°C to 800°C in air with 50°C increments using an Autolab PGSTAT302N potentiostat/galvanostat. In addition, the data were calculated using the equation 2.1.

$$\sigma = \frac{I}{V} \times \frac{L}{W \times T} \quad \text{----- (2.1)}$$

Where; σ is the electrical conductivity (S·cm⁻¹)

I is the applied DC current (A)

L is the distance between the two inner probes (cm)

V is the voltage difference between the two outer probes (V)

W is the width of the specimen (cm)

T is the thickness of the specimen (cm)

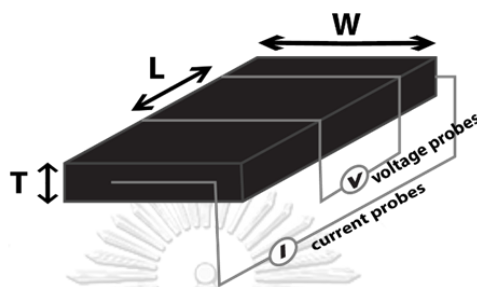


Figure 2.1 DC four point probe measurement

2.3.3 Thermal expansion coefficient (TEC)

Coefficient of thermal expansion of materials was carried out using a Dilatometer series NETZSCH DIL 402SE and a type of measurement was standard expansion/sample with correction. The data was recorded with the temperature range between 25°C and 1000°C and a scan speed of 5°C·min⁻¹.

2.3.4 Electrochemical Impedance Spectroscopy

Symmetric cells were fabricated using 0.3 mm.-thick LSGM as the electrolyte and the synthesized oxides as the electrodes. The oxide samples were prepared into slurries using a mixture of isobutyrate and ethyl cellulose as a binder. Then, the sample slurry was subsequently applied on both sides of LSGM disk via a screen-printing technique to produce a symmetric cell. Next, the screened disk was heated at 900°C for 30 minutes in air for the complete adhesion between electrolytes and electrodes. After that, the cell was placed on between the alumina tubes without a sealing glass O-ring and exposed to air at operating temperature from 600 – 800°C under ambient pressure. The overall instrumentation is shown in Figure 2.2. Moreover, the AC impedance measurement was recorded on the potentio-stat mode of an Autolab

PGSTAT302N instrument with the frequency response analyser under open circuit conditions and the frequency range is 1 MHz to 0.01 Hz.

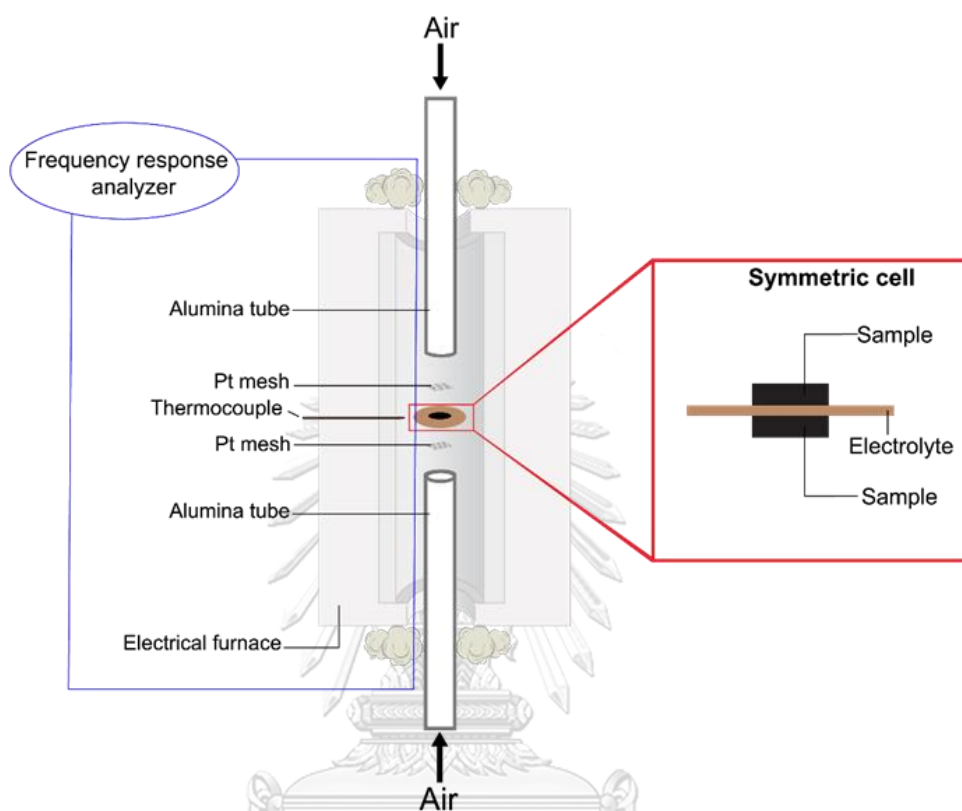


Figure 2.2 Schematic diagram of symmetric cell for AC impedance measurement

2.3.5 SOFC performance

Like a symmetric cell, a single cell was prepared by the screen printing method of oxide materials on the electrolyte (LSGM) but the applied electrode side was cathode slurry while the other side was anode. Additionally, the anode side was exposed to hydrogen gas (99.99%) whereas the cathode side was fed by oxygen gas (99.99%) with the flow rate of $100 \text{ mL}\cdot\text{min}^{-1}$ at the operating temperature from $600 - 800^\circ\text{C}$ and the cell was sealed by the glass O-ring as shown in Figure 2.3. The voltage (V) and current (I) of single cell were carried out using the U3402A Agilent multimeter and the HA - 151B galvanostat, respectively.

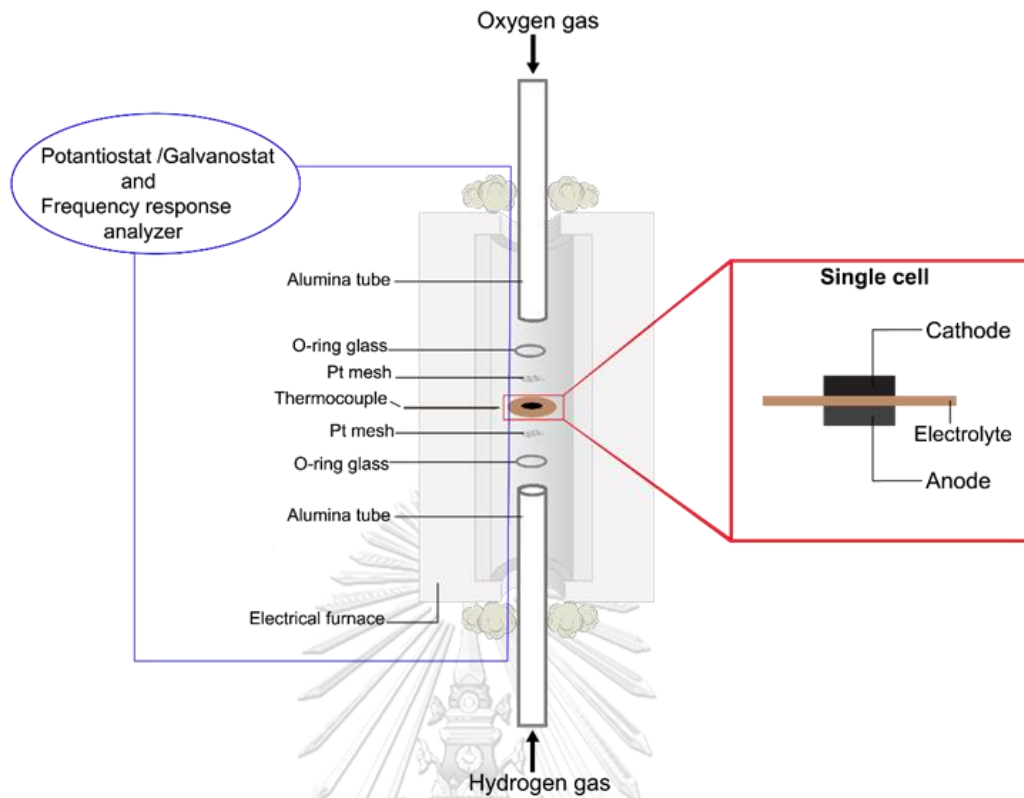


Figure 2.3 Schematic of the single cell measurement for AC impedance and SOFC performance

CHAPTER 3

RESULT AND DISCUSSION

3.1 XRD characterizations

The XRD patterns of SFT and doped oxides sintered at 1250°C for 12 hours in air are shown in Figure 3.1 and Figure 3.2. The XRD spectrum indicates that SFT is pure and has double perovskite structure (JCPDF 84 – 1004), similar to the work report by Q. Zhou [63]. The XRD patterns of $\text{Sr}_2\text{FeTi}_{1-x}\text{Nb}_x\text{O}_{6-\delta}$ ($x = 0.05 - 0.5$) show a double perovskite structure of SFT and the formation of $\text{Sr}(\text{FeNb})_{0.5}\text{O}_3$ impurity phase (JCPDF 75 – 0003) [69], except in $\text{Sr}_2\text{FeTi}_{0.95}\text{Nb}_{0.05}\text{O}_{6-\delta}$ which is a pure phase of SFT. The intensity of impurity phase increases with the increasing of Nb content. Likewise, the XRD patterns of $\text{Sr}_2\text{FeTi}_{1-x}\text{V}_x\text{O}_{6-\delta}$ ($x = 0.05 - 0.5$) shown in Figure 3.2 denote the double perovskite structure as well. The concentration of $\text{Sr}_3(\text{VO}_4)_2$ (JCPDF 29 – 1318) [70, 71] impurity phase also increases with V content similar to the Nb doped SFT.

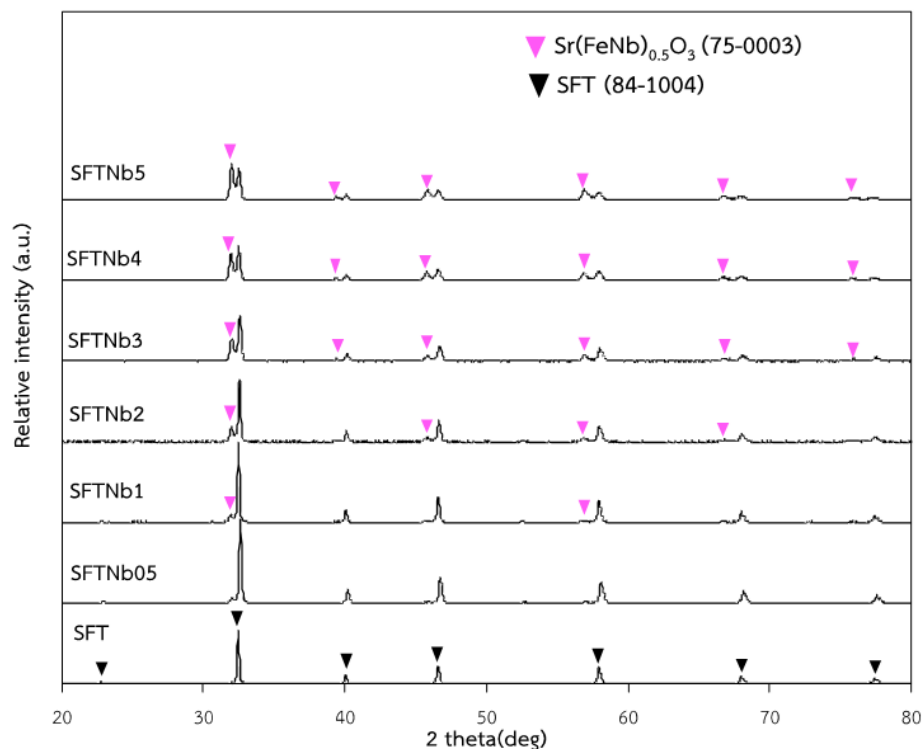


Figure 3.1 XRD patterns of SFT and $\text{Sr}_2\text{FeTi}_{1-x}\text{Nb}_x\text{O}_{6-\delta}$ ($x = 0.05 - 0.50$) at room temperature

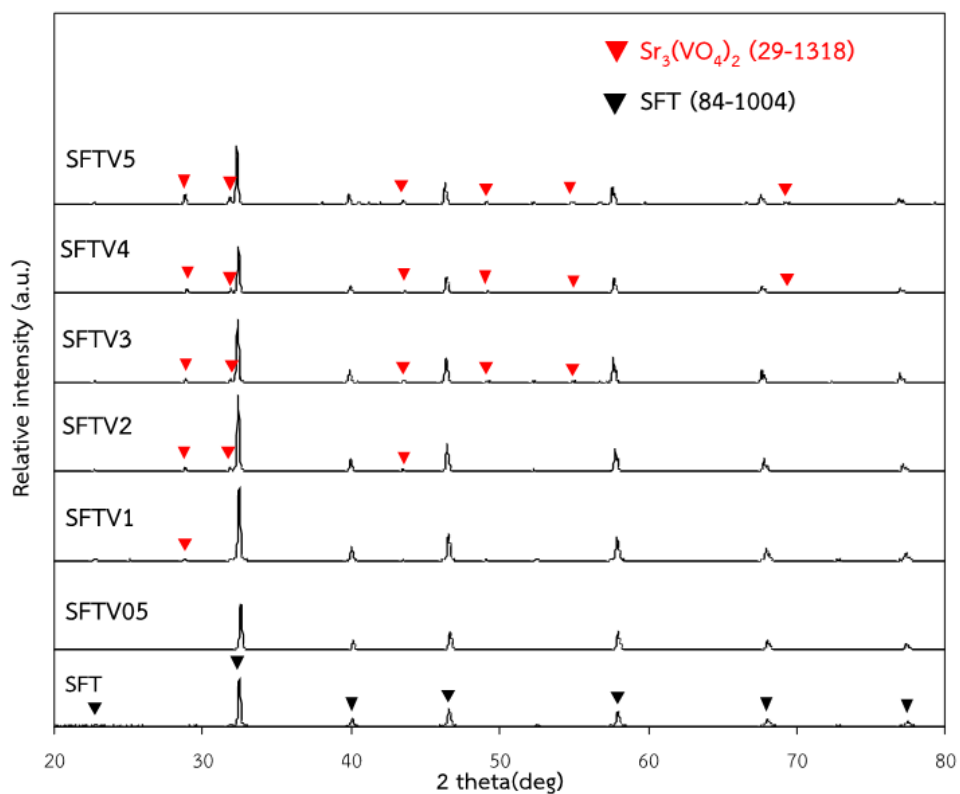


Figure 3.2 XRD patterns of SFT and $\text{Sr}_2\text{FeTi}_{1-x}\text{V}_x\text{O}_{6-\delta}$ ($x = 0.05 - 0.50$) at room temperature

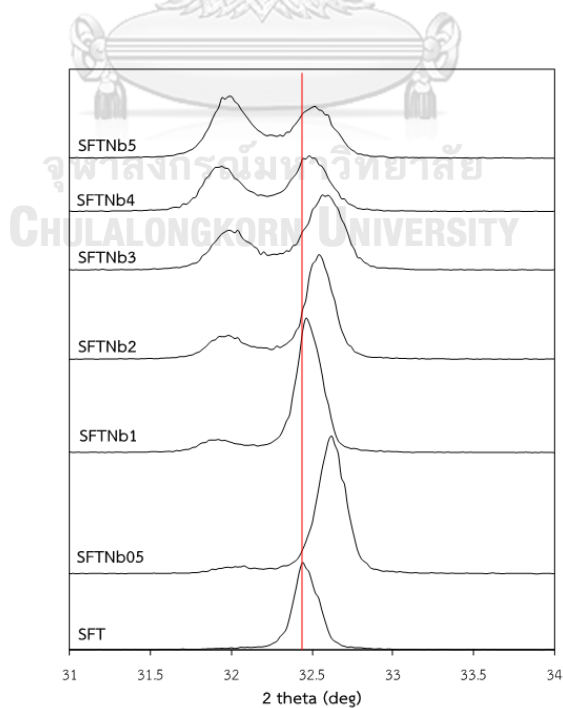
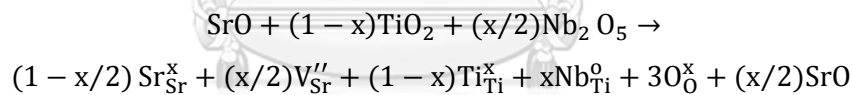


Figure 3.3 The magnification of main peak in XRD patterns of SFT and $\text{Sr}_2\text{FeTi}_{1-x}\text{Nb}_x\text{O}_{6-\delta}$ ($x = 0.05 - 0.50$)

Figure 3.3 presents the magnification of XRD pattern for SFT and $\text{Sr}_2\text{FeTi}_{1-x}\text{Nb}_x\text{O}_{6-\delta}$ ($x = 0.05 - 0.50$) at 2Theta between 31 to 34 angles. When Nb^{5+} ions substituted for Ti^{4+} ions in double perovskite structure, the diffraction peak at 2Theta about 32.4 angle was shifted to the high angle, suggesting the contraction of the unit cell lattice, as related to the bragg's equation. Even though the pentavalent of niobium ions has larger ionic radii than the tetravalent of titanium ions ($\text{Nb}^{5+} = 0.64 \text{ \AA}$, $\text{Ti}^{4+} = 0.605 \text{ \AA}$), the expansion of unit cell to the low value of 2Theta angle was not clearly observed below 32.4 angle because it might be related with Fe ions in double perovskite and strontium vacancies. When 0.05 mole of Nb^{5+} was added for Ti^{4+} ions, the ratio of $\text{Fe}^{4+}/\text{Fe}^{3+}$ increased as seen from XPS result. As a result, Fe^{4+} ions which have smaller ionic radii than Fe^{3+} ions, cause the shrinkage in lattice structure. As Niobium ions increased, the expansion of lattice was observed compared to 0.05 mole of Nb^{5+} but it is also insignificant compared to SFT. Additionally, the substitution of titanium with niobium can create the strontium vacancies and SrO phase, as shown in the following equation written according to the kröger-Vink notation. If the preferred species is strontium vacancies, the incorporation reaction would be as followed [72]:



The appearance of SrO caused the lattice structure decreased similar to the works found in $\text{SrTi}_{1-x}\text{Nb}_x\text{O}_{3-\delta}$ ($0 < x < 0.08$) perovskite [73] and $\text{Sr}_{0.99}\text{Ti}_{1-x}\text{Nb}_x\text{O}_3$ [72]. When the Nb content in SFT oxides was increased ($\text{Nb} > 0.05$), the main diffraction peak shifted to the low angle of 2Theta compared to SFTNb05, suggesting a slightly expansion of the unit cell. This could be a result of the Nb^{5+} content added and the large ionic radii of Nb^{5+} ions. However, please note that there was a difficult in determining the unit cell of SFT at high Nb content because the amount of secondary phase, $\text{Sr}(\text{FeNb})_{0.5}\text{O}_3$, increased might alter the main diffraction peak of SFT, as reported by T. Tahsin Khan [71] The impurity phase influenced the crystallite size of the materials which could be easily seen by the lower intensity and the expandable peak width of main peak in the XRD pattern.

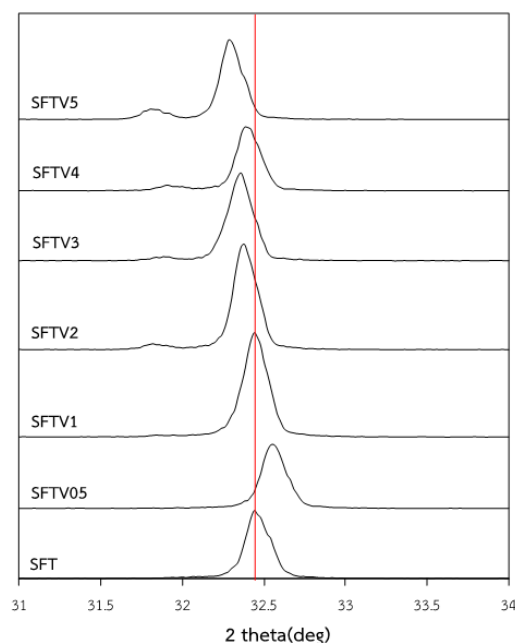


Figure 3.4 The magnification of main peak in XRD patterns of SFT and $\text{Sr}_2\text{FeTi}_{1-x}\text{V}_x\text{O}_{6-\delta}$ ($x = 0.05 - 0.50$)

Figure 3.4 shows the magnification of XRD pattern for SFT and $\text{Sr}_2\text{FeTi}_{1-x}\text{V}_x\text{O}_{6-\delta}$ ($x = 0.05 - 0.50$) at 2Theta between 31 to 34 angles. When vanadium was doped in SFT oxides, the diffraction peak intentionally shifted to the low values of 2Theta, except for the composition of $\text{Sr}_2\text{FeTi}_{0.95}\text{V}_{0.05}\text{O}_{6-\delta}$. Because the pentavalent of vanadium has smaller ionic radii ($\text{V}^{5+} = 0.54 \text{ \AA}$), substitution of vanadium for the tetravalent of titanium in double perovskite caused the shrinkage of lattice parameter, as a result the main diffraction of SFT shifted to the high 2Theta values as observed in $\text{Sr}_2\text{FeTi}_{0.95}\text{V}_{0.05}\text{O}_{6-\delta}$. On the other hand, increasing the amount of V might affect the electron neutrality and the change in spin state of iron [74, 75], which could expand the lattice parameter and result in the shift of the SFT peak to the low angle of 2Theta.

3.2 Electrical conductivity measurement

The temperature dependence on electrical conductivity of SFT in air is illustrated in Figure 3.5(a). The electrical conductivity increases with increasing temperature from 300 – 600°C, suggesting a semiconducting behavior and a typical

metallic behavior above 600°C. The maximum electrical conductivity of SFT is approximately 2.00 S·cm⁻¹ at 600°C, which is lower than that of SFT reported by W. Li et al, around 2.83 – 2.33 S·cm⁻¹ [62]. The activation energy for electrical conduction was derived from a slope of the linear fits in the relationship between ln(σT) and 1000/T using equation 3.1, and the Arrhenius plot of conductivity for SFT is displayed in Figure 3.5(b). It is clearly seen that there are two linear fits which the calculated activation energy values are 0.4187 eV (300 – 600°C) and 0.0196 eV (600 – 800°C), respectively, indicating the difference in mechanisms between low and high temperatures. At temperatures below 600°C, the conductivity is dominated by small polaron hopping mechanism [76, 77] and the electrons transfer in double perovskite through the B-O-B bonds [78]. As the rise of temperature, the loss of oxygen in the lattice increases and produces oxygen vacancy, which leads to the ionic conductivity. As a result, the activation energy for ionic conduction is less than that at low temperature. In addition, the oxygen loss in lattice can also break the B-O-B interaction. Therefore, the mobility of electron carriers is decreased as well as the electronic conductivity is also reduced [79]. However, in mixed ionic/electronic conductors (MIECs) such as double perovskites, the electrical conductivity is dominated by the electronic conductivity due to the mobility of electron is much higher than the oxygen ions [80, 81]. Thus, the total conductivity decreases with increasing the temperature.

$$\sigma = \frac{A}{T} \exp\left(\frac{-E_a}{kT}\right) \quad (3.1)$$

Where σ is conductivity, A is the pre-exponential factor, T is a temperature (K), k is the Boltzmann constant (8.6173×10^{-5} eV·K⁻¹), and E_a is the activation energy for conduction.

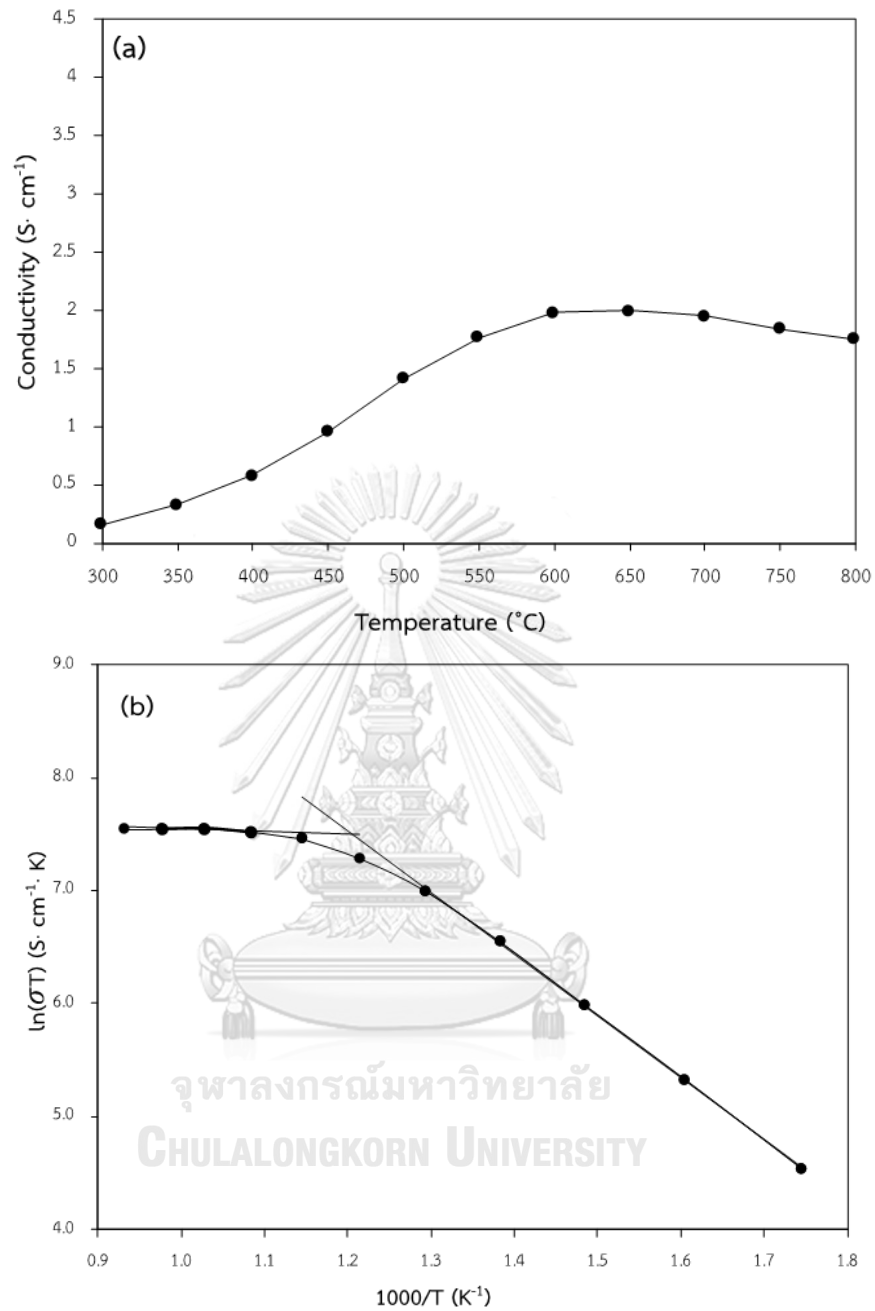


Figure 3.5 Temperature dependence on electrical conductivity for SFT in air (a) and Arrhenius plots of the electrical conductivity for SFT (b)

Table 3.1 The maximum electrical conductivity (σ_{max}) of SFT, $Sr_2FeTi_{1-x}Nb_xO_{6-\delta}$ and $Sr_2FeTi_{1-x}V_xO_{6-\delta}$ ($x = 0.05 - 0.5$)

Composition (x)	σ_{max} (S·cm ⁻¹)	
	$Sr_2FeTi_{1-x}Nb_xO_{6-\delta}$	$Sr_2FeTi_{1-x}V_xO_{6-\delta}$
0.00	2.00	2.00
0.05	2.44	3.93
0.10	2.08	2.89
0.20	1.62	3.22
0.30	0.82	2.83
0.40	0.63	3.30
0.50	0.38	2.84

Figure 3.6 shows a similar trend of temperature dependence on electrical conductivity of $Sr_2FeTi_{1-x}Nb_xO_{6-\delta}$ ($x = 0.05 - 0.5$) which the semiconducting behavior is observed. The electrical conductivities of Nb-doped SFT are similar to the SFT indicating the conductivity mechanisms are the same. The overall electrical conductivities of Nb doped SFT decrease obviously with the increasing of Nb content as well as the maximum electrical conductivity of $Sr_2FeTi_{1-x}Nb_xO_{6-\delta}$ ($x = 0.05 - 0.5$) are shown in Table 3.1. The activation energies of Nb-doped SFT double perovskites were derived from the Arrhenius plots of $\ln(\sigma T)$ versus $1000/T$ in Figure 3.7 and be listed in Table 3.2. It can be seen that the increased E_a value with increasing amount of Nb exhibit the decreasing of electronic conductivity. This is probably related to the impurity phase, $Sr(FeNb)_{0.5}O_3$, which is a dielectric material [82]. This secondary phase may reduce the effective contact area in SFTNb double perovskites and provide a defiant influence on the B-O-B networks of Nb-doped SFT lattices, as a result, the electrical conductivity is reduced when the impurity increases in the Nb-doped oxides. These results are in agreement with the work reported by L. Zhang et al. [83]. Additionally, similar trend was also observed on the work reported by G. Xiao et al., who investigated Mo-doped $SrFeO_{3-\delta}$ as cathode material. They mentioned that the conductivity of materials was decreased with increasing Mo content due to the

decreased number of charge carrier or Fe ions [84]. However, the increase of the Fe^{4+} charge improved the electrical property as well [85]. L. dos Santo-Gómez et al. also reveals that relationship between the structural parameter and the conductivity of Zr-doped $\text{SrFeO}_{3-\delta}$ for SOFCs. The structural parameters were expanded as the Zr dopant increased and the electrical conductivity of Zr-doped SFO was reduced. In addition, it was also related to the low concentration of Fe ions charge carriers [86]. Besides, N. Dai et al. discovered the decreasing of unit cell parameters when Ni substituted for Fe in perovskites, $\text{Sr}_2\text{Fe}_{1.5-x}\text{NiMo}_{0.5}\text{O}_{6-\delta}$ ($x = 0 - 0.1$), increased conductivity, compared to the SFM perovskite [87]. Therefore, in this study, with a small amount of Nb dopant, $\text{Sr}_2\text{FeTi}_{0.95}\text{Nb}_{0.05}\text{O}_{6-\delta}$ has higher electrical conductivity value than SFT double perovskite, and the maximum conductivity was achieved approximately $2.44 \text{ S}\cdot\text{cm}^{-1}$ at 700°C . It may relate to the high $\text{Fe}^{4+}/\text{Fe}^{3+}$ ratio in SFTNb05 oxide (see in section 3.5) and the shrinkage of the lattice, as observed from the XRD result, resulting the overlapping between the orbitals of B and O^{2-} becomes closer and electrons easily delocalize via B-O-B interaction, then the electronic conductivity is increased.

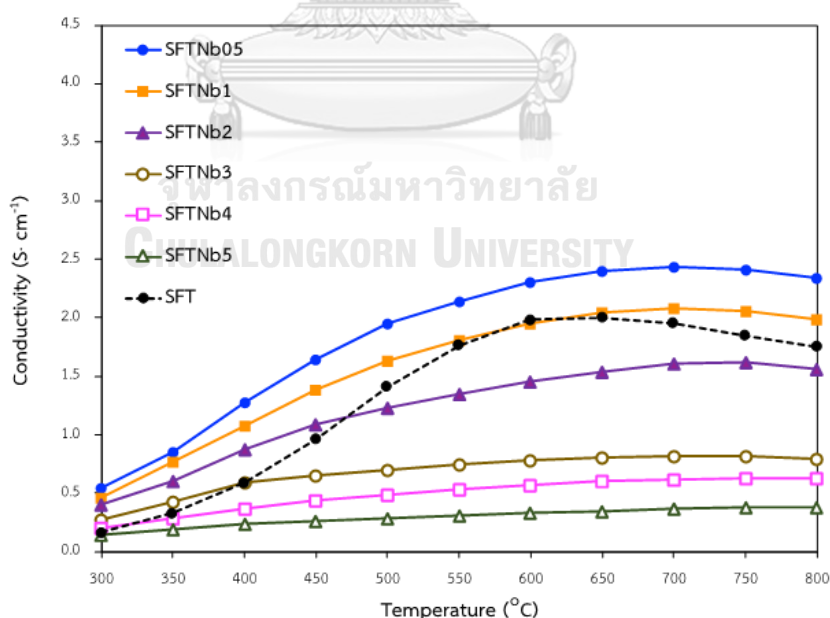


Figure 3.6 Electrical conductivity of $\text{Sr}_2\text{FeTi}_{1-x}\text{Nb}_x\text{O}_{6-\delta}$ ($x = 0.05 - 0.50$) with SFT in air as a function of temperature

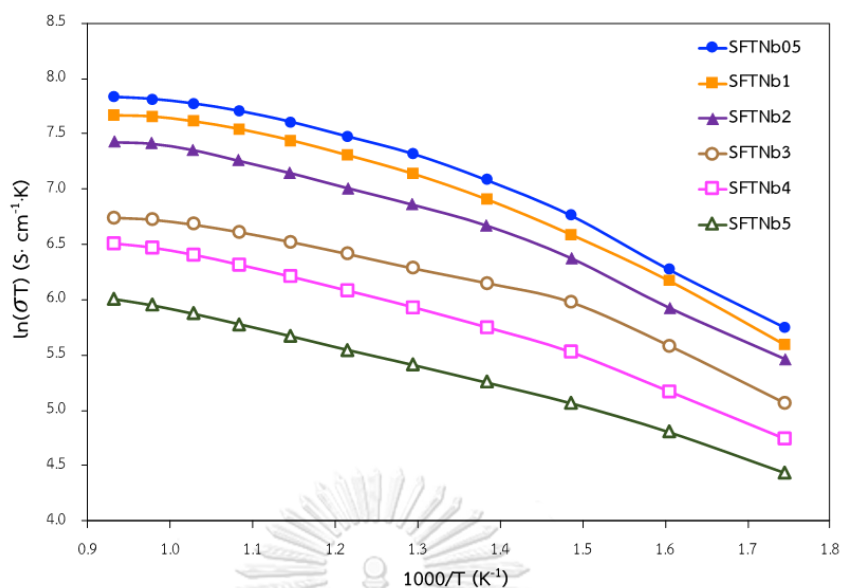


Figure 3.7 Arrhenius plot of $Sr_2FeTi_{1-x}Nb_xO_{6-\delta}$ ($x = 0.05 - 0.50$) for the electrical conductivity

Table 3.2 Activation energy of conductivity for $Sr_2FeTi_{1-x}Nb_xO_{6-\delta}$ ($x = 0.05 - 0.50$)

Oxides	Activation energy, E_a (eV)
SFTNb05	0.1592
SFTNb1	0.1661
SFTNb2	0.1684
SFTNb3	0.1692
SFTNb4	0.1723
SFTNb5	0.1736

The variation of electrical conductivity of $Sr_2FeTi_{1-x}V_xO_{6-\delta}$ ($x = 0.05 - 0.5$) samples with temperature in air and the Arrhenius plot of $Sr_2FeTi_{1-x}V_xO_{6-\delta}$ ($x = 0.05 - 0.5$) for the electrical conductivity are shown in Figure 3.8 and Fig 3.9, respectively. And, the summarization of activation energy is displayed in Table 3.3. Compared to SFT, the electrical conductivities of V-doped SFT increase with small amount of V added to $x=0.05$ which corresponds to the decreasing of activation energy. With increasing of V content from 0.05-2.0, the electrical conductivity decreases. The highest electrical conductivity was observed on $Sr_2FeTi_{0.95}V_{0.05}O_{6-\delta}$, which is $\sim 3.39 \text{ S}\cdot\text{cm}^{-1}$ at

700°C. This composition was similar to the Nb-doped SFT series which the highest electrical conductivity was observed on $\text{Sr}_2\text{FeTi}_{0.95}\text{Nb}_{0.05}\text{O}_{6-\delta}$. The high electrical conductivity of $x = 0.05$ in V-doped oxide may result from the shrinkage in structure which provides a good B-O-B interaction. For high V content ($x > 0.05$), impurity may play a role for the decreasing of conductivity. Since the impurity, $\text{Sr}_3(\text{VO}_4)_2$, has dielectric property [70] with high dielectric constant at 400°C thus the resistivity of materials would be increased. As a result, the conductivity decreased with increasing impurity. On the contrary, at high temperature, the dielectric constant of impurity was low thus the conductivity increased with increasing amount of impurity.

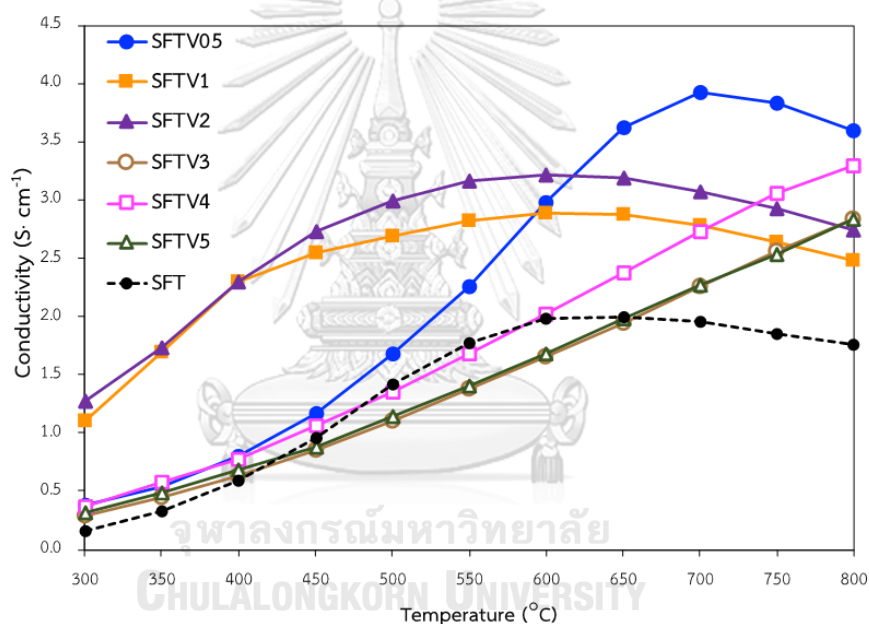


Figure 3.8 Electrical conductivity of $\text{Sr}_2\text{FeTi}_{1-x}\text{V}_x\text{O}_{6-\delta}$ ($x = 0.05 - 0.50$) with SFT in air as a function of temperature

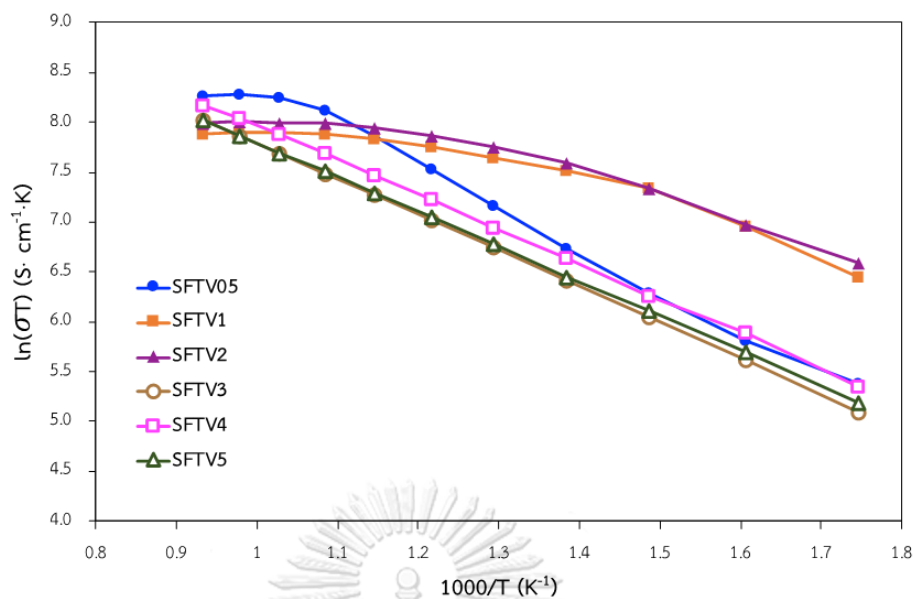


Figure 3.9 Arrhenius plot of $Sr_2FeTi_{1-x}V_xO_{6-\delta}$ ($x = 0.05 - 0.50$) for the electrical conductivity

Table 3.3 Activation energy of conductivity for $Sr_2FeTi_{1-x}V_xO_{6-\delta}$ ($x = 0.05 - 0.50$)

Oxides	Activation energy, E_a (eV)
SFTV05	0.3044
SFTV1	0.2371
SFTV2	0.2324
SFTV3	0.3132
SFTV4	0.3016
SFTV5	0.3033

3.3 Electrochemical Impedance Spectroscopy (EIS)

Figure 3.10(a) shows the typical EIS spectra of $\text{Sr}_2\text{FeTi}_{1-x}\text{Nb}_x\text{O}_{6-\delta}$ ($x = 0.05 - 0.50$) symmetrical cell with LSGM electrolyte at 800°C and the ohmic resistance was set at zero in the Nyquist plot. The polarization resistance value of all Nb substitution in SFT material was also presented in Table 3.4. It can be clearly seen that the polarization resistance value of Nb-doped SFT oxides increases with the increasing amount of Nb. This result also corresponds to the conductivity of Nb-doped SFT (see in 3.2), which the resistance is inverse of conductivity. The decrease in conductivity and the increasing of resistance caused by the increasing of Nb content can be explained by the migration of electrons and oxide ions. Since two semicircles were clearly observed, increasing Nb content limits the charge transfer reaction at the interface and retards the ORR reaction. As the low frequency arc was larger than the high frequency one, it is suggested that the adsorption of oxygen molecule on the surface, the dissociation and diffusion of oxide ion in electrode materials are slow. Thus, the rate determining step of ORR is controlled by the adsorption, dissociation, and diffusion of oxygen molecule into oxide ions [66, 88, 89]. However, the polarization resistance value of $\text{Sr}_2\text{FeTi}_{0.95}\text{Nb}_{0.05}\text{O}_{6-\delta}$ was very low compared to others and the impedance plot at high and low frequency is not clearly distinct as two semicircles, suggesting high rate of ORR. Similar to the Nb substitution in SFT, small amount of V substitution promotes the ORR reaction by facilitating charge transfer of electrons, adsorption of oxygen molecules on the surface, dissociation and diffusion of oxide ions in cathode. And, the polarization resistance value of V substitution in SFT increases as the V content increases, suggesting the slow mechanism of oxygen molecule adsorption, dissociation and diffusion of oxide ions. The Nyquist plots of $\text{Sr}_2\text{FeTi}_{1-x}\text{V}_x\text{O}_{6-\delta}$ symmetrical cell with LSGM electrolyte at 800°C in air was displayed in Figure 3.10(b) and the polarization resistance values were shown in Table 3.4.

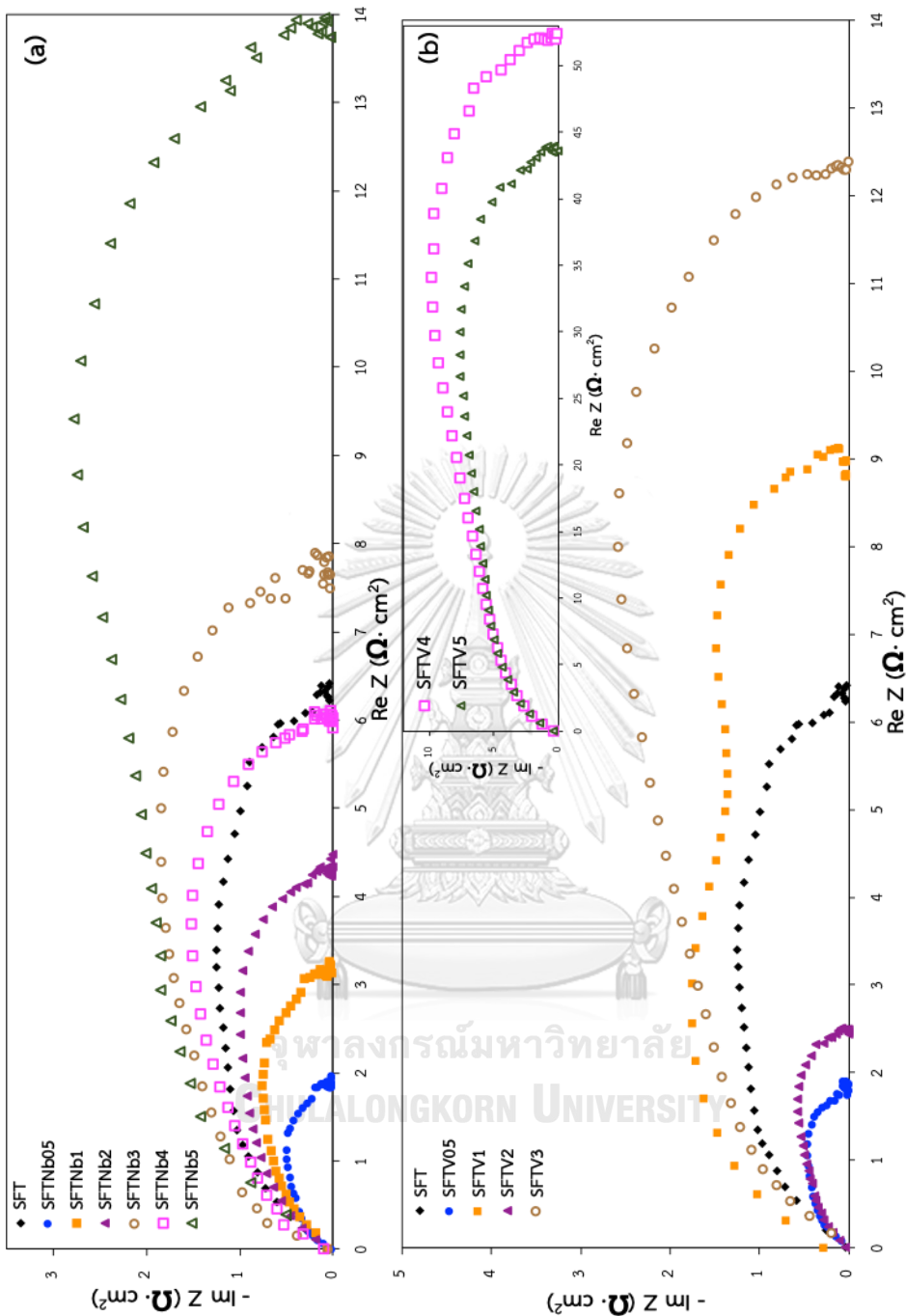


Figure 3.10 Typical impedance spectra of SFT, $Sr_2FeTi_{1-x}Nb_xO_{6-\delta}$ ($x = 0.00 - 0.50$) (a) and $Sr_2FeTi_{1-x}V_xO_{6-\delta}$ ($x = 0.00 - 0.50$) (b) with LSGM electrolyte at 800 °C in air

Table 3.4 The polarization resistance value of $Sr_2FeTi_{1-x}Nb_xO_{6-\delta}$ and $Sr_2FeTi_{1-x}V_xO_{6-\delta}$ ($x = 0 - 0.5$) at $800^\circ C$ in air

Composition (x)	Polarization resistance, R_p ($\Omega \cdot cm^2$)	
	$Sr_2FeTi_{1-x}Nb_xO_{6-\delta}$	$Sr_2FeTi_{1-x}V_xO_{6-\delta}$
0.00	6.42	6.42
0.05	1.91	1.89
0.10	3.14	8.97
0.20	4.48	2.46
0.30	7.56	12.74
0.40	6.63	52.37
0.50	13.79	43.57

3.4 Fuel cell performance

The single cell performance testing of the materials was performed on the LSGM-electrolyte supported cell under H_2 gas as a fuel and air as an oxidant. The asymmetrical cell and symmetrical cell test were divided into three parts;

- part I asymmetrical cell (cathode): the synthesized oxides were used as the cathode and NiFe as the anode.
- part II asymmetrical cell (anode): the materials were used as the anode and SSC as the cathode.
- Part III symmetrical cell: the perovskite samples were used as both the cathode and the anode.

3.4.1 Testing of single cell performance using $Sr_2FeTi_{1-x}M_xO_{6-\delta}$ ($M = Nb, V$) oxides as the cathode material

Figure 3.11 shows the cell voltage and the power density of SFTNb/ LSGM/ NiFe cells at $800^\circ C$ as a function of the current density. It can be seen that adding Nb improves power density of cell and the cell performance of SFTNb05 exhibits the highest maximum power density around $97 \text{ mW} \cdot \text{cm}^{-2}$, compared to the others. Subsequently, the power density of SFTNb ($x = 0.1, 0.2, 0.5$) are 54, 45, 40 $\text{mW} \cdot \text{cm}^{-2}$,

respectively. The single cell performance of SFTNb x increases with $x = 0.05$ and decreases when $x > 0.05$, that is also in accordance with the decreasing of electrical conductivity and the increasing of polarization resistance for the reaction of cathode. The typical Nyquist plot of SFTNb x / LSGM/ NiFe cells at 800°C is presented in Figure 3.12. The polarization resistance values of single cells are 1.15, 1.25, 1.76 and 1.89 $\Omega\cdot\text{cm}^2$ for SFTNb05, SFTNb1, SFTNb2 and SFTNb5, respectively. It can be observed that the polarization resistance of cell decreases when Nb was doped in the materials. Thus, the increasing of power density of materials is due to the reducing in polarization resistance. In addition, the increasing amount of niobium makes the polarization resistance increased and the cell performance decreased. The summary of polarization resistance value and the power density value of Nb-doped SFT samples is shown in Table 3.5.

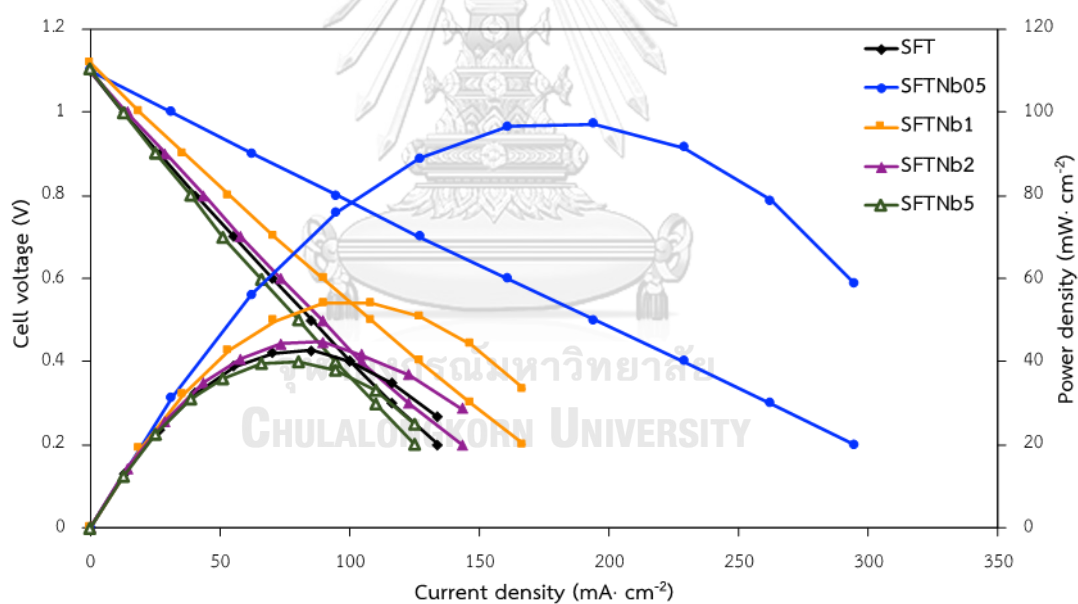


Figure 3.11 Cell voltage and power density as functions of current density for the single cell with $\text{Sr}_2\text{FeTi}_{1-x}\text{Nb}_x\text{O}_{6-\delta}$ ($x = 0.00, 0.05, 0.10, 0.20, 0.50$) cathode at 800°C

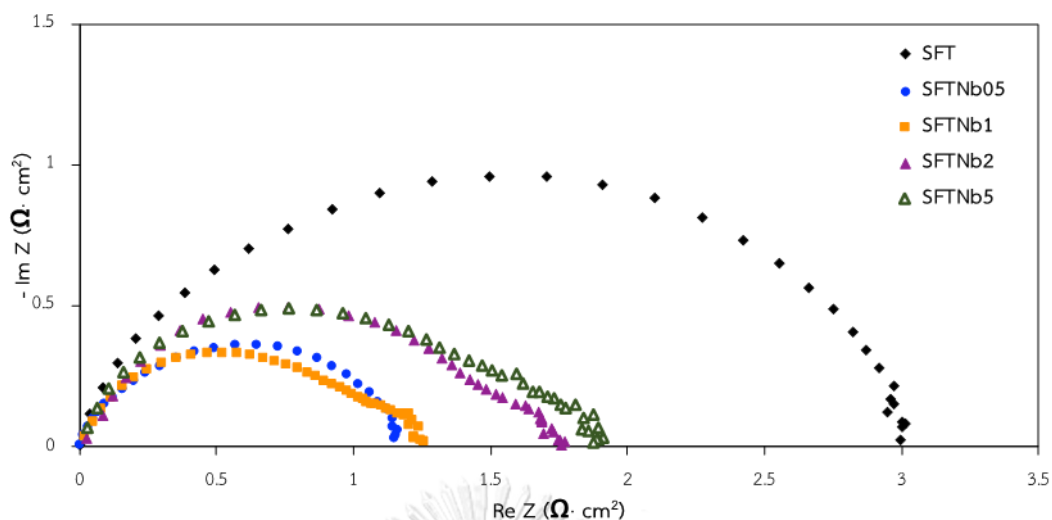


Figure 3.12 Impedance spectra of single cell with $Sr_2FeTi_{1-x}Nb_xO_{6-\delta}$ ($x = 0.00, 0.05, 0.10, 0.20, 0.50$) cathode at $800^\circ C$

Table 3.5 The maximum power density value and polarization resistance of a SFTNb x /LSGM/NiFe cell with different compositions at $800^\circ C$

	Maximum power density (mW·cm ⁻²)	R _p (Ω·cm ²)
SFT	43	2.99
SFTNb05	97	1.15
SFTNb1	54	1.25
SFTNb2	45	1.76
SFTNb5	40	1.89

Figure 3.13 shows the cell voltage and power density as a function of current density for the single cell with $Sr_2FeTi_{0.95}Nb_{0.05}O_{6-\delta}$ cathode in the temperature range of $600 - 800^\circ C$ with intervals of $50^\circ C$. The maximum power density of $Sr_2FeTi_{0.95}Nb_{0.05}O_{6-\delta}$ cathode are 97, 68, 48, 37 and 28 mW·cm⁻² at 800, 750, 700, 650 and $600^\circ C$, respectively. It can also be observed that the power density decreased with decreasing temperature because of the lower ORR rate. At low temperature, the migration of oxide ions in the materials is very difficult compared to the high

temperature, thus the reaction rate would be low and the power density of cell decreased.

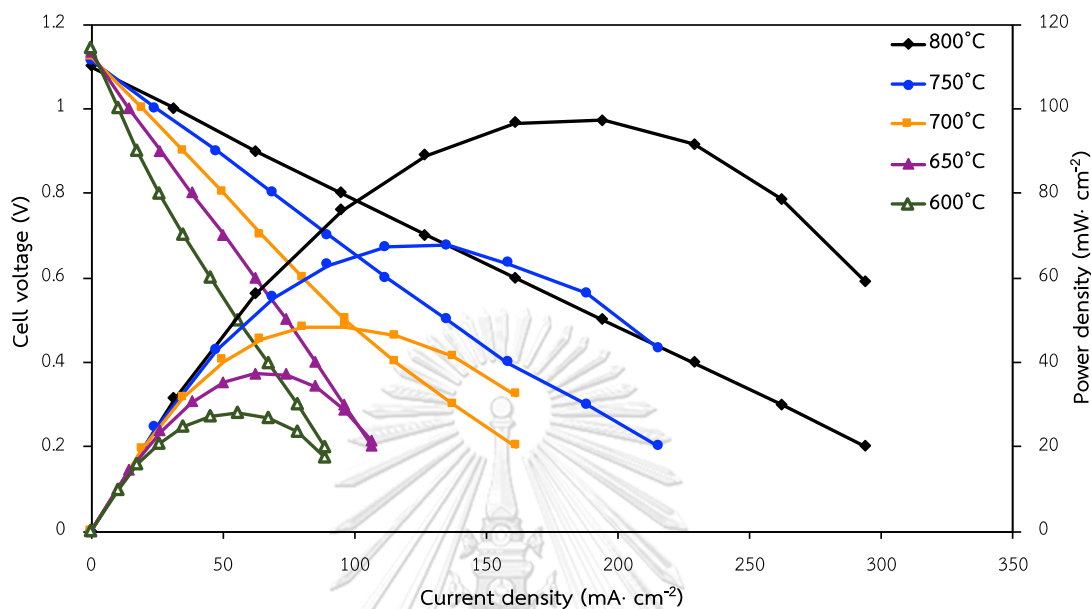


Figure 3.13 Cell voltage and power density as functions of current density for the single cell with $Sr_2FeTi_{0.95}Nb_{0.05}O_{6-\delta}$ cathode over the temperature range from 600 – 800°C

Figure 3.14 demonstrates the cell voltage and the cell performance of V-doped SFT cathodes with LSGM electrolyte operating at 800°C under humidified pure hydrogen as the fuel and ambient air as the oxidant. The maximum power density values are 106, 87, 78 and 17 mW·cm⁻² for SFTV05, SFTV1, SFTV2 and SFTV5, respectively. With small amount of V doped (x = 0.05, 0.1), the cell performance was improved and the best cell performance was achieved from SFTV05 because SFTV05 has the highest electrical conductivity and the lowest polarization resistance of the cathode reaction compared to the doping vanadium compositions. In addition, the impedance spectra for a SFTVx/ LSGM/ NiFe cell at 800°C are shown in Figure 3.15. It can be seen that the polarization resistance value of single cell with SFTV05, SFTV1, SFTV2 and SFTV5 cathodes are 0.89, 0.95, 1.01 and 2.37 Ω·cm², respectively. It should be noticed that the polarization resistance of single cells increases with increasing the V content whereas the value of fuel cell performance decreases. Therefore, it can be

concluded that the cell performance was improved by the reduction of polarization resistance. And small amount of V and Nb doped on SFT improves the cell performance by reducing polarization resistance, enhancing ORR, and increasing conductivity. Furthermore, the maximum power density value and the polarization resistance value for SFTVx/ LSGM/ NiFe cells are summarized in Table 3.6.

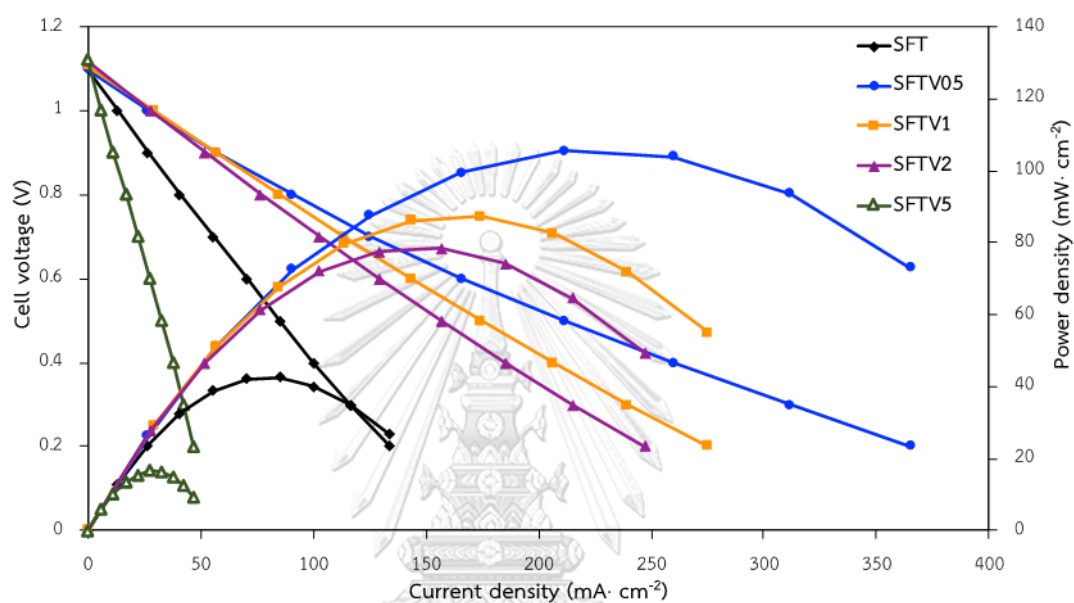


Figure 3.14 Cell voltage and power density as functions of current density for the single cell with $Sr_2FeTi_{1-x}V_xO_{6-\delta}$ ($x = 0.00, 0.05, 0.10, 0.20, 0.50$) cathode at $800^\circ C$

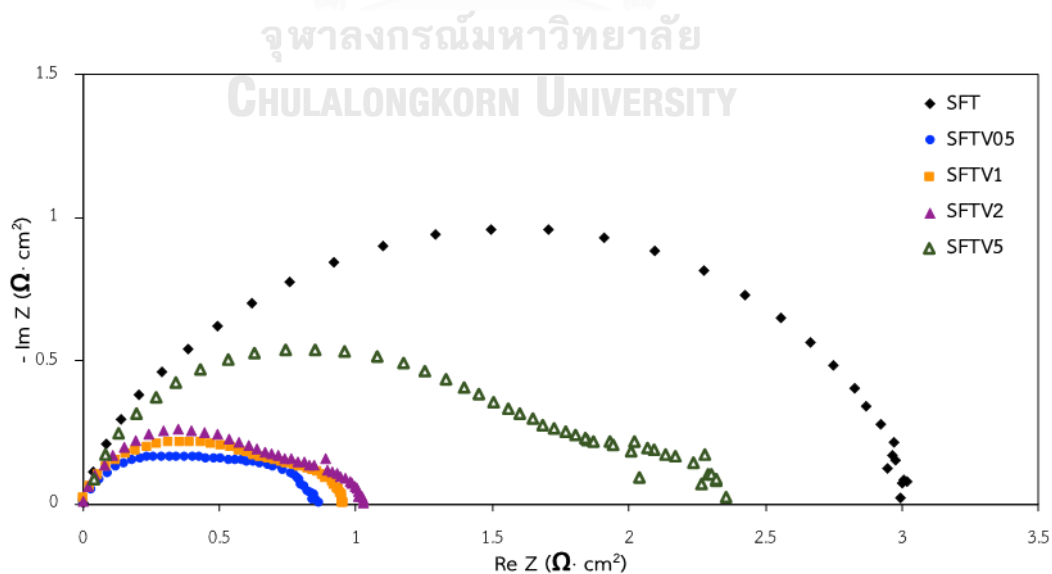


Figure 3.15 Impedance spectra of single cell with $Sr_2FeTi_{1-x}V_xO_{6-\delta}$ ($x = 0.00, 0.05, 0.10, 0.20, 0.50$) cathode at $800^\circ C$

Table 3.6 The maximum power density value and polarization resistance of a SFTVx/ LSGM/ NiFe cell at 800°C

	Maximum power density (mW·cm ⁻²)	R _p (Ω·cm ²)
SFT	43	2.99
SFTV05	106	0.89
SFTV1	87	0.95
SFTV2	78	1.01
SFTV5	17	2.37

Similar to the cell performance of Sr₂FeTi_{0.95}Nb_{0.05}O_{6-δ} cathode over the temperature range from 600 – 800°C, the power density of single cell for Sr₂FeTi_{0.95}V_{0.05}O_{6-δ} cathode decreased with decreasing temperature as shown in Figure 3.16. It can be seen that the maximum power density of Sr₂FeTi_{0.95}V_{0.05}O_{6-δ} cathode are 106, 53, 44, 34 and 24 mW·cm⁻² at 800, 750, 700, 650 and 600°C, respectively.

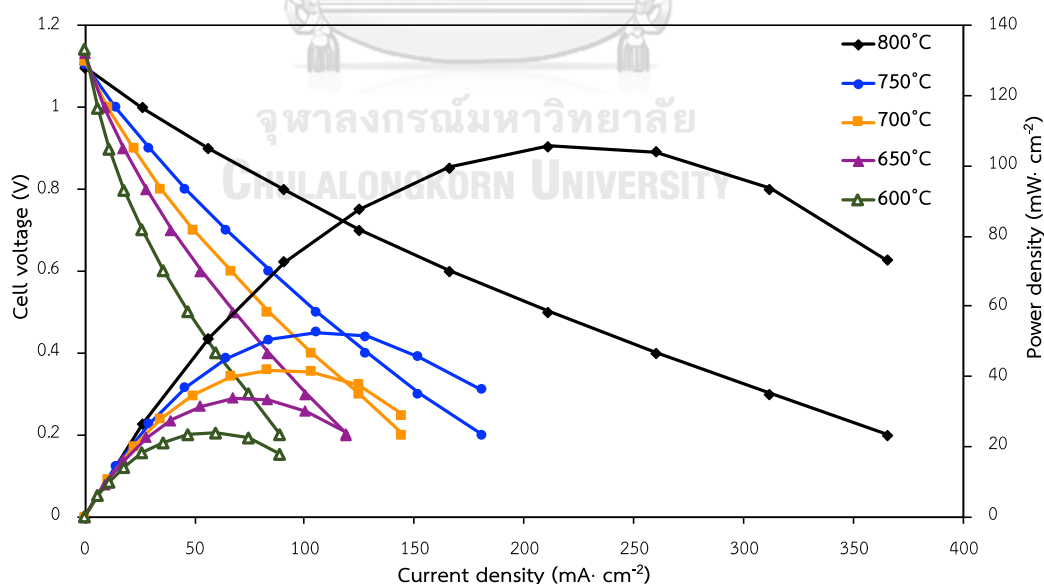


Figure 3.16 Cell voltage and power density as functions of current density for the single cell with Sr₂FeTi_{0.95}Nb_{0.05}O_{6-δ} cathode over the temperature range from 600 – 800°C

3.4.2 Testing of single cell performance using $\text{Sr}_2\text{FeTi}_{1-x}\text{M}_x\text{O}_{6-\delta}$ ($\text{M} = \text{Nb}, \text{V}$) oxides as the anode material

The fuel cell performance of $\text{Sr}_2\text{FeTi}_{1-x}\text{Nb}_x\text{O}_{6-\delta}$ ($x = 0.05, 0.1, 0.2, 0.5$) as anode was studied using cell configuration of SSC/ LSGM/ SFTNb x cells. Figure 3.17 presents the cell voltage and the power density of the single cells with SFTNb x anode as a function of current density measured at 800°C under wet hydrogen gas as the fuel and ambient air as the oxidant. It can be found that the materials can be used as the anode in SOFC and the maximum power density values of 60, 29, 23 and 16 $\text{mW}\cdot\text{cm}^{-2}$ were obtained for SFTNb05, SFTNb1, SFTNb2 and SFTNb5, respectively. However, when compared the use of materials as cathode, it can be seen that the power density of anode was lower than the cathode. This could be because the materials have more oxygen vacancy which facilitates the ORR reaction and the migration of oxide in the cathode side. With high amount of Nb, the cell performance was reduced and the polarization resistance was drastically increased. This could be due to the difficulty in oxide ion diffusion at the anode. The polarization resistance from Nyquist plots of SSC/ LSGM/ SFTNb x cell at 800°C is shown in Figure 3.18, as well as, Table 3.7 summarizes the polarization resistance value for single cell and the maximum power density value as anode of SFTNb x anode at 800°C.

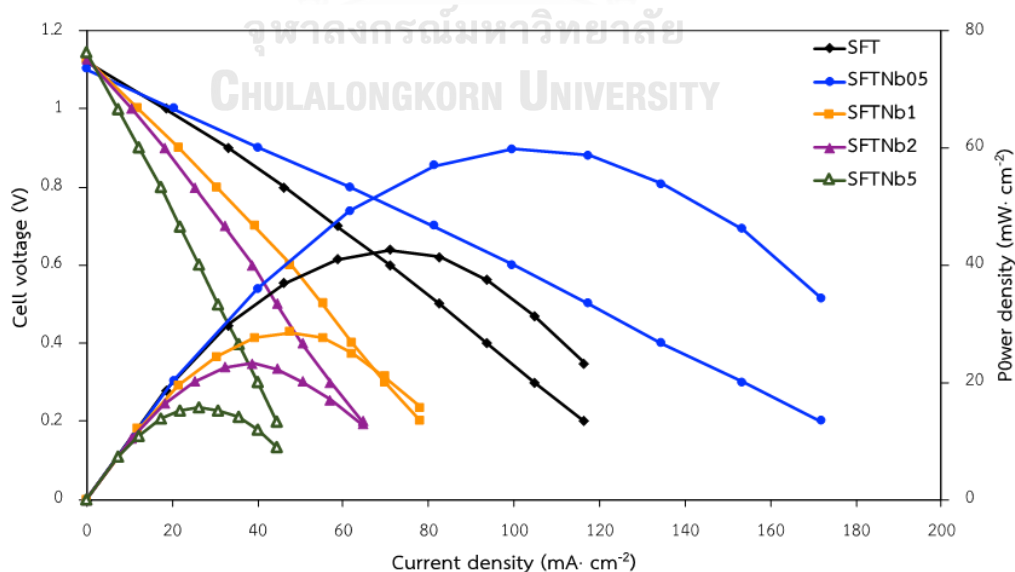


Figure 3.17 Cell voltage and power density as functions of current density for the single cell with $\text{Sr}_2\text{FeTi}_{1-x}\text{Nb}_x\text{O}_{6-\delta}$ ($x = 0.00, 0.05, 0.10, 0.20, 0.50$) anode at 800°C

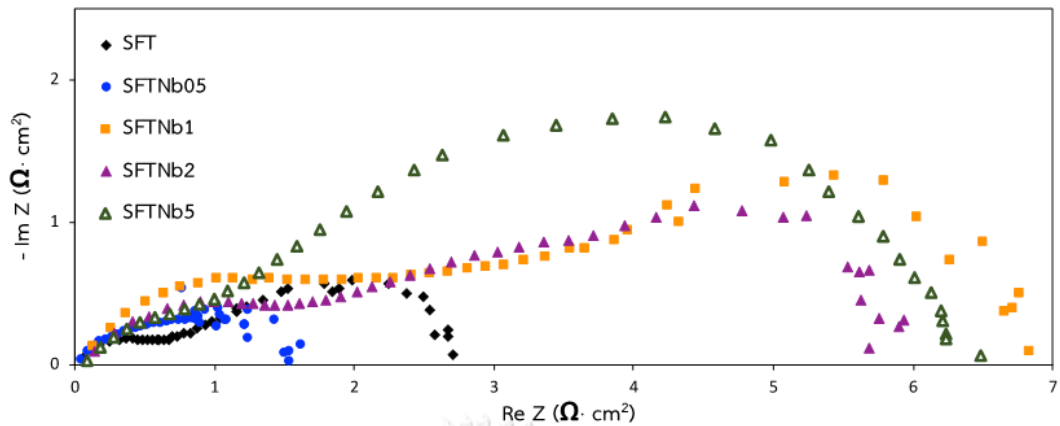


Figure 3.18 Impedance spectra of single cell with $Sr_2FeTi_{1-x}Nb_xO_{6-\delta}$ ($x = 0.00, 0.05, 0.10, 0.20, 0.50$) anode at $800^\circ C$

Table 3.7 The maximum power density value and polarization resistance of a SSC/LSGM/ SFTNbx cell with different compositions at $800^\circ C$

	Maximum power density ($mW \cdot cm^{-2}$)	R_p ($\Omega \cdot cm^2$)
SFT	42	2.70
SFTNb05	60	1.53
SFTNb1	29	6.83
SFTNb2	23	5.69
SFTNb5	16	6.49

Figure 3.19 displays the cell voltage and power density as a function of current density for the single cell with $Sr_2FeTi_{0.95}Nb_{0.05}O_{6-\delta}$ anode in the temperature range of $600 - 800^\circ C$. The maximum power density of $Sr_2FeTi_{0.95}Nb_{0.05}O_{6-\delta}$ anode are 60, 38, 24, 11 and $5 mW \cdot cm^{-2}$ at $800, 750, 700, 650$ and $600^\circ C$, respectively. It can also be observed that the power density decreased with decreasing temperature because the oxide ion diffusion is decreased.

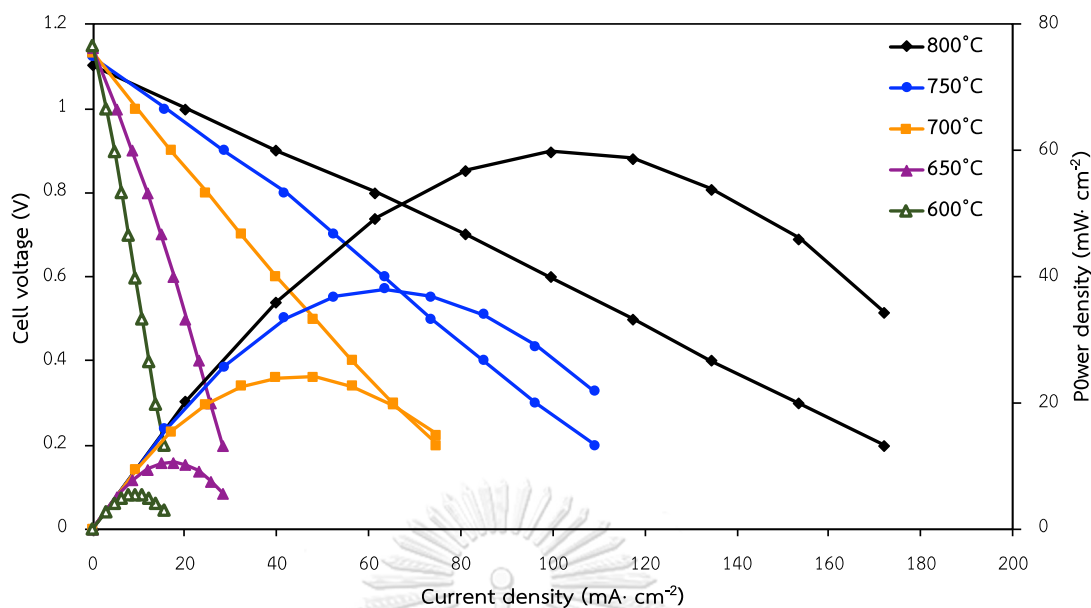


Figure 3.19 Cell voltage and power density as functions of current density for the single cell with $Sr_2FeTi_{0.95}Nb_{0.05}O_{6-\delta}$ anode over the temperature range from 600 – 800°C

Similar to the SFTNbx results, Figure 3.20 displays the cell voltage and the cell performance of single cell for SFTVx as anode and SSC as cathode with LSGM electrolyte measured at 800°C under pure H_2 as the fuel and ambient air as the oxidant. Figure 3.21 exhibits the typical impedance Nyquist plot of SSC/ LSGM/ SFTVx single cells at 800°C. SFTVx can also be used as the anode and the values of maximum power density are 86, 49, 21 and 12 $mW \cdot cm^{-2}$ for SFTV05, SFTV1, SFTV2 and SFTV5, respectively. The fuel cell performance increases with small amount of V doped by the reduction of polarization resistance and decreases with the increasing of V content. The increasing of cell performance and reducing of polarization resistance of low V-doped materials could be related with conductivity and structure of materials which facilitates electron migration. Summary of maximum power density value and polarization resistance value for difference compositions of SFTVx anode is presented in Table 3.8.

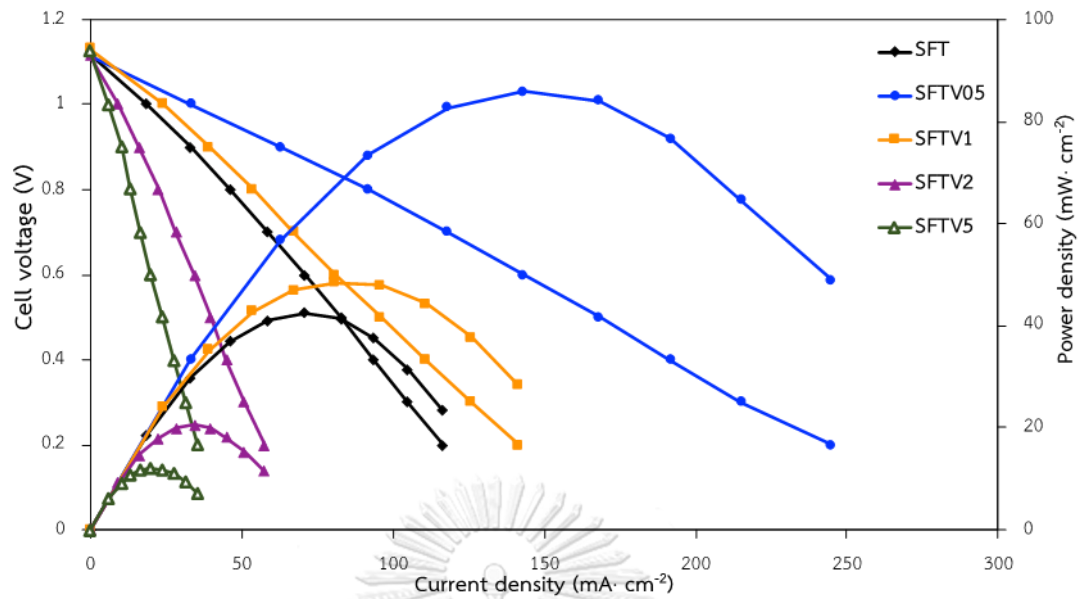


Figure 3.20 Cell voltage and power density as functions of current density for the single cell with $\text{Sr}_2\text{FeTi}_{1-x}\text{V}_x\text{O}_{6-\delta}$ ($x = 0.00, 0.05, 0.10, 0.20, 0.50$) anode at 800°C

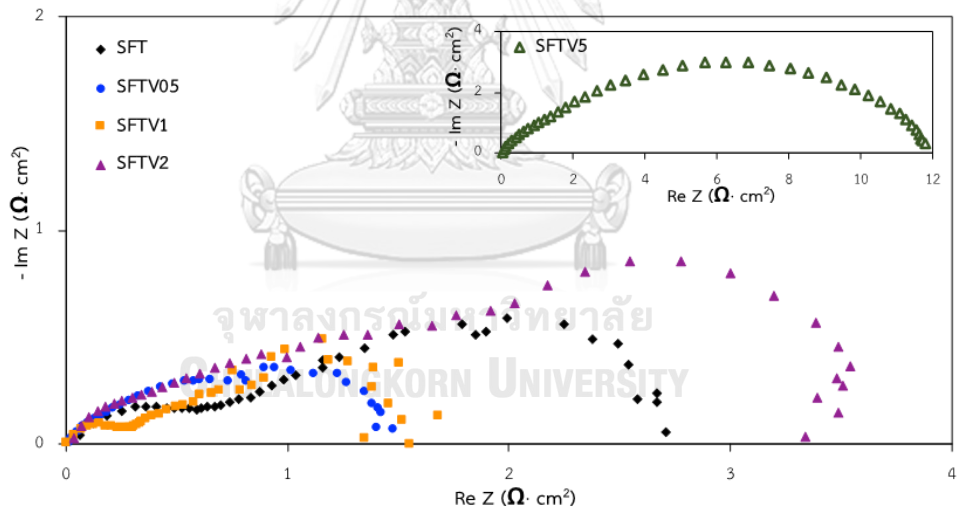


Figure 3.21 Impedance spectra of single cell with $\text{Sr}_2\text{FeTi}_{1-x}\text{V}_x\text{O}_{6-\delta}$ ($x = 0.00, 0.05, 0.10, 0.20, 0.50$) anode at 800°C

Table 3.8 The maximum power density value and polarization resistance of a SSC/LSGM/ SFTVx cell with different compositions at 800°C

	Maximum power density (mW·cm ⁻²)	R _p (Ω·cm ²)
SFT	42	2.70
SFTV05	86	1.35
SFTV1	49	1.55
SFTV2	21	3.49
SFTV5	12	11.82

Figure 3.22 presents the cell voltage and power density as functions of current density for the single cell with Sr₂FeTi_{0.95}V_{0.05}O_{6-δ} anode between 600 and 800°C. The maximum power density of Sr₂FeTi_{0.95}V_{0.05}O_{6-δ} anode are 86, 63, 43, 25 and 14 mW·cm⁻² at 800, 750, 700, 650 and 600°C, respectively. Similar result to the cell performance of Sr₂FeTi_{0.95}Nb_{0.05}O_{6-δ} anode, the power density of Sr₂FeTi_{0.95}V_{0.05}O_{6-δ} anode decreased with decreasing temperature.

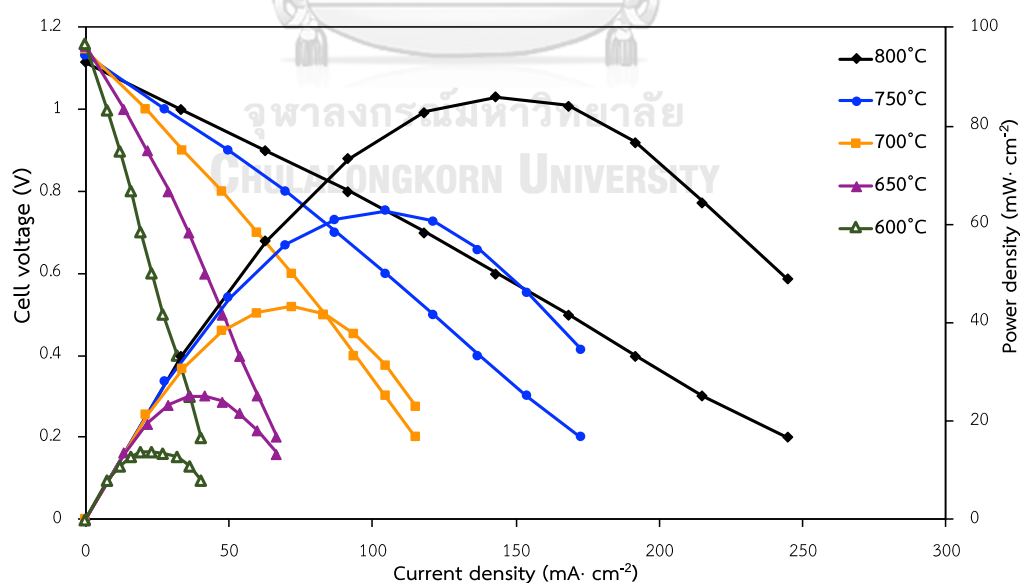


Figure 3.22 Cell voltage and power density as functions of current density for the single cell with Sr₂FeTi_{0.95}V_{0.05}O_{6-δ} anode over the temperature range from 600 – 800°C

In summary of this point, it can be concluded that SFTNb and SFTV can be used as either cathode or anode in SOFC. However, for the high power density of cell, the use of cathode is more preferable. In addition, only small amount of doped Nb and V in the range of 0.05 – 0.1 can enhance the cell performance.

3.4.3 Cell performance of symmetrical cell

The single cell performance testing of Nb-doped SFT and V-doped SFT demonstrate that for cathode, a small dopant of Niobium and Vanadium ($x = 0.05$) in SFT double perovskite displays the highest power density. Similarly, both SFTNb05 and SFTV05 exhibit the best cell performance for anode. Thus, SFTNb05 and SFTV05 was tested the fuel cell performance by using this sample as both anode and cathode with LSGM electrolyte. Figure 3.23 show the cell voltage and power density as a function of current density for SFT/ LSGM/ SFT, SFTNb05/ LSGM/ SFTNb05 and SFTV05/ LSGM/ SFTV05 cells measured at 800°C under humidified hydrogen gas as the fuel and ambient air as the oxidant. It can be seen that the maximum power density value of symmetrical cell for SFT, SFTNb05 and SFTV05 are 19.54, 14.62 and 19.42 $\text{mW}\cdot\text{cm}^{-2}$, respectively.

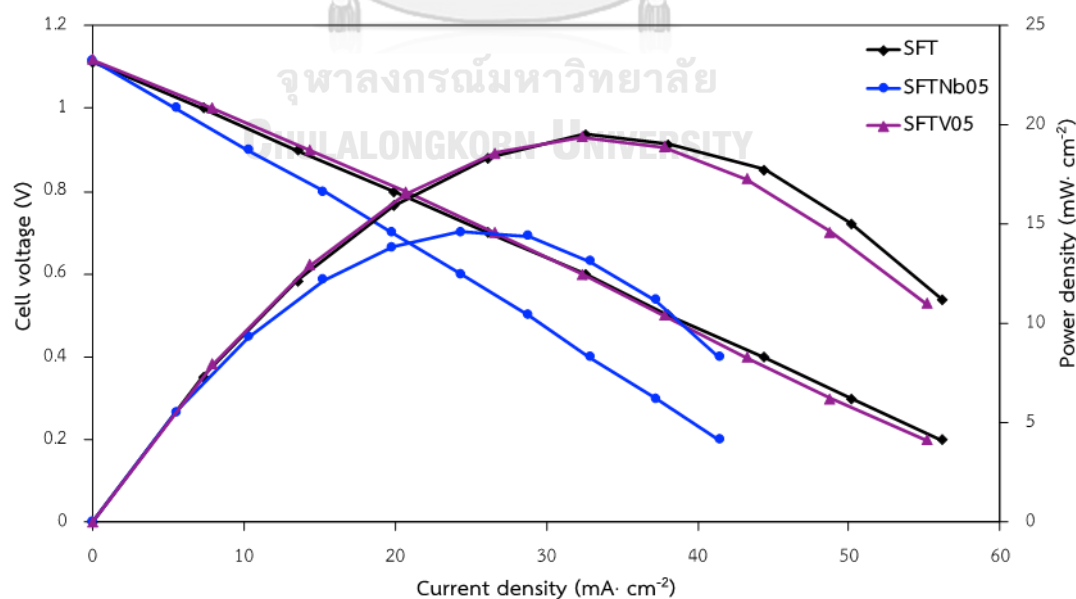


Figure 3.23 Cell voltage and power density as functions of current density for the symmetrical cell with SFT, SFTNb05 and SFTV05 electrode at 800°C

3.5 X-ray Photoelectron analysis

To understand the behavior of some electrochemical properties, the X-ray photoelectron spectroscopy (XPS) was used to characterize the chemical state of the element for $\text{Sr}_2\text{FeTi}_{1-x}\text{M}_x\text{O}_{6-\delta}$ ($M = \text{Nb}, \text{V}$) materials. The XPS spectra were deconvoluted by the CasaXPS program and the binding energy scale was calibrated against at 285.0 eV of the C 1s line.

3.5.1 XPS results of Nb-doped SFT double perovskites

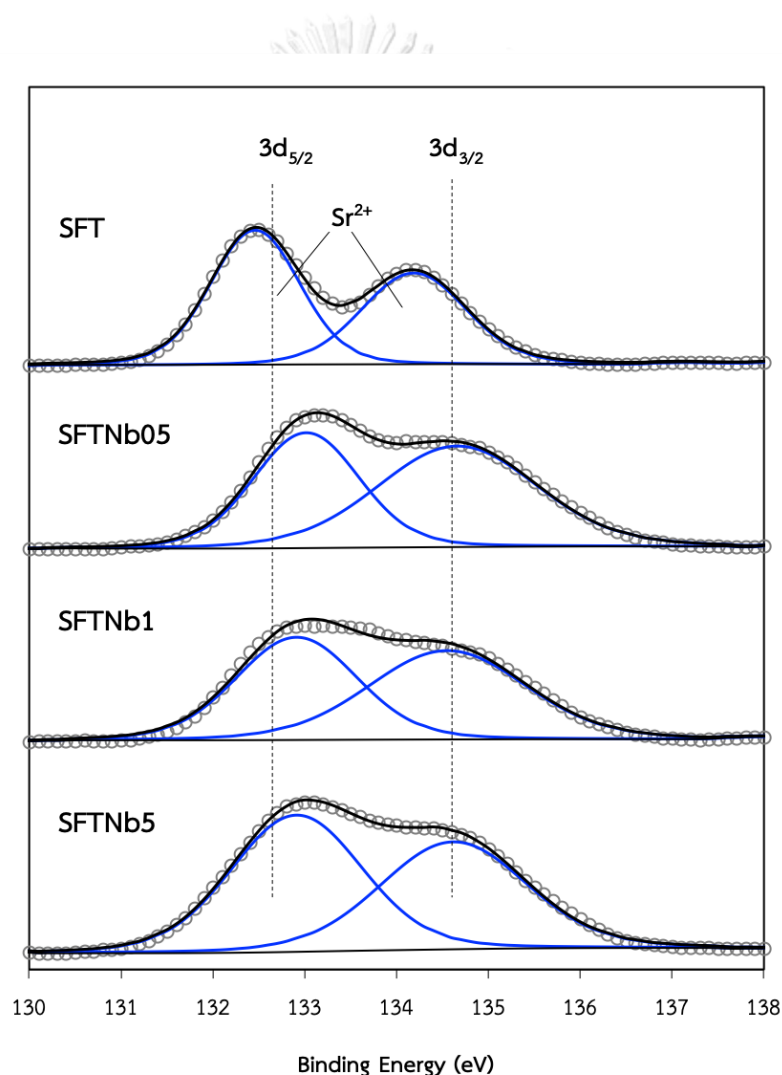


Figure 3.24 XPS spectra of Sr 3d for SFT and $\text{Sr}_2\text{FeTi}_{1-x}\text{Nb}_x\text{O}_{6-\delta}$ ($x = 0.05, 0.10, 0.50$) at room temperature

Figure 3.24 shows the Sr 3d core-level spectra for SFT, SFTNb05, SFTNb1 and SFTNb5 at room temperature and the fitting result. It can be seen that the Sr 3d spectra consists of two peaks; the peak at higher binding energy represents Sr 3d_{3/2} peak and the peak at lower binding energy indicates Sr 3d_{5/2} peak. In case of SFT sample, the Sr 3d peaks are 134.19 and 132.46 eV, respectively. While, the binding energy of Sr 3d_{3/2} for SFTNb05, SFTNb1 and SFTNb5 are 134.63 and 133.00 eV, 134.52 and 132.89 eV, 134.57 and 132.88 eV, respectively. The binding energy of the Sr 3d peak corresponds to the strontium ions in Sr²⁺ state, which is in good agreement with the work reported by W. yang et al. [90] and H. Zhang et al. [91].

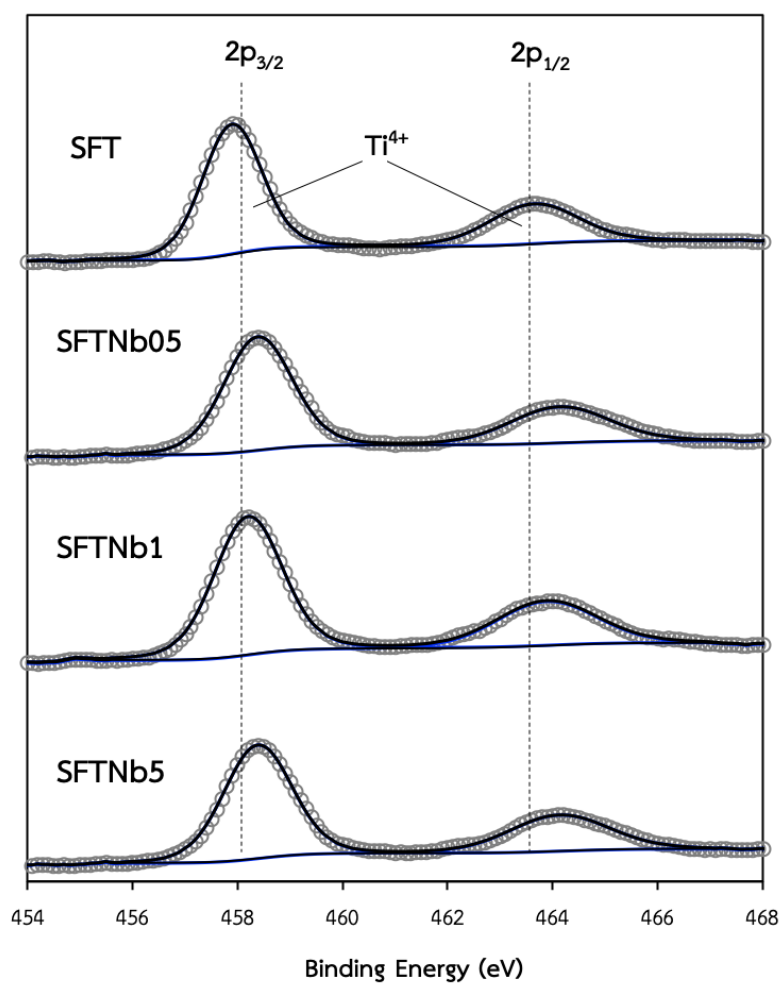


Figure 3.25 XPS spectra of Ti 2p for SFT and $Sr_2FeTi_{1-x}Nb_xO_{6-\delta}$ ($x = 0.05, 0.10, 0.50$) at room temperature

The XPS analyses of Ti 2p of the undoped and Nb-doped SFT oxide at room temperature are displayed in Figure 3.25. The deconvolution of each spectrum indicated the binding energy peaks of Ti 2p_{1/2} and Ti 2p_{3/2} around 463.64 and 457.89 eV, 464.13 and 458.39 eV, 463.89 and 458.20 eV, 463.88 and 458.09 eV for SFTNb_x when x = 0.00, 0.05, 0.10, 0.50, respectively. However, B. Bharti et al. argues that the splitting peak of Ti 2p_{1/2} and Ti 2p_{3/2} demonstrated the binding energy at 464.4 and 458.6 eV, respectively, and these peaks are corresponding with Ti⁴⁺ ions [92]. G. Elipe et al. also reported the binding energy of Ti⁴⁺ 2p_{3/2} in TiO₂, around 458.5 eV [93]. Therefore, it can be indicated that the valence state of Ti ions in all studied samples are +4, without Ti³⁺ and Ti²⁺ [94, 95].

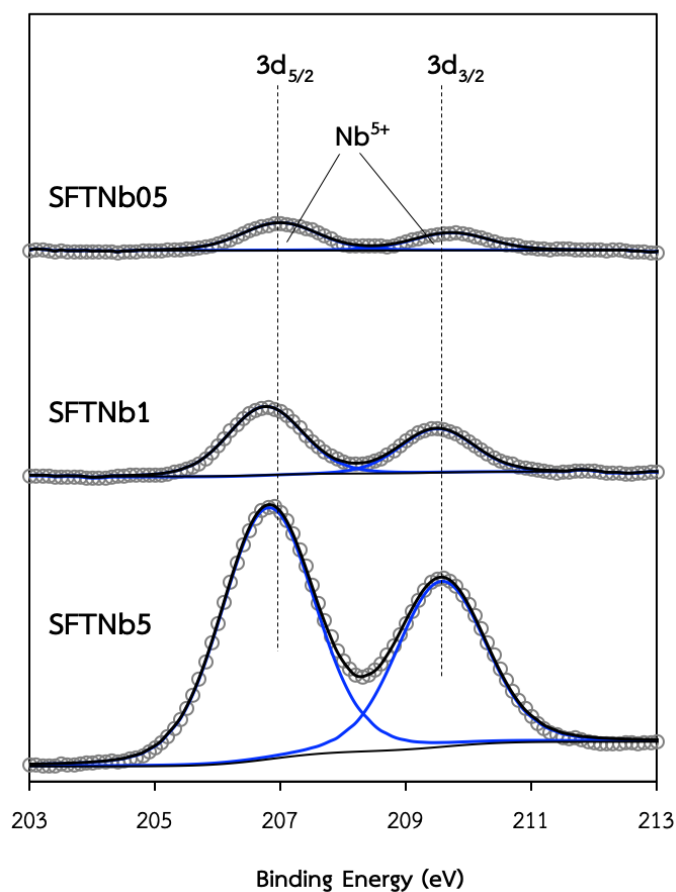


Figure 3.26 XPS spectra of Nb 3d for SFT and $\text{Sr}_2\text{FeTi}_{1-x}\text{Nb}_x\text{O}_{6-\delta}$ ($x = 0.05, 0.10, 0.50$) at room temperature

The XPS Nb 3d spectra for SFTNb05, SFTNb1 and SFTNb5 at room temperature are presented in Figure 3.26. This XPS spectra split into two peaks: Nb 3d_{3/2} and Nb 3d_{5/2}. The binding energy of Nb 3d_{5/2} are ~207.00, 206.76 and 206.82 for SFTNb05, SFTNb1 and SFTNb5, respectively. These binding energy values of Nb 3d_{5/2} peak were consistent with the values reported by B. Mei et al. for Nb⁵⁺ ions in Nb-doped TiO₂ material, which the binding energy was 206.8 eV [96] as well as the Nb-doped SrTiO₃ demonstrates the binding energy at 207.0 eV for Nb⁵⁺ 3d_{5/2} [97]. It is noticed that niobium in SFTNbx (x = 0.05, 0.10, 0.50) samples mainly exhibit the pentavalent state [98, 99].

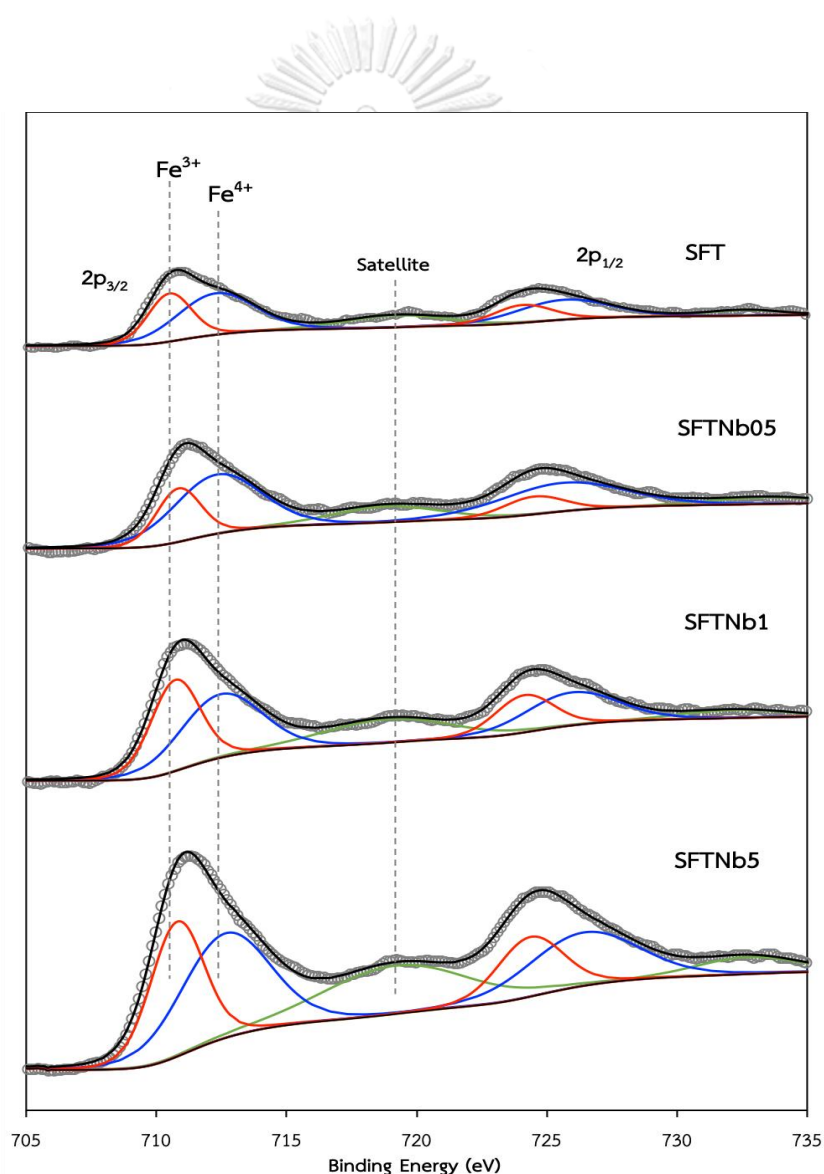


Figure 3.27 XPS spectra of Fe 2p for SFT and $\text{Sr}_2\text{FeTi}_{1-x}\text{Nb}_x\text{O}_{6-\delta}$ ($x = 0.05, 0.10, 0.50$) at room temperature

Figure 3.27 presents the Fe 2p XPS spectra of SFT, SFTNb05, SFTNb1 and SFTNb5 at room temperature. After deconvolution, the Fe 2p spectra for all samples are consisted of two iron species, which are Fe⁴⁺ and Fe³⁺ ions. No characteristic peak of Fe²⁺ is observed at ~709 (2p_{3/2}) and ~723 (2p_{1/2}) eV. For Fe 2p in SFT sample, the peaks of binding energy at 725.65 and 712.29 eV are assigned to Fe⁴⁺ 2p_{1/2} and Fe⁴⁺ 2p_{3/2}, respectively. While, the core-level binding energy at 724.07 and 710.50 eV are determined to Fe³⁺ 2p_{1/2} and Fe³⁺ 2p_{3/2}, respectively. Similarly, iron in Nb-doped SFT is in mixed valence state and the binding energy peaks of Fe⁴⁺ 2p_{1/2} and Fe⁴⁺ 2p_{3/2} are 725.55 and 712.33 eV, 725.95 and 712.47 eV, 726.41 and 712.65 eV for SFTNb05, SFTNb1, SFTNb5, respectively. For Fe³⁺ 2p_{1/2} and Fe³⁺ 2p_{3/2} in SFTNbx, the peaks of binding energy are 724.52 and 710.85 eV, 724.14 and 710.73 eV, 724.37 and 710.80 eV when x = 0.05, 0.10, 0.50, respectively. This is in good agreement with the results reported by J. Zhu et al. [100] and others [101, 102]. Furthermore, the satellite peaks of Fe 2p suggests the charge transfer from the anion valence band to the d band of Fe [103, 104]. This shake-up satellite peak has been found approximately between 718.8 – 719.2 eV, which is involved with the Fe 2p_{3/2} [105]. Moreover, the increasing amount of large charge (Fe⁴⁺) leads to the chemical shift to higher binding energy and changing of the satellite shape as in agreement with the report of M. Ghaffari et. al. [106]. The Fe⁴⁺/Fe³⁺ ratio was calculated based on the peak area and presented in Table 3.9. The increasing of Fe⁴⁺/Fe³⁺ ratio promotes the electron hopping between Fe³⁺ and Fe⁴⁺ [107], thus the electronic conductivity should be increased. In this work, it is clearly observed that the conductivity of SFTNb05 was increased with the higher Fe⁴⁺ ratio, in comparison with SFT perovskite. When Nb content (x = 0.10) was increased, the decreasing of Fe⁴⁺ ratio resulted in the lower conductivity of materials.

Table 3.9 Calculated Ratio of Fe 2p_{3/2} for SFT and Sr₂FeTi_{1-x}Nb_xO_{6-δ} (x = 0.05, 0.10, 0.50) oxides

Samples	Binding energy of Fe 2p _{3/2} (eV)		Peak area of Fe 2p _{3/2}		Ratio of Fe 2p _{3/2}
	Fe ³⁺	Fe ⁴⁺	Fe ³⁺	Fe ⁴⁺	Fe ⁴⁺ / Fe ³⁺
SFT	710.50	712.29	8625.04	13183.59	1.53
SFTNb05	710.85	712.33	9799.56	21300.51	2.17
SFTNb1	710.73	712.47	18485.37	21204.49	1.15
SFTNb5	710.80	712.65	29698.63	38393.99	1.29

The O 1s XPS spectra of SFT, SFTNb05, SFTNb1 and SFTNb5 at room temperature are shown in Figure 3.28. It is clearly seen that the deconvolution of broad O 1s spectra indicates two contributions. The first peak at lower binding energy ~ 528.5 – 530.0 eV corresponds to the lattice oxygen (O_L), whereas the peak at higher binding energy ~ 531.0 – 531.5 eV is associated with the adsorbed oxygen (O_A) [108-110]. In this case, the adsorbed oxygen is correlated with the surface oxygen vacancies [111]. Thus, the binding energy values at 529.10 eV, 529.62 eV, 529.55 eV and 529.57 eV for SFT, SFTNb05, SFTNb1 and SFTNb5, respectively, are O²⁻ species in the lattice and those at 531.20 eV, 531.53 eV, 531.40 eV and 531.43 eV are assigned to the adsorbed oxygen. The percentage between the adsorbed oxygen and lattice oxygen was calculated based on the peak areas of each type and summarized in Table 3.10. SFTNb05 sample has the highest percentage of adsorbed oxygen which means that SFTNb05 has higher surface oxygen vacancies than other series, thus the electrochemical activity such as oxygen adsorption, oxygen dissociation, and surface exchange coefficient at ORR is better improved [112]. This result can explain the reason for the lower polarization resistance and higher power density of asymmetrical cell of SFTNb05.

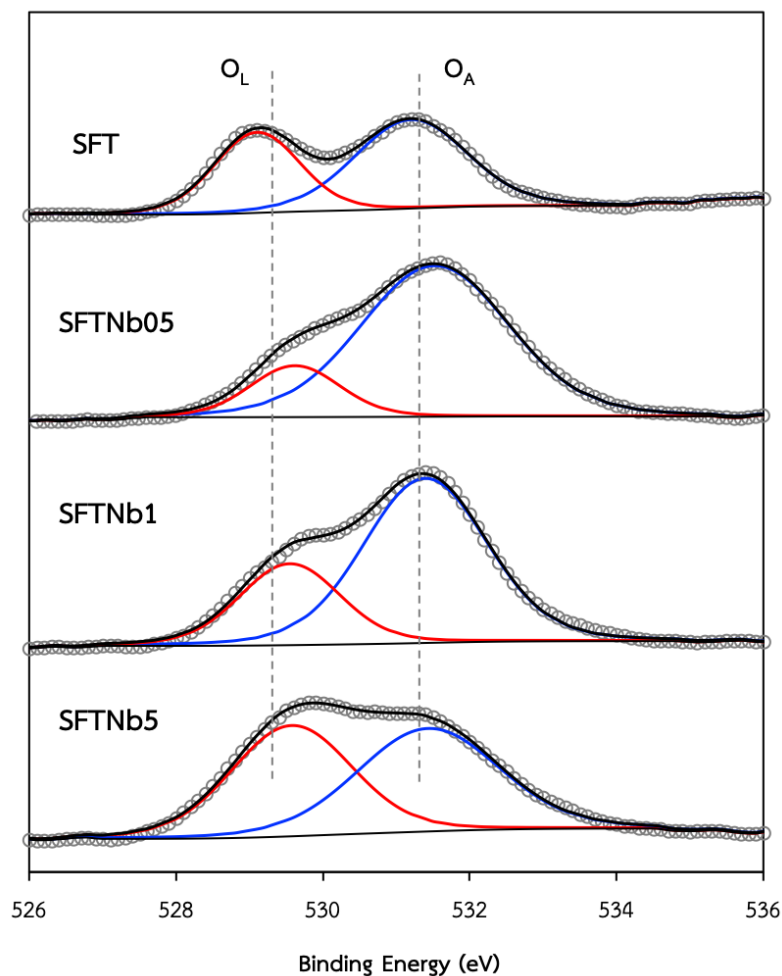


Figure 3.28 XPS spectra of O 1s for SFT and $\text{Sr}_2\text{FeTi}_{1-x}\text{Nb}_x\text{O}_{6-\delta}$ ($x = 0.05, 0.10, 0.50$) at room temperature

Table 3.10 Calculated ratio between adsorbed oxygen and lattice oxygen for SFT and $\text{Sr}_2\text{FeTi}_{1-x}\text{Nb}_x\text{O}_{6-\delta}$ ($x = 0.05, 0.10, 0.50$) oxides

Samples	Binding energy of O 1s (eV)		Peak area of O 1s		$\text{O}_A / (\text{O}_A + \text{O}_L)$ [%]*
	O_L	O_A	O_L	O_A	
SFT	529.10	531.20	19302.46	27708.62	58.940
SFTNb05	529.26	531.53	12854.18	62331.40	82.90
SFTNb1	529.55	531.40	22813.95	56534.16	71.25
SFTNb5	529.57	531.43	37368.63	40619.55	52.08

*[113]

3.5.2 XPS results of V-doped SFT double perovskites

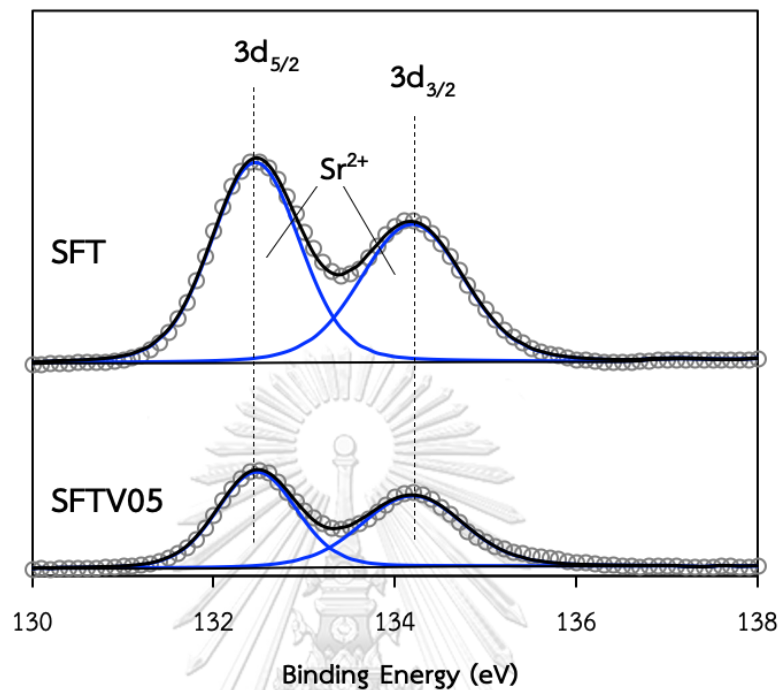


Figure 3.29 XPS spectra of Sr 3d for SFT and SFTV05 samples at room temperature

The fitting results of the Sr 3d core-level spectra for SFT and SFTV05 perovskite materials are shown in Figure 3.29. The Sr 3d signal of SFTV05 displayed peaks at 134.19 and 132.48 eV for Sr $3d_{3/2}$ and Sr $3d_{5/2}$, respectively. These Sr 3d peaks are attributed to the strontium ions in Sr^{2+} state.

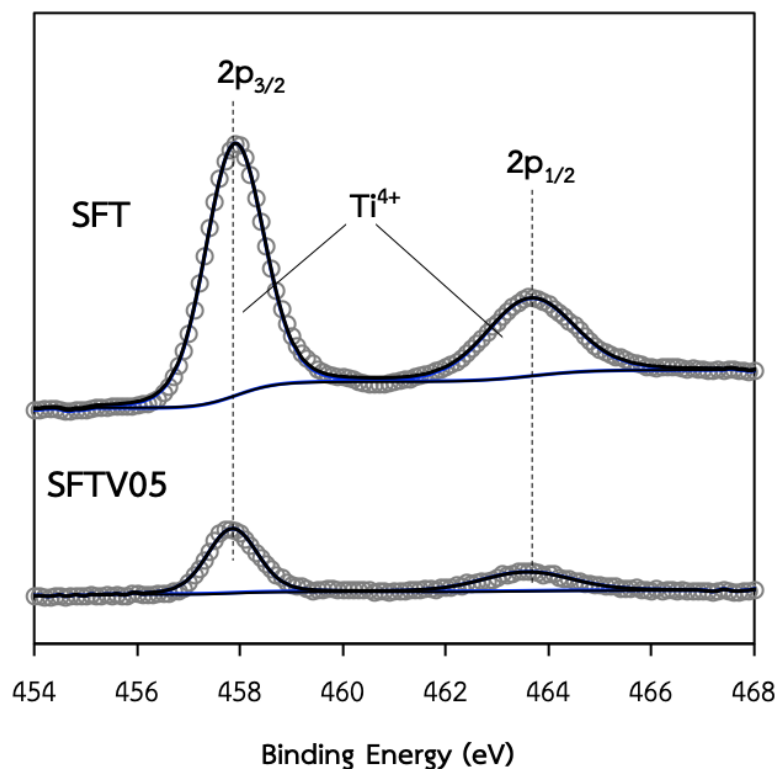


Figure 3.30 XPS spectra of Ti 2p for SFT and SFTV05 samples at room temperature

Figure 3.30 illustrates the XPS analyses of Ti 2p of SFT and SFTV05 oxides at room temperature. For SFTV05 sample, the doublet Ti $2p_{3/2}$ and Ti $2p_{1/2}$ peak demonstrates the binding energy at 463.58 and 457.85 eV, respectively. These peaks are also consistent with Ti^{4+} in perovskite lattice, similar to the Ti 2p XPS spectra of Nb-doped SFT oxides.

The V 2p is split into V $2p_{3/2}$ and V $2p_{1/2}$, but Figure 3.31 displays only the XPS analyses of V $2p_{3/2}$ for SFTV05 perovskite oxide. The binding energy at 517.10 eV was assigned for V $2p_{3/2}$ peak which corresponded with V in the +5 oxidation state, and in agreement with the value reported in literature of H.W. Liu et al. [114] and other [115]. That suggests V has been in cooperated in the structure.

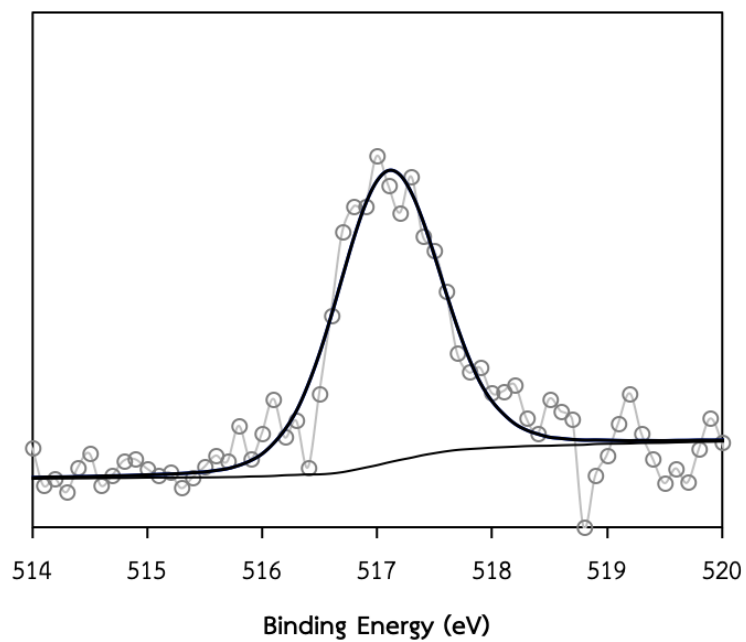


Figure 3.31 XPS spectra of V 2p for SFTV05 sample at room temperature

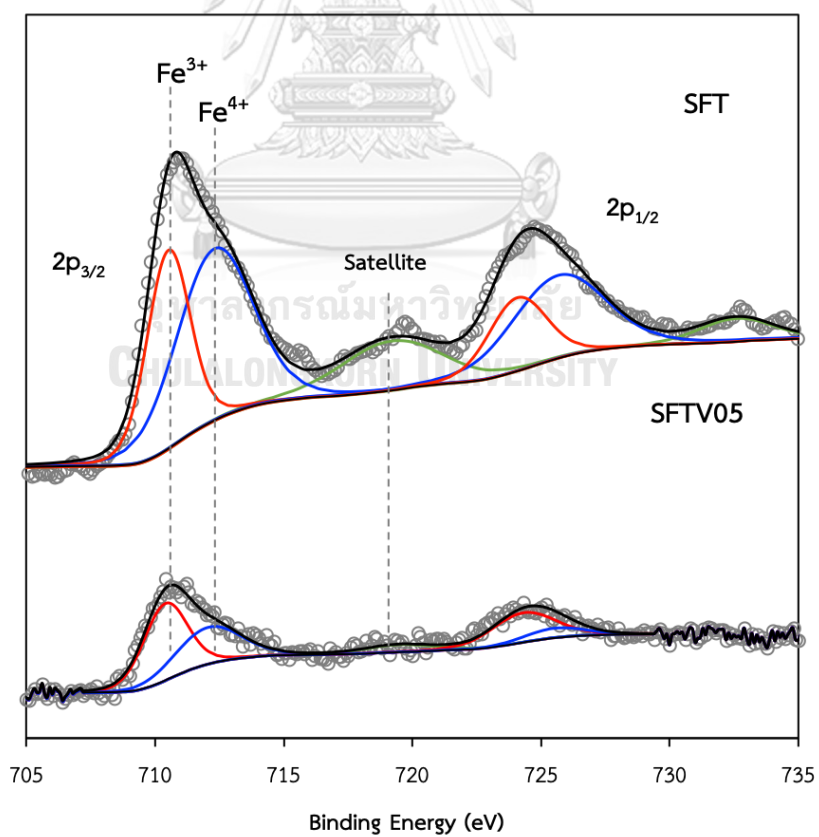


Figure 3.32 XPS spectra of Fe 2p for SFT and SFTV05 samples at room temperature

Figure 3.32 presents the Fe 2p XPS spectra of SFT and SFTV05. For SFTV05 perovskite material, the peaks at the binding energy of 724.3 and 710.38 eV are attributed to $\text{Fe}^{3+} 2p_{1/2}$ and $\text{Fe}^{3+} 2p_{3/2}$, respectively. While the binding peaks of $\text{Fe}^{4+} 2p_{1/2}$ and $\text{Fe}^{4+} 2p_{3/2}$ appeared at 725.53 and 712.06 eV, respectively. Similar to the SFT oxide, the peak at ~ 719 eV of SFTV05 was assigned to the satellite peak for Fe 2p core level. Additionally, the $\text{Fe}^{4+}/\text{Fe}^{3+}$ ratio of these samples was calculated as shown in Table 3.11. It can be also observed that the V-doped SFT with $x = 0.05$ has lower $\text{Fe}^{4+}/\text{Fe}^{3+}$ ratio than the SFT based perovskite due to the higher valence state of V^{5+} made the reduction of Fe^{4+} to Fe^{3+} to keep electroneutrality.

Table 3.11 Calculated Ratio of Fe $2p_{3/2}$ for SFT and SFTV05 oxides

Samples	Binding energy of Fe $2p_{3/2}$ (eV)		Peak area of Fe $2p_{3/2}$		Ratio of Fe $2p_{3/2}$
	Fe^{3+}	Fe^{4+}	Fe^{3+}	Fe^{4+}	$\text{Fe}^{4+}/\text{Fe}^{3+}$
SFT	710.50	712.29	8625.04	13183.59	1.53
SFTV05	710.38	712.06	3407.44	2410.02	0.71

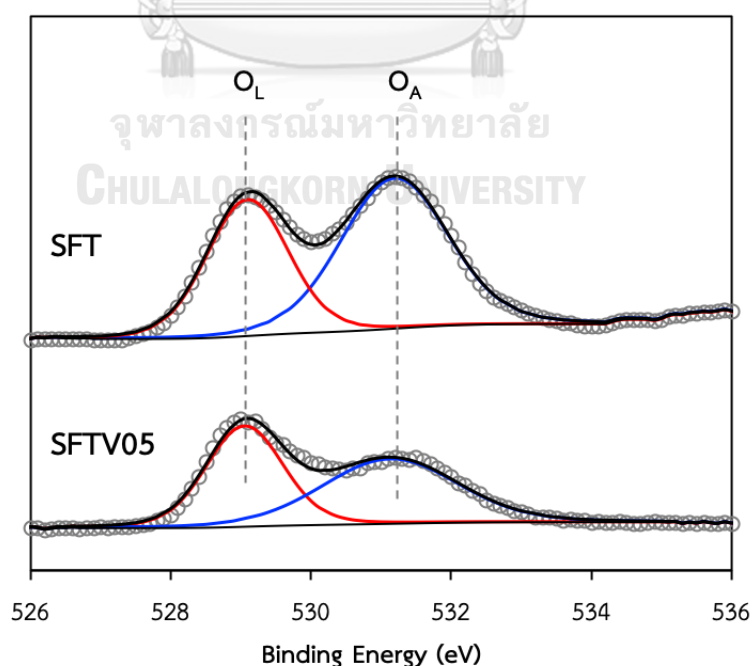


Figure 3.33 XPS spectra of O 1s for SFT and SFTV05 samples at room temperature

Figure 3.33 shows the O 1s XPS spectra of SFT and SFTV05. The peak at the binding energy position of 529.06 eV corresponds to the adsorbed oxygen (O_A), while peak at 531.14 eV are determined to the lattice oxygen (O_L) in SFTV05 perovskite material. It can also be seen from Table 3.12 that the percentage of adsorbed oxygen of SFTV05 oxide is decreased compared with that of the based SFT oxide. Thus, the electrochemical performance of SFTV relates with the oxygen vacancy in lattice structure.

Table 3.12 Calculated ratio between adsorbed oxygen and lattice oxygen for SFT and SFTV05 oxides

samples	Binding energy of O 1s (eV)		Peak area of O 1s		$O_A / (O_A + O_L)$ [%]*
	O_L	O_A	O_L	O_A	
SFT	529.10	531.20	19302.46	27708.62	58.94
SFTV05	529.06	531.14	13244.45	15122.65	53.31

*[113]

3.5 Thermal expansion

Thermal expansion coefficient (TEC) of material is also a significant property to enhance the SOFC cell performance because the mismatch of TECs between electrode and electrolyte during the operating temperature causes the excessive thermal stress on the materials, leading to the delamination in the electrode. Therefore, the TECs of electrode and electrolyte should have similar values in order to reduce the mechanical compatibility problem [116, 117]. Figure 3.34 shows the thermal expansion curves of SFT, SFTNb05 and SFTV05 from room-temperature to 1000°C in air atmosphere. These materials have similar thermal behavior as a linear correlation at low temperature (< 350°C) and nonlinear behavior due to an oxygen release in the perovskite structure with the generation of oxygen vacancies [118-121] at temperature greater than 350°C. However, the TEC values of Nb-doped SFT doesn't differ from that of SFT whereas the value slightly increases in case of doping V. The average TEC values of SFT,

SFTNb05 and SFTV05 from the temperature of 30 – 1000°C are 13.4151×10^{-6} , 13.8478×10^{-6} and $16.1762 \times 10^{-6} \text{ K}^{-1}$, respectively. Compared to the LSGM electrolyte, the average TEC value of LSGM reported by Z. wang et al. is $11.7 \times 10^{-6} \text{ K}^{-1}$ [122], as a result, SFT and SFTNb05 electrodes are more compatible with LSGM electrolyte than SFTV05 electrode. The matching of electrode and electrolyte provides the use in long-term operation for the IT-SOFC electrode application. In contrast, the SFTV oxide is high thermal expansion than SFTNb05 oxides, therefore, the LSGM electrolyte cell with SFTV05 electrode may be cracked and delaminated in long term operating conditions easily. The reason for the high TEC value in SFTV may be related with higher oxygen in lattice compared to both SFT and SFTNb05, thus the increasing temperature can make the easier loss of oxygen from the lattice.

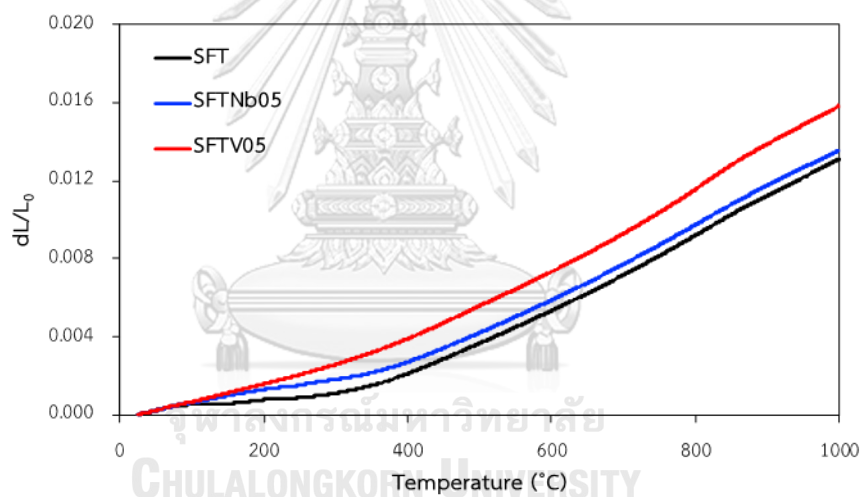


Figure 3.34 Thermal expansion curves of SFT, SFTNb05 and SFTV05 as a function temperature in air

3.7 The chemical compatibility

The chemical compatibility between electrode and electrolyte is one of many factors to evaluate the SOFC performance because during operation, the interfacial chemical reaction of electrolyte with electrode material may produce the impurity phases, which probably increases the interfacial polarization resistance of the SOFC cell and may cause the degradation of the cell. Thereby, the chemical compatibility of SFT, SFTNb05 and SFTV05 oxides with LSGM electrolyte was performed by physical

mixing of materials and electrolyte in the ratio of 1: 1 and examined by XRD after heated the mixture to 900°C (temperature above the SOFC cell operating temperature) for 5 hours. Figure 35 – 37 indicate the XRD pattern of the mixture between LSGM powder and SFT, SFTNb05, SFTV05 oxides powder (1: 1%wt ratio). It is clearly seen that the calcined mixtures show the structures of starting reactants, LSGM and double perovskite oxides of pure SFT, SFTNb05, SFTV05. There is also neither impurity phase nor peak shifting observed in the XRD pattern of the calcined mixtures. This means that SFT, SFTNb05 and SFTV05 oxides have a good chemical compatibility with LSGM perovskite as the electrolyte during the cell operation. Thus, this result demonstrated that the SFT, SFTNb05 and SFTV05 double perovskites are appropriate for SOFCs as the electrode material.

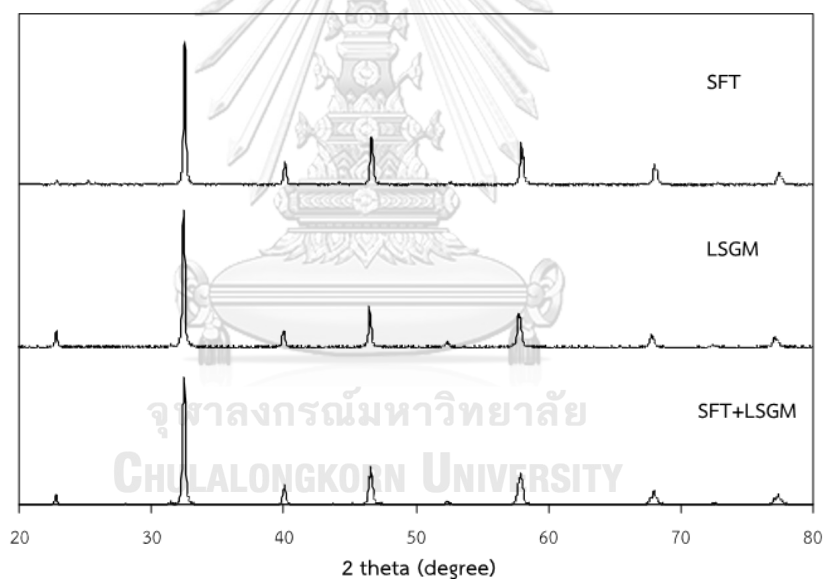


Figure 3.35 XRD pattern of SFT powder, LSGM powder and LSGM-SFT mixture calcined at 900°C for 5 hours in air

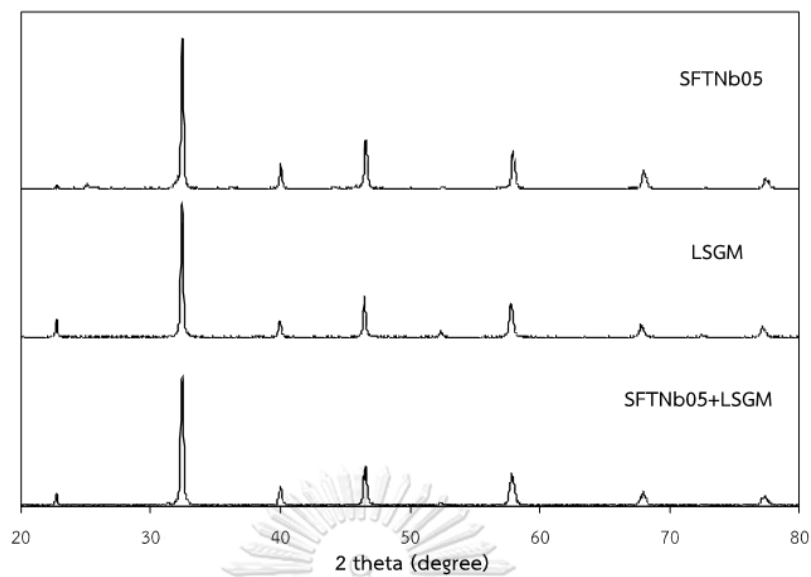


Figure 3.36 XRD pattern of SFTNb05 powder, LSGM powder and LSGM-SFTNb05 mixture calcined at 900°C for 5 hours in air

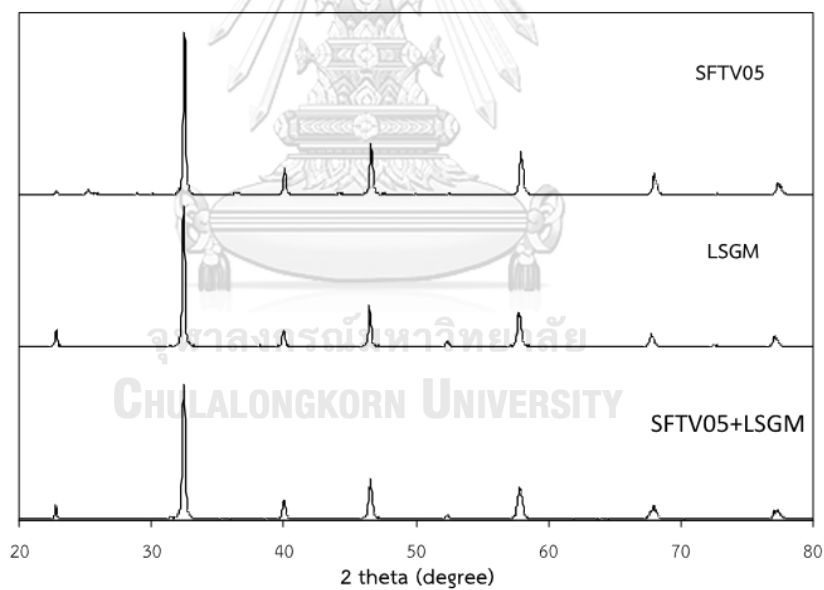


Figure 3.37 XRD pattern of SFTV05 powder, LSGM powder and LSGM-SFTV05 mixture calcined at 900°C for 5 hours in air

CHAPTER 4

CONCLUSION

4.1 Conclusion

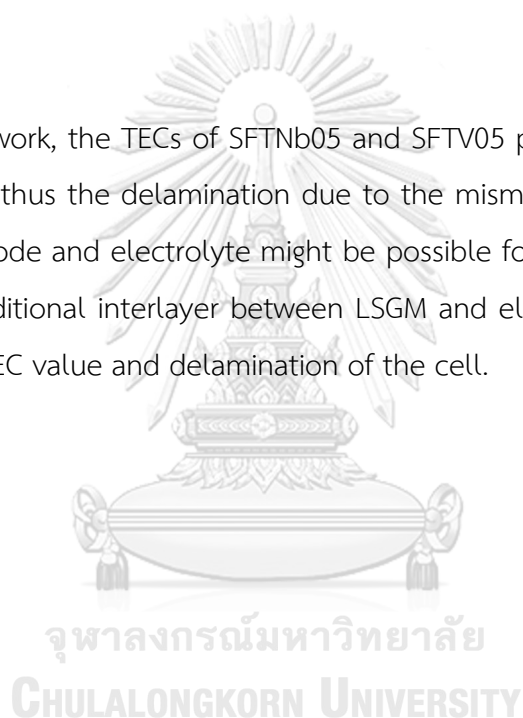
The substitution of niobium and vanadium on titanium site in $\text{Sr}_2\text{FeTiO}_{6-\delta}$ (SFT) double perovskite has been investigated for conductivity and electrochemical performance as the electrode materials in IT-SOFC. $\text{Sr}_2\text{FeTi}_{1-x}(\text{Nb}, \text{V})_x\text{O}_{6-\delta}$ ($x = 0.00 - 0.50$) oxides were synthesized by conventional solid state reaction with calcination at 1050°C and sintering at 1250°C for 12 hours. The X-ray diffraction analyses reveal that all metal-doped samples have the double perovskite structure and impurity phases of $\text{Sr}(\text{FeNb})_{0.5}\text{O}_3$ and $\text{Sr}_3(\text{VO}_4)_2$ for Nb-doped SFT and V-doped SFT, respectively, however no impurity phases were found in SFTNb05 and SFTV05 oxides. The amount of these impurity phases also increased with increasing x ratio. The electrical conductivity and polarization resistance of SFT were $2.00 \text{ S}\cdot\text{cm}^{-1}$ and $6.42 \Omega\cdot\text{cm}^2$, respectively. When Nb was substituted in SFT, the conductivity increased with the small amount of Nb doped and decreased with high amount of Nb, which relates to the $\text{Fe}^{4+}/\text{Fe}^{3+}$ ratio. The high $\text{Fe}^{4+}/\text{Fe}^{3+}$ ratio of SFTNb05 promoted the electrical conductivity of materials. For the Nb-doped series, SFTNb05 exhibited the highest conductivity around $\sim 2.44 \text{ S}\cdot\text{cm}^{-1}$. For V-doped perovskites, the conductivity was in similar trend with the Nb series and SFTV05 has higher electrical conductivity, which was $\sim 3.93 \text{ S}\cdot\text{cm}^{-1}$, than others. The thermal expansion behavior study indicated that the TEC value of SFT slightly increased with increasing metal dopant.

For the electrochemical performance test as cathode and anode in IT-SOFC under LSGM electrolyte, H_2 fuel gas and O_2 oxidant, the V and Nb doped materials were active to be used as both cathode and anode, and small amount of V and Nb doping doubly improved the cell performance of SFT. For asymmetric cell performance, the maximum power density of SFT cathode was $\sim 42.61 \text{ mW}\cdot\text{cm}^{-2}$ at 800°C whereas the maximum power densities of SFTNb05 and SFTV05 cathodes were $79 \text{ mW}\cdot\text{cm}^{-2}$ and $106 \text{ mW}\cdot\text{cm}^{-2}$, respectively. For asymmetrical cell performance as anode, the maximum power densities of SFTNb05 and SFTV05 were $60 \text{ mW}\cdot\text{cm}^{-2}$ and

86 $\text{mW}\cdot\text{cm}^{-2}$ at 800°C, respectively. However, the symmetrical cell test of both materials exhibit low performance value compared with the asymmetric cell. Furthermore, the chemical compatibility study revealed that SFTNb05 and SFTV05 are compatible with LSGM electrolyte at 900°C for 5 hours. In conclusion, these primary results show that SFTNb05 and SFTV05 have potentials to be used as electrode materials in asymmetric IT-SOFC and their property can be improved much better if some factors such as the mismatch in thermal expansion between electrode and electrolyte, type of electrolyte are eliminated.

4.2 Suggestion

From this work, the TECs of SFTNb05 and SFTV05 perovskites are higher than LSGM electrolyte, thus the delamination due to the mismatch in thermal expansion behavior of electrode and electrolyte might be possible for the long-term operation. Therefore, the additional interlayer between LSGM and electrode can be a solution for reducing the TEC value and delamination of the cell.



REFERENCES

1. Florides, G.A. and P. Christodoulides, *Global warming and carbon dioxide through sciences*. Environment International, 2009. **35**(2): p. 390-401.
2. Massardo, A.F., M. Santarelli, and R. Borchiellini, *Carbon exergy tax (CET): its impact on conventional energy system design and its contribution to advanced systems utilisation*. Energy, 2003. **28**(7): p. 607-625.
3. Steele, B.C.H. and A. Heinzl, *Materials for fuel-cell technologies*. Nature, 2001. **414**(6861): p. 345-352.
4. Lucia, U., *Overview on fuel cells*. Renewable and Sustainable Energy Reviews, 2014. **30**: p. 164-169.
5. Sharaf, O.Z. and M.F. Orhan, *An overview of fuel cell technology: Fundamentals and applications*. Renewable and Sustainable Energy Reviews, 2014. **32**: p. 810-853.
6. Andújar, J.M. and F. Segura, *Fuel cells: History and updating. A walk along two centuries*. Renewable and Sustainable Energy Reviews, 2009. **13**(9): p. 2309-2322.
7. Ramadhani, F., et al., *Optimization strategies for Solid Oxide Fuel Cell (SOFC) application: A literature survey*. Renewable and Sustainable Energy Reviews, 2017. **76**: p. 460-484.
8. Brandon, N.P. and M.A. Parkes, *Fuel Cells: Materials*. 2016.
9. Choudhury, A., H. Chandra, and A. Arora, *Application of solid oxide fuel cell technology for power generation—A review*. Renewable and Sustainable Energy Reviews, 2013. **20**: p. 430-442.
10. Irshad, M., et al., *A Brief Description of High Temperature Solid Oxide Fuel Cell's Operation, Materials, Design, Fabrication Technologies and Performance*. Vol. 6. 2016. 75.
11. Singhal, S.C., *Solid Oxide Fuel Cells*. The Electrochemical Society Interface, 2007. **16**: p. 41-44.

12. Ranasinghe, S.N., H.S.G. Pussewalage, and P.H. Middleton. *Performance analysis of single cell solid oxide fuel cells*. in *2017 Moratuwa Engineering Research Conference (MERCon)*. 2017.
13. Soottitantawat, A., et al., *Reviews on Solid Oxide Fuel Cell Technology*. Vol. 13. 2009.
14. Abdalla, A.M., et al., *Nanomaterials for solid oxide fuel cells: A review*. *Renewable and Sustainable Energy Reviews*, 2018. **82**: p. 353-368.
15. Basu, R., *Materials for solid oxide fuel cells*. 2007. 286-331.
16. Arabaci, A. and M.F. Öksüzömer, *Preparation and characterization of 10mol% Gd doped CeO₂ (GDC) electrolyte for SOFC applications*. *Ceramics International*, 2012. **38**(8): p. 6509-6515.
17. Joshi, A.V., et al., *Solid Electrolyte Materials, Devices, and Applications*. *Journal of Electroceramics*, 2004. **13**(1): p. 619-625.
18. Huang, K. and J.B. Goodenough, *A solid oxide fuel cell based on Sr- and Mg-doped LaGaO₃ electrolyte: the role of a rare-earth oxide buffer*. *Journal of Alloys and Compounds*, 2000. **303-304**: p. 454-464.
19. Naiqing, Z., et al., *Study on Properties of LSGM Electrolyte Made by Tape Casting Method and Applications in SOFC*. *Journal of Rare Earths*, 2006. **24**(1, Supplement 1): p. 90-92.
20. Gao, Z., et al., *A Perspective On Low-Temperature Solid Oxide Fuel Cells*. Vol. 9. 2016.
21. Mahato, N., et al., *Progress in material selection for solid oxide fuel cell technology: A review*. *Progress in Materials Science*, 2015. **72**: p. 141-337.
22. Abdelkader, H. and G. Lacques, *Solid oxide fuel cells*, in *The CRC handbook of solid state electrochemistry edited by P.J. Gellings, H.J.M. Bouwmeester, P.J. Gellings and H.J.M. Bouwmeester, Editors*. 1997, Boca Raton, Fla CRC Press.
23. Ivers-Tiffée, E., A. Weber, and H. Schichlein, *O₂-reduction at high temperatures: SOFC*, in *Handbook of Fuel Cells-Fundamentals Technology and Applications*. 2010, Copyright © John Wiley & Sons, Ltd.

24. Fergus, J.W., *Materials challenges for solid-oxide fuel cells*. JOM, 2007. **59**(12): p. 56-62.
25. Takeda, Y., *Cathodic Polarization Phenomena of Perovskite Oxide Electrodes with Stabilized Zirconia*. Vol. 134. 1987.
26. Rembelski, D., et al., *Characterization and comparison of different cathode materials for SC-SOFC: LSM, BSCF, SSC, and LSCF*. Vol. 12. 2012.
27. Grosz, F., *Proceedings of the Second International Symposium on Solid Oxide Fuel Cells: Held from 2 to 5 July 1991 in Athens, Greece*. 1991: Office for Official Publications of the European Communities.
28. G Bessler, W., et al., *Weber A and Ivers-Tiffe E Model anodes and anode models for understanding the mechanism of hydrogen oxidation in solid oxide fuel cells*. Vol. 12. 2010. 13888-903.
29. Shri Prakash, B., S. Senthil Kumar, and S.T. Aruna, *Properties and development of Ni/YSZ as an anode material in solid oxide fuel cell: A review*. Renewable and Sustainable Energy Reviews, 2014. **36**: p. 149-179.
30. Bieberle, A., *The electrochemistry of solid oxide fuel cell anodes. experiments, modeling, and simulations*. 2000, ETH Zürich.
31. Gong, M., et al., *Sulfur-tolerant anode materials for solid oxide fuel cell application*. Journal of Power Sources, 2007. **168**(2): p. 289-298.
32. Cheng, Z. and M. Liu, *Characterization of sulfur poisoning of Ni-YSZ anodes for solid oxide fuel cells using in situ Raman microspectroscopy*. Solid State Ionics, 2007. **178**(13): p. 925-935.
33. Ishihara, T., et al., *Ni-Fe Bimetallic Anode for Intermediate Temperature Solid Oxide Fuel Cells Using LaGaO₃ Based Oxide Electrolyte*. Materials Science Forum, 2007. **539-543**: p. 1350-1355.
34. Fu, C.J., et al., *A promising Ni-Fe bimetallic anode for intermediate-temperature SOFC based on Gd-doped ceria electrolyte*. International Journal of Hydrogen Energy, 2011. **36**(21): p. 13727-13734.
35. Xu, N., M. Chen, and M. Han, *Oxidation behavior of a Ni-Fe support in SOFC anode atmosphere*. Journal of Alloys and Compounds, 2018. **765**: p. 757-763.

36. Kan, W.H., A.J. Samson, and V. Thangadurai, *Trends in electrode development for next generation solid oxide fuel cells*. Journal of Materials Chemistry A, 2016. **4**(46): p. 17913-17932.
37. Jacobson, A.J., *Materials for Solid Oxide Fuel Cells*. Chemistry of Materials, 2010. **22**(3): p. 660-674.
38. Huang, Y.-H., et al., *Double Perovskites as Anode Materials for Solid-Oxide Fuel Cells*. Science, 2006. **312**(5771): p. 254.
39. Li, W., et al., *Can we predict the formability of perovskite oxynitrides from tolerance and octahedral factors?* Journal of Materials Chemistry A, 2013. **1**(39): p. 12239-12245.
40. Hossain, A., P. Bandyopadhyay, and S. Roy, *An overview of double perovskites $A_2B'B''O_6$ with small ions at A site: Synthesis, structure and magnetic properties*. Journal of Alloys and Compounds, 2018. **740**: p. 414-427.
41. Vasala, S. and M. Karppinen, *A $2 B'B''O_6$ perovskites: A review*. Progress in Solid State Chemistry, 2015. **43**(1-2): p. 1-36.
42. Yin, W.-J., et al., *Oxide perovskites, double perovskites and derivatives for electrocatalysis, photocatalysis, and photovoltaics*. Energy & Environmental Science, 2019. **12**(2): p. 442-462.
43. Ramadass, N., *ABO₃-type oxides—Their structure and properties—A bird's eye view*. Materials Science and Engineering, 1978. **36**(2): p. 231-239.
44. Bartel, C.J., et al., *New tolerance factor to predict the stability of perovskite oxides and halides*. Science Advances, 2019. **5**(2): p. eaav0693.
45. Corrêa, H.P.S., et al., *Synthesis and structural characterization of the Ca_2MnReO_6 double perovskite*. Cerâmica, 2010. **56**: p. 193-200.
46. Richter, J., et al., *Materials design for perovskite SOFC cathodes*. Vol. 140. 2009. 985-999.
47. Meng, Y.S. and M.E. Arroyo-de Dompablo, *First principles computational materials design for energy storage materials in lithium ion batteries*. Energy & Environmental Science, 2009. **2**(6): p. 589-609.
48. Ishikawa, T., et al., *Optical spectroscopy of charge-ordering transition in $La_{1/3}Sr_{2/3}FeO_3$* . Vol. 581. 1998.

49. Riess, I., *Electrochemistry of mixed ionic-electronic conductors*, in *Handbook of Solid State Electrochemistry*, P.J. Gellings, Editor. 2019, CRC Press.
50. O'Hayre, R., *Fuel cell fundamentals*. 2005, Hoboken, NJ: John Wiley & Sons. 409 s.
51. Kirubakaran, A., S. Jain, and R.K. Nema, *A review on fuel cell technologies and power electronic interface*. *Renewable and Sustainable Energy Reviews*, 2009. **13**(9): p. 2430-2440.
52. O'Hayre, R.P., *Fuel cells for electrochemical energy conversion*. *EPJ Web Conf.*, 2017. **148**: p. 00013.
53. Cooper, K.R. and M. Smith, *Electrical test methods for on-line fuel cell ohmic resistance measurement*. *Journal of Power Sources*, 2006. **160**(2): p. 1088-1095.
54. Ivers-Tiffée, E., A. Weber, and H. Schichlein, *Electrochemical impedance spectroscopy*, in *The Handbook of Fuel Cells - Fundamentals, Technology and Applications*. 2010, John Wiley & Sons, Ltd.
55. Barsoukov, E. and J.R. Macdonald, *Impedance Spectroscopy.: Theory, Experiment, and Applications*. 2005: Wiley.
56. Wang, J., et al., *Superior electrochemical performance and oxygen reduction kinetics of layered perovskite $\text{PrBa}_x\text{Co}_2\text{O}_{5+\delta}$ ($x = 0.90-1.0$) oxides as cathode materials for intermediate-temperature solid oxide fuel cells*. *International Journal of Hydrogen Energy*, 2014. **39**(32): p. 18392-18404.
57. Chen, D., R. Ran, and Z. Shao, *Assessment of $\text{PrBaCo}_2\text{O}_{5+\delta}+\text{Sm}_{0.2}\text{Ce}_{0.8}\text{O}_{1.9}$ composites prepared by physical mixing as electrodes of solid oxide fuel cells*. *Journal of Power Sources*, 2010. **195**(21): p. 7187-7195.
58. Meng, F., et al., *Praseodymium-deficiency $\text{Pr}_{0.94}\text{BaCo}_2\text{O}_{6-\delta}$ double perovskite: A promising high performance cathode material for intermediate-temperature solid oxide fuel cells*. *Journal of Power Sources*, 2015. **293**: p. 741-750.
59. Kim, J.H. and J.T.S. Irvine, *Characterization of layered perovskite oxides $\text{NdBa}_{1-x}\text{Sr}_x\text{Co}_2\text{O}_{5+\delta}$ ($x = 0$ and 0.5) as cathode materials for IT-SOFC*. *International Journal of Hydrogen Energy*, 2012. **37**(7): p. 5920-5929.

60. Yu, X., et al., *Cobalt-free perovskite cathode materials $SrFe_{1-x}Ti_xO_{3-\delta}$ and performance optimization for intermediate-temperature solid oxide fuel cells*. *Electrochimica Acta*, 2014. **123**: p. 426-434.
61. Jung, W. and H.L. Tuller, *Impedance study of $SrTi_{1-x}Fe_xO_{3-\delta}$ ($x=0.05$ to 0.80) mixed ionic-electronic conducting model cathode*. *Solid State Ionics*, 2009. **180**(11): p. 843-847.
62. Li, W., et al., *Evaluation of double perovskite $Sr_2FeTiO_{6-\delta}$ as potential cathode or anode materials for intermediate-temperature solid oxide fuel cells*. *Ceramics International*, 2015. **41**(9, Part B): p. 12393-12400.
63. Zhou, Q., et al., *Investigation of cobalt-free perovskite $Sr_2FeTi_{0.75}Mo_{0.25}O_{6-\delta}$ as new cathode for solid oxide fuel cells*. *Materials Research Bulletin*, 2016. **74**: p. 129-133.
64. Niu, B., et al., *Performance of double perovskite symmetrical electrode materials $Sr_2TiFe_{1-x}MoxO_{6-\delta}$ ($x = 0.1, 0.2$) for solid oxide fuel cells*. *Electrochimica Acta*, 2018. **263**: p. 217-227.
65. Lee, G.-Y., et al., *Properties of Cu, Ni, and V doped- $LaCrO_3$ interconnect materials prepared by pechini, ultrasonic spray pyrolysis and glycine nitrate processes for SOFC*. *Journal of Electroceramics*, 2006. **17**(2): p. 723-727.
66. Zhou, W., et al., *Structural, electrical and electrochemical characterizations of $SrNb_{0.1}Co_{0.9}O_{3-\delta}$ as a cathode of solid oxide fuel cells operating below 600°C* . *International Journal of Hydrogen Energy*, 2010. **35**(3): p. 1356-1366.
67. Ding, L., et al., *Promotion on electrochemical performance of a cation deficient $SrCo_{0.7}Nb_{0.1}Fe_{0.2}O_{3-\delta}$ perovskite cathode for intermediate-temperature solid oxide fuel cells*. *Journal of Power Sources*, 2017. **354**: p. 26-33.
68. Yao, C., et al., *A niobium and tungsten co-doped $SrFeO_{3-\delta}$ perovskite as cathode for intermediate temperature solid oxide fuel cells*. *Ceramics International*, 2019. **45**(6): p. 7351-7358.
69. Akhtar, M.J. and R.T.A. Khan, *Structural studies of $SrFeO_3$ and $SrFe_{0.5}Nb_{0.5}O_3$ by employing XRD and XANES spectroscopic techniques*. *Materials Characterization*, 2011. **62**(10): p. 1016-1020.

70. S. Batista, G., et al., *Communication—Detection of Giant Dielectric Constant in Strontium Orthovanadate $Sr_3V_2O_8$* . Vol. 6. 2017. N213-N215.
71. Tamal, T., et al., *Synthesis and Thermoelectric Properties of the B-Site Substituted $SrTiO_3$ with Vanadium*. Vol. 27. 2017.
72. Blennow, P., et al., *Defect and electrical transport properties of Nb-doped $SrTiO_3$* . *Solid State Ionics*, 2008. **179**(35): p. 2047-2058.
73. Karczewski, J., et al., *Electrical and structural properties of Nb-doped $SrTiO_3$ ceramics*. *Journal of Electroceramics*, 2010. **24**(4): p. 326-330.
74. Zhang, K., et al., *Double-site yttria-doped $Sr_{1-x}Y_xCo_{1-y}YyO_{3-\delta}$ perovskite oxides as oxygen semi-permeable membranes*. *Journal of Alloys and Compounds*, 2009. **474**(1): p. 477-483.
75. Zeng, P., et al., *Efficient stabilization of cubic perovskite $SrCoO_{3-\delta}$ by B-site low concentration scandium doping combined with sol-gel synthesis*. *Journal of Alloys and Compounds*, 2008. **455**(1): p. 465-470.
76. Pan, X., et al., *Effect of Co doping on the electrochemical properties of $Sr_2Fe_{1.5}Mo_{0.5}O_6$ electrode for solid oxide fuel cell*. *International Journal of Hydrogen Energy*, 2013. **38**(10): p. 4108-4115.
77. Savaniu, C.D. and J.T.S. Irvine, *La-doped $SrTiO_3$ as anode material for IT-SOFC*. *Solid State Ionics*, 2011. **192**(1): p. 491-493.
78. Niu, Y., et al., *A comparative study of oxygen reduction reaction on Bi- and La-Doped $SrFeO_{3-\delta}$ perovskite cathodes*. Vol. 158. 2011. B132-B138.
79. Xie, Z., et al., *Effects of Co Doping on the Electrochemical Performance of Double Perovskite Oxide $Sr_2MgMoO_{6-\delta}$ as an Anode Material for Solid Oxide Fuel Cells*. *The Journal of Physical Chemistry C*, 2012. **116**(17): p. 9734-9743.
80. Zhang, Q., T. Wei, and Y.-H. Huang, *Electrochemical performance of double-perovskite Ba_2MMoO_6 ($M=Fe, Co, Mn, Ni$) anode materials for solid oxide fuel cells*. *Journal of Power Sources*, 2012. **198**: p. 59-65.
81. Mushtaq, M., et al., *Perovskite $SrFe_{1-x}Ti_xO_{3-\delta}$ ($x \leq 0.1$) cathode for Low Temperature Solid Oxide Fuel Cell*. 2018.

82. Phatungthane, T. and G. Rujijanagul, *Dielectric Properties of Modified SrFe_{0.5}Nb_{0.5}O₃ Ceramics Prepared by a Solid-State Reaction Technique*. Ferroelectrics, 2013. **454**(1): p. 23-28.
83. Zhang, L. and T. He, *Performance of double-perovskite Sr_{2-x}Sm_xMgMoO_{6-δ} as solid-oxide fuel-cell anodes*. Journal of Power Sources, 2011. **196**(20): p. 8352-8359.
84. Xiao, G., et al., *Synthesis and characterization of Mo-doped SrFeO_{3-δ} as cathode materials for solid oxide fuel cells*. Journal of Power Sources, 2012. **202**: p. 63-69.
85. Cowin, P.I., et al., *Conductivity and redox stability of new perovskite oxides SrFe_{0.7}TM_{0.2}Ti_{0.1}O_{3-δ} (TM=Mn, Fe, Co, Ni, Cu)*. Solid State Ionics, 2017. **301**: p. 99-105.
86. dos Santos-Gómez, L., et al., *Symmetric electrodes for solid oxide fuel cells based on Zr-doped SrFeO_{3-δ}*. Journal of Power Sources, 2015. **279**: p. 419-427.
87. Dai, N., et al., *Synthesis and characterization of B-site Ni-doped perovskites Sr₂Fe_{1.5-x}Ni_xMo_{0.5}O_{6-δ} (x = 0, 0.05, 0.1, 0.2, 0.4) as cathodes for SOFCs*. Journal of Materials Chemistry A, 2013. **1**(45): p. 14147-14153.
88. Xie, Z., et al., *Electrical, Chemical, and Electrochemical Properties of Double Perovskite Oxides Sr₂Mg_{1-x}Ni_xMoO_{6-δ} as Anode Materials for Solid Oxide Fuel Cells*. The Journal of Physical Chemistry C, 2014. **118**(33): p. 18853-18860.
89. Aguadero, A., et al., *SrCo_{1-x}Sb_xO_{3-δ} perovskite oxides as cathode materials in solid oxide fuel cells*. Journal of Power Sources, 2009. **192**(1): p. 132-137.
90. Yang, W.-D., *X-ray photoelectron spectroscopy and electrical properties studies of La₂O₃-doped strontium titanate ceramics prepared by sol-precipitation method*. Journal of Materials Science, 1999. **34**(14): p. 3533-3544.
91. Zhang, H., et al., *Fabrication and Photocatalytic Property of One-Dimensional SrTiO₃/TiO_{2-x}N_x Nanostructures*. Vol. 2013. 2013.
92. Bharti, B., et al., *Formation of oxygen vacancies and Ti³⁺ state in TiO₂ thin film and enhanced optical properties by air plasma treatment*. Scientific Reports, 2016. **6**: p. 32355.

93. González-Elipe, A.R., et al., *Compositional changes induced by 3.5 keV Ar⁺ ion bombardment in Ni-Ti oxide systems: A comparative study*. Surface Science, 1989. **220**(2): p. 368-380.
94. Biesinger, M.C., et al., *Resolving surface chemical states in XPS analysis of first row transition metals, oxides and hydroxides: Sc, Ti, V, Cu and Zn*. Applied Surface Science, 2010. **257**(3): p. 887-898.
95. Atuchin, V.V., et al., *Ti 2p and O 1s core levels and chemical bonding in titanium-bearing oxides*. Journal of Electron Spectroscopy and Related Phenomena, 2006. **152**(1): p. 18-24.
96. Mei, B., et al., *The synthesis of Nb-doped TiO₂ nanoparticles by spray drying: an efficient and scalable method*. Journal of Materials Chemistry, 2011. **21**(32): p. 11781-11790.
97. Shibagaki, S. and K. Fukushima, *XPS analysis on Nb-SrTiO₃ thin films deposited with pulsed laser ablation technique*. Journal of the European Ceramic Society, 1999. **19**(6): p. 1423-1426.
98. Nili, H., et al., *Alkali ratio control for lead-free piezoelectric thin films utilizing elemental diffusivities in RF plasma*. CrystEngComm, 2013. **15**(36): p. 7222-7229.
99. Mattsson, A., et al., *Adsorption and Solar Light Decomposition of Acetone on Anatase TiO₂ and Niobium Doped TiO₂ Thin Films*. The Journal of Physical Chemistry B, 2006. **110**(3): p. 1210-1220.
100. Zhu, J., et al., *CO₂-tolerant oxygen-permeable perovskite-type membranes with high permeability*. Journal of Materials Chemistry A, 2015. **3**(45): p. 22564-22573.
101. Dong, X., W. Jin, and N. Xu, *Reduction-Tolerant Oxygen-Permeable Perovskite-Type Oxide Sr_{0.7}Ba_{0.3}Fe_{0.9}Mo_{0.1}O_{3-δ}*. Chemistry of Materials, 2010. **22**(12): p. 3610-3618.
102. Khan, H. and I.K. Swati, *Fe³⁺-doped Anatase TiO₂ with d-d Transition, Oxygen Vacancies and Ti³⁺ Centers: Synthesis, Characterization, UV-vis Photocatalytic and Mechanistic Studies*. Industrial & Engineering Chemistry Research, 2016. **55**(23): p. 6619-6633.

103. Wu, Q.-H., M. Liu, and W. Jaegermann, *X-ray photoelectron spectroscopy of La_{0.5}Sr_{0.5}MnO₃*. *Materials Letters*, 2005. **59**(16): p. 1980-1983.
104. Batis, N.H., P. Delichere, and H. Batis, *Physicochemical and catalytic properties in methane combustion of La_{1-x}CaxMnO_{3±y} (0≤x≤1; -0.04≤y≤0.24) perovskite-type oxide*. *Applied Catalysis A: General*, 2005. **282**(1): p. 173-180.
105. Yamashita, T. and P. Hayes, *Analysis of XPS spectra of Fe²⁺ and Fe³⁺ ions in oxide materials*. *Applied Surface Science*, 2008. **254**(8): p. 2441-2449.
106. Ghaffari, M., et al., *Preparation, surface state and band structure studies of SrTi_(1-x)Fe_(x)O_(3-δ) (x=0-1) perovskite-type nano structure by X-ray and ultraviolet photoelectron spectroscopy*. *Surface Science*, 2012. **606**(5): p. 670-677.
107. Atamanik, E., S.S. Bhella, and V. Thangadurai, *Electrical Properties of Fe-doped Perovskite-like BaNb_{0.75-x}Fe_xNa_{0.25}O_{3-δ} (0.05<x<0.5)*. *Solid State Ionics*, 2011. **192**(1): p. 205-209.
108. Ochoa, N., et al., *Modified Cassava Starches as Potential Corrosion Inhibitors for Sustainable Development*. Vol. 16. 2013. 1209-1219.
109. Zhang, C., J. Sunarso, and S. Liu, *Designing CO₂-resistant oxygen-selective mixed ionic–electronic conducting membranes: guidelines, recent advances, and forward directions*. *Chemical Society Reviews*, 2017. **46**(10): p. 2941-3005.
110. Zhang, X., et al., *Effect of aspect ratio and surface defects on the photocatalytic activity of ZnO nanorods*. *Scientific Reports*, 2014. **4**: p. 4596.
111. Han, X.-G., et al., *Controlling Morphologies and Tuning the Related Properties of Nano/Microstructured ZnO Crystallites*. *The Journal of Physical Chemistry C*, 2009. **113**(2): p. 584-589.
112. Lee, T.-H., et al., *Robust NdBa_{0.5}Sr_{0.5}Co_{1.5}Fe_{0.5}O_{5+δ} cathode material and its degradation prevention operating logic for intermediate temperature-solid oxide fuel cells*. *Journal of Power Sources*, 2016. **331**: p. 495-506.
113. Hua, B., et al., *The Excellence of Both Worlds: Developing Effective Double Perovskite Oxide Catalyst of Oxygen Reduction Reaction for Room and Elevated Temperature Applications*. Vol. 26. 2016.

114. Liu, H., et al., *Effect of oxygen stoichiometry on the insulator-metal phase transition in vanadium oxide thin films studied using optical pump-terahertz probe spectroscopy*. Vol. 103. 2013. 151908.
115. Li, J., J. Xu, and J. Huang, *Nanofibrous vanadium-doped rutile titania derived from cellulose substance by flame synthesis*. *CrystEngComm*, 2014. **16**(3): p. 375-384.
116. Tietz, F., *Thermal expansion of SOFC materials*. *Ionics*, 1999. **5**(1): p. 129-139.
117. Mori, M. and N.M. Sammes, *Sintering and thermal expansion characterization of Al-doped and Co-doped lanthanum strontium chromites synthesized by the Pechini method*. *Solid State Ionics*, 2002. **146**(3): p. 301-312.
118. Ullmann, H., et al., *Correlation between thermal expansion and oxide ion transport in mixed conducting perovskite-type oxides for SOFC cathodes*. *Solid State Ionics*, 2000. **138**(1): p. 79-90.
119. Fagg, D.P., et al., *The stability and mixed conductivity in La and Fe doped SrTiO₃ in the search for potential SOFC anode materials*. *Journal of the European Ceramic Society*, 2001. **21**(10): p. 1831-1835.
120. W. Stevenson, J., et al., *Influence of Cobalt and Iron Additions on the Electrical and Thermal Properties of (La,Sr)(Ga,Mg)O_{3-δ}*. Vol. 147. 2000. 3213.
121. Cascos, V., L. Troncoso, and J.A. Alonso, *New families of Mn⁺-doped SrCo_{1-x}MxO_{3-δ} perovskites performing as cathodes in solid-oxide fuel cells*. *International Journal of Hydrogen Energy*, 2015. **40**(34): p. 11333-11341.
122. Wang, Z., Y. Tian, and Y. Li, *Direct CH₄ fuel cell using Sr₂FeMoO₆ as an anode material*. *Journal of Power Sources*, 2011. **196**(15): p. 6104-6109.



จุฬาลงกรณ์มหาวิทยาลัย
CHULALONGKORN UNIVERSITY

VITA

NAME Ausa Potong
DATE OF BIRTH 28 March 1993
PLACE OF BIRTH Ratchaburi, Thailand
INSTITUTIONS ATTENDED Chulalongkorn University

